A HOLISTIC APPROACH TO THE MODELING OF A BIOPHARMACEUTICAL DOWNSTREAM PROCESS

MECHANISTIC MODELING

zur Erlangung des akademischen Grades eines

DOKTORS DER INGENIEURWISSENSCHAFTEN (DR.-ING.)

von der KIT-Fakultät für Chemieingenieurwesen und Verfahrenstechnik des

Karlsruher Instituts für Technologie (KIT)

genehmigte

DISSERTATION

von

M.Sc. Daniel Federico Rischawy

aus Berlin

Tag der mündlichen Prüfung: 24.11.2023

Erstgutachter: Prof. Dr. Jürgen Hubbuch

Zweitgutachter: Prof. Dr. Matthias Franzreb

Danksagung

Hiermit möchte ich meine aufrichtige Dankbarkeit gegenüber meinen Kollegen und Freunden zum Ausdruck bringen, die mich auf meiner beruflichen Reise begleitet und unterstützt haben. Ein besonderes Wort des Dankes gebührt Prof. Jürgen Hubbuch für seine hervorragende Betreuung und die regelmäßigen wissenschaftlichen Gespräche. Des Weiteren bin ich dankbar für die wissenschaftliche Freiheit, die mir stets gewährt wurde. Ebenso möchte ich Prof. Matthias Franzreb meinen Dank für die Übernahme des Korreferats aussprechen.

Mein Dank erstreckt sich auch auf meine Kollegen bei Boehringer Ingelheim. Insbesondere möchte ich Joey Studts für die Möglichkeit danken, an meiner Doktorarbeit bei Boehringer Ingelheim arbeiten zu dürfen. Zudem schätze ich sehr die uneingeschränkte Unterstützung, die unvergesslichen Konferenzen und die wunderbaren Feste. Weiterhin bin ich Simon Kluters und Till Briskot für ihre Unterstützung während meiner Doktorarbeit zutiefst dankbar. Es war stets eine Freude, sowohl fachliche Diskussionen mit euch zu führen als auch euer offenes Ohr zu schätzen. Besonderen Dank möchte ich auch David Saleh und Gang Wang aussprechen, ohne deren Unterstützung diese Doktorarbeit in dieser Form nicht möglich gewesen wäre. Von der ersten Idee bis zur endgültigen Fertigstellung konnte ich stets auf eure Hilfe zählen. Ihr habt mir geholfen auch schwierige Zeiten und Situation zu bestehen.

Ich bin darüber hinaus dankbar, dass die Arbeitsatmosphäre im DSP Modeling Team stets produktiv als auch inspirierend war. Ebenso möchte ich den talentierten und fleißigen Studenten danken, die mich tatkräftig unterstützt haben: Nathalie Hopf, Adrian Schimek, Frederik Nitsch und Angela Wiebe. Es war mir eine Freude, mit euch zusammenzuarbeiten. Ich wünsche Frederik Nitsch und Adrian Schimek alles Gute und viel Erfolg bei ihrer Doktorarbeit.

Mein Dank gilt auch allen Kollegen in der Downstream-Entwicklung, G71, 3. OG, die mich stets mit Materialien, Methoden und technischem Support im Labor unterstützt haben. Vielen Dank für die wunderbaren Feste und Laborexkursionen. Auch bin ich Judith Thoma und dem neuen Labor sehr dankbar für die herzliche Aufnahme und freue mich auf die kommende gemeinsame Zeit. Darüber hinaus danke ich der gesamten MAB-Arbeitsgruppe für die schöne Zeit bei gelegentlichen Besuchen in Karlsruhe und auf Konferenzen.

Meinen Eltern Gudrun und Daniel danke ich für ihre bedingungslose Unterstützung in allen Lebenslagen. Des Weiteren möchte ich meiner Frau Ulrike für ihre Liebe, ihr Verständnis und den Rückhalt danken, den sie mir während der Erstellung dieser Arbeit geboten hat.

Abschließend möchte ich mich von ganzem Herzen bei allen bedanken, die mich auf meinem Weg begleitet und unterstützt haben.

Zusammenfassung

Die vorgelegte Doktorarbeit beschäftigt sich erstmals damit einen gesamten biopharmazeutischen Downstream Prozess mit computergestützten Modellen zu beschreiben. Mit dem Downstream Prozess ist in diesem Fall die Aufreinigung von therapeutischen Proteinen, zur Erzielung eines definierten Reinheitsgrades für die klinische Applikation gemeint. Der Fertigungsprozess im Downstream besteht in der Regel aus einer Verkettung von mehreren Chromatographie- und Filtrationsschritten. Die wesentliche Aufgabe besteht darin Verunreinigungen und auftretende Prozessschwankungen zuverlässig abzufangen und die Produktqualität zu gewährleisten. Zur Sicherstellung der Produktqualität verlangen Aufsichtsbehörden wie die U.S. Food and Drug Administration (FDA) und die Europäische Arzneimittelagentur (EMA) einen kontrollierten und robusten Fertigungsprozess. Hierdurch soll die Patientensicherheit und die effiziente Marktversorgung des Arzneimittels gewährleistet werden. Die biopharmazeutischen Unternehmen müssen somit alle Prozessparameter und deren Auswirkung auf Produktqualitätsmerkmale ermitteln, überwachen und kontrollieren. Zu den geforderten Qualitätszielen, findet sich die biopharmazeutische Industrie in einer zunehmend kompetitiven Umgebung. Der Kosten- und Zeitdruck nimmt stetig zu und es ist absolut entscheidend die Marktreife des Arzneimittels als erstes Unternehmen zu erreichen. Es ist somit von großem Interesse die aktuelle Prozessentwicklung zu hinterfragen und zu beschleunigen.

Die derzeitige Prozessentwicklung setzt zur Erschließung der Zusammenhänge zwischen Prozessparametern und deren Einfluss auf die Produktqualität hauptsächlich auf experimentelle Ansätze. Häufig wird die statistische Versuchsplanungen, auch Design of Experiments (DoE‘s) genannt, eingesetzt. Hierbei werden die Ursache-Wirkungs-Beziehungen zwischen Prozessparametern und Produktqualität durch Planung, Durchführung und Auswertung speziell designter Experimente erschlossen. Dieser Ansatz war in der Vergangenheit erfolgsversprechend, jedoch gibt es einige Nachteile. Die erhaltenden Zusammenhänge sind prozessgebunden und somit nicht generell gültig oder übertragbar. Zudem sind Vorhersagen außerhalb des experimentell getesteten Rahmens generell nicht zulässig. Aufgrund des exponentiellen Zusammenhanges zwischen der Anzahl an Parametern und Experimenten, ist die Anzahl an testbaren Prozessparametern ebenfalls limitierend. Auch wenn die Anzahl an Parametern geringgehalten wird, ist die experimentelle Durchführung sehr zeitintensiv. Prozessschritt übergreifende Studien würden deshalb einen unrealistischen experimentellen Aufwand bedeuten, da die Anzahl an Prozessparameter jeden möglichen Versuchsrahmen sprengen würde. Somit werden die Prozesseinheiten i.d.R. einzeln betrachtet und

entwickelt. Die genannten Limitationen können potenziell von mechanistischen Modellen ausgeglichen werden. Diese Modelle haben zum Ziel die zugrundeliegenden Prozesszusammenhänge anhand von Naturgesetzen zu beschreiben. Es werden hierbei mathematische Gleichungen herangezogen, welche die zugrundeliegenden Prozesszusammenhänge mit physikalisch-chemischen Modellen verbinden. Vorhersagen durch mechanistische Modelle außerhalb des experimentellen Rahmens sind somit möglich und auch die Unabhängigkeit von Prozessdimensionen ist gegeben. Wenn also Prozesszusammenhänge im Downstream Prozess durch mechanistische Modelle bekannt und beschrieben werden, können hierdurch Experimente und Zeit während der Entwicklung eingespart werden.

Im Idealfall sind alle benötigten Modellparameter bekannt oder direkt messbar. In der Realität müssen jedoch häufig einzelne Modellparameter an wenigen, gezielten Experimenten bestimmt werden, was als Parameteranpassung bezeichnet wird. Die Qualität der Modellvorhersagen hängt somit stark von der Wahl des Modelles und der Experimente zur Parameteranpassung ab. Es ist anzumerken, dass selbst bei Beachtung der genannten Punkte, die Modelle dennoch eine Approximation der Realität bleiben. Dennoch helfen sie uns die Prozesszusammenhänge besser zu verstehen und zu kontrollieren.

Das Ziel der vorliegenden Arbeit war es erstmalig mechanistische Modelle zur Beschreibung einer gesamten Downstream Sequenz zu verknüpfen. Durch die Verknüpfung von mechanistischen Modellen wird eine prozessschritt- und dimensions-übergreifende Prozessbeschreibung ermöglicht. Dies erforderte eine sorgfältige Modellauswahl, sowie die Sicherstellung einer geeigneten Strategie zur Parameteranpassung jedes einzelnen Modells. Das im Labormaßstab entwickelte Modell wurde auf Produktionsdaten getestet, um die industrielle Anwendbarkeit zu demonstrieren. Dies wurde schrittweise in 3 Manuskripten umgesetzt.

In der ersten Veröffentlichung (Kapitel 3) wurde die Verkettung von zwei Ionenaustauschchromatographie Schritten unter Beachtung der Anpassungsschritte veröffentlicht. Dies ermöglicht die Einflussnahme von Puffersubstanzen, pH, Ionen und Proteinkonzentrationen auf die entsprechenden folgenden Prozessschritte zu beschreiben. Als geeignetes Modell für die Einstellschritte hat sich ein Mean-Field Ansatz erwiesen. Für die Beschreibung der Ionenaustauschchromatographie hat sich das Transport-Dispersionsmodell in Kombination mit einem kolloidalen Partikeladsorptionsmodell bewiesen. Das verknüpfte Modell war schließlich in der Lage Prozessvariationen im Produktionsmaßstab von 94 Durchläufen angemessen zu reproduzieren. Das Modell konnte zudem nicht nur die

Prozessperformance reproduzieren, sondern auch die Größenvarianten als kritisches Qualitätsattribut beschreiben. Es konnte erstmals gezeigt werden, dass ein verknüpftes Modell im Labormaßstab entwickelt, durchaus in der Lage ist Schlüsse auf die Produktionsvariabilität zuzulassen.

Das Modell in Kapitel 4 beschreibt die Tangentialflussfiltration (TFF) wie sie für die Ultrafiltration und Diafiltration (UF/DF) in der biopharmazeutischen Industrie angewendet wird. Bei dieser Filtration strömt der Fluss tangential zur Membranfläche und erlaubt somit eine hohe Ankonzentration (Ultrafiltration) bzw. einen Puffertausch (Diafiltration). Während des UF/DF Prozesses wirkt ein komplexes Zusammenspiel aus Drücken und Flüssen in Abhängigkeit der Proteineigenschaften wie der Viskosität. Bisherige Modelle betrachteten lediglich die Ultrafiltration oder den Druck und dies nicht über die gesamten Phasen der UF/DF über die Zeit aufgelöst. Ein modifiziertes Polarisationsmodell in Kombination mit einer modifizierten Darcy Forchheimer Gleichung erwies sich als zuverlässig. Das Modell war in der Lage adäquat auf multivariate Ultrafiltrationsexperimente zu reagieren. Ebenfalls konnte ein kompletter UF/DF Prozess beschrieben werden und Dimensionseffekte beobachtet werden.

In Kapitel 5 wird schließlich das verbundene mechanistische Prozessmodell präsentiert. Hierzu war es notwendig für die restlichen Prozessschritte Modelle zu etablieren. Dies beinhaltet die Beschreibung der Affinitätschromatographie mittels eines Transport-Dispersionsmodells in Kombination mit einer modifizierten Langmuir Adsorptionsisotherme. Das Affinitätsmodell beschreibt die pH induzierte Elution für verschiedene Säulenbeladungen und Prozessfahrweisen, was in der Form bisher noch nicht gezeigt werden konnte. Des Weiteren wurde für die Tiefenfiltration als fähigstes Modell das kombinierte Porenverblockungsmodell identifiziert. Das Modell kombiniert die klassische Porenverblockung mit der Kuchenfiltration, welche erstmals auf die Tiefenfiltration angewendet werden konnte. Es konnte schließlich die Tiefenfiltration über die Zeit aufgelöst und die fluss- als auch druckgesteuerte Filtration beschrieben werden. In der Summe konnte schließlich ein verbundenes mechanistisches Prozessmodell für einen gesamten biopharmazeutischen Downstream Prozess erstellt werden. Das im Labormaßstab entwickelte Prozessmodell wurde ebenfalls erstmals genutzt, um auf industrielle Produktionsläufe zu extrapolieren. Die Extrapolation der Prozessinputs beinhaltete nicht nur Chromatographie Säulen doppelter Trennlänge, sondern auch weitere Prozessbedingungen, wie sie im Labormaßstab nicht zur Modellentwicklung verwendet wurden. Die Modellqualität und Anwendbarkeit konnte zusätzlich gezeigt werden, indem

die Prozessschwankung von 23 Produktionsläufen adäquat über den gesamten Prozess von dem Prozessmodell wiedergeben wurde.

Zusammenfassend konnte in der vorliegenden Arbeit anhand eines Proteins gezeigt werden, dass die zugrunde liegenden Mechanismen in einem biopharmazeutische Downstream Prozess in verbundener Form beschrieben werden können. Die Herausforderung der Modellauswahl und Umsetzung konnten anhand des vorliegenden Prozesses umgesetzt werden. Die Erkenntnisse und Modelle können als Grundlage für weitere Studien und Prozesse dienen und bieten somit ein Fundament in Richtung modellgestützter Prozessentwicklung.

Abstract

The present doctoral thesis is the first to describe an entire biopharmaceutical downstream process with computer-aided models. Downstream processing refers to the purification of therapeutic proteins to achieve a defined degree of purity for clinical application. The downstream manufacturing process usually consists of a concatenation of several chromatography and filtration steps. The essential task is to reliably remove impurities, control process fluctuations that occur, and to ensure product quality. To ensure product quality, regulatory agencies such as the U.S. Food and Drug Administration (FDA) and the European Medicines Agency (EMA) demand a controlled and robust manufacturing process. This is to ensure patient safety and efficient market supply of the drug product. Biopharmaceutical companies must therefore identify, monitor, and control all process parameters and their impact on product quality. To the required quality goals, the biopharmaceutical industry finds itself in an increasingly competitive environment. Cost and time pressures are steadily increasing, and it is critical to be the first to market with a novel drug candidate. It is therefore of great interest to challenge and accelerate the current process development.

Current process development mainly relies on experimental approaches to develop the relationships between process parameters and their influence on product quality. For this, statistical design of experiments (DoE) is often used. Here, the cause-effect relationships between process parameters and product quality are developed by planning, conducting, and evaluating dedicated experiments. This approach has been promising, and yet it comes with some drawbacks. The relationships obtained are process-specific and not generally valid or transferable to future processes. In addition, predictions outside the experimentally tested framework are generally not valid. The number of testable process parameters is also limited due to the exponential relationship between the number of parameters and experiments. Even if the number of parameters is kept low, the experimental execution is very time consuming. Moreover, cross-unit studies would require an unrealistic experimental effort, since the number of process parameters would exceed any possible experimental framework. Thus, the process units are usually considered and developed individually. The limitations mentioned above can be compensated by mechanistic models. The aim of these models is to describe the underlying process relationships on the basis of natural laws. Mathematical equations used here link the underlying process relationships with physical chemical models. Predictions by mechanistic models outside the experimental framework are thus possible and the independence of process dimensions is

given. If downstream process interrelationships are known and described by mechanistic models, this can save experiments and time during development.

Ideally, all required model parameters are known or directly measurable. In reality, however, individual model parameters often have to be mathematically determined using a few dedicated experiments, which is usually referred to as parameter estimation. Therefore, the quality of model predictions strongly depends on the choice of the model and the experiments for parameter fitting. It should be noted that even if the above points are taken into account, the models still remain an approximation of reality. Nevertheless, they help us to better understand and control the process relationships.

The aim of the present work was to link mechanistic models of different unit operations together for the first time to describe an entire downstream sequence. Linking mechanistic models enables a process description that spans process steps and dimensions. This required careful model selection, as well as ensuring an appropriate experimentation and strategy for parameter fitting of each model. The laboratory scale model developed was tested using various production data to demonstrate industrial applicability. This was implemented stepwise in three manuscripts.

In the first publication (Chapter 3), the concatenation of two ion-exchange chromatography steps was published, taking into account the surrounding adjustment steps. This allows the influence of buffer substances, pH, ion, and protein concentrations on the respective subsequent process steps to be described. A mean-field approach has proven to be a suitable model for the adjustment steps. For the description of ion-exchange chromatography, the transport-dispersive column model in combination with a colloidal particle adsorption model proved to be suitable for this study. The linked model was finally able to adequately reproduce process variations at the production scale of 94 runs. The model was also able to reproduce not only process performance, but also size variants of the product as a critical quality attribute. For the first time, it has been shown that a linked model developed at laboratory scale allows conclusions to be drawn about production variability.

The model in chapter 4 describes tangential flow filtration (TFF) as applied to ultrafiltration and diafiltration (UF/DF) in the biopharmaceutical industry. In this filtration step, the flow is tangentially to the membrane surface, allowing to reach high product concentration (ultrafiltration) and buffer exchanges (diafiltration). During the UF/DF process, a complex interplay of pressures and fluxes occurs depending on quantities such as the protein viscosity and protein concentration. Previous models considered only filtration and pressure independently and were not applied over the entire duration of the UF/DF

phases. A modified polarization model combined with a modified Darcy Forchheimer equation proved to be reliable. The model was able to respond adequately to multivariate ultrafiltration experiments. In addition, a complete UF/DF process was described, and scale-up effects could be observed.

Finally, chapter 5 presents the connected mechanistic process model. For this purpose, it was necessary to establish models for the remaining process steps. This includes the description of affinity chromatography using a transport-dispersive column model in combination with a modified Langmuir adsorption isotherm. The affinity model describes the pH induced elution for different column loadings and process driving modes, which has not been shown in the form before. Furthermore, for depth filtration, the most capable model identified was the combined pore blocking model. The model combines classical pore blocking with cake filtration, which could be applied to depth filtration for the first time. It was finally possible to resolve depth filtration over time and describe it for both flow- and pressure-controlled filtration. In conclusion, this work describes the first connected mechanistic process model for an entire biopharmaceutical downstream process. The process model developed at laboratory scale was also used for the first time to extrapolate to industrial production runs. The extrapolation includes not only chromatography columns of twice the separation length in some cases, but also process conditions not included for model development at the laboratory scale. The model quality and applicability could additionally be demonstrated by the fact that the process model adequately represents the process variation of 23 production runs over the entire process.

In summary, the present dissertation used a protein to demonstrate that the underlying mechanisms in a biopharmaceutical downstream process can be described in connected form using mechanistic models. The challenge of model selection and implementation could be resolved using the present process. The findings and models are a basis for further work and will serve as a foundation for model-based process development.

Table of contents

1 Introduction

Biopharmaceuticals or biologics are large molecules that are not produced chemically but in living host cells from plants, animals, or bacteria [1]. Since the first approval of a recombinant form of human insulin in 1982, biologics have transformed disease cures, particularly in the areas of autoimmune diseases and refractory cancers [1–3]. Furthermore, the time for innovative breakthroughs is far from over, as demonstrated by recent mRNA vaccines against SARS-CoV-2, which has saved countless lives [4]. The market value of biopharmaceuticals continues to rise and was estimated to US $343 billion in 2021 [5]. Biopharmaceutical approvals by the US Food and Drug Administration (FDA), or the European Medicines Agency (EMA) are still dominated by therapeutic proteins in particular monoclonal antibodies (mAbs). In the period of January 2018 to June 2022, among the 197 approved biopharmaceuticals, 97 of these approvals in the United States and the EU were for mAbs [5]. Nearly half of the mAbs approved or in regulatory review have oncology indication [6]. The specificity of mAbs allows for targeting specific cell surface antigens or receptors involved in the interaction between the immune system and tumor cells. This makes mAbs one of the most successful and important strategy for the treatment of various tumors [7–10].

Therapeutic proteins such as mAbs have a molecular weight of approximately 150 kDa which is significantly larger compared to small molecules like Aspirin with 0.18 kDa [11,12]. This large and complex protein structure can only be expressed by living host cells. The fermentation with host cells, the molecule size and molecule complexity lead to manufacturing challenges [13]. Besides the target protein, the harvested cell culture fluid (HCCF) potentially contains various impurities such as host cell proteins (HCP), DNA, adventitious and endogenous viruses, lipids, proteases and other enzymes, product related impurities and other additives. To ensure patient safety, impurity levels need to be below an acceptable threshold in the final product [14,15]. This is usually achieved by a sequence of orthogonal chromatography and filtration steps referred to as downstream process.

To accelerate process development a general platform process is desired to bring drug candidates as fast as possible into clinic [16,17]. However, the process behavior of the target protein, and related impurities highly depend on

their protein characteristics which can drastically differ [18]. Furthermore, a trend towards diversification and increasing antibody format complexity does not allow for generalization of process conditions. Some of the new formats include bispecific antibodies, antibody-drug conjugates, and antibody fragments [19–22]. A general process is therefore more of a goal than a reality. Moreover, adapting to discrepancies in process behavior presents a challenge with the current development strategy, which is primarily experimental and heavily dependent on knowledge gained from past projects. This can lead to time consuming sequential trial and error experiments in case of unusual process behavior. In this case, not only are the chances of success uncertain, but there is also a risk of delays in the project schedule. Furthermore, this timely strategy seems to be outdated in an environment of increasing competition and requirements for cost savings and efficiency [23].

The challenges in biopharmaceutical process development require new and more efficient methods. In general, a lack of process understanding requires extensive experimentation to mitigate risk. A better understanding can therefore reduce or even replace experiments and thus time and costs. In addition, regulatory authorities encourage a systematic approach and process understanding based on sound science as stated in the ICH Q8R2 [24,25]. This fundamental process understanding can be derived from first principal models referred to as mechanistic models. Such models allow to simulate the process based on underlying physical phenomena described by mathematical equations [26,27]. The comparison of model predictions with experimental measures allows to augment, test, and proof the current state of process understanding. In fact, the evaluation of a theory's predictions in mathematical form based on real experimental data can be regarded as the foundation of the scientific method [28]. From the perspective of developing industrial processes, models offer significant value by providing essential knowledge and theoretical foundation, which can prove to be critical when time is a constraint, data is unavailable, and prompt decisions are necessary.

In the following sections, the fundamentals of chromatography and filtration are presented. This encompasses the mathematical description of relevant downstream chromatography and filtration process models.

1.1 Downstream process of biopharmaceuticals

1.1.1 Introduction to preparative liquid chromatography

Liquid chromatography serves as the workhorse in purification of therapeutic proteins. The solid stationary phase consists of packed spherical beads referred to as resin beads or adsorber beads. The mobile phase transported through the column contains the product and other components. A retention difference of components can be achieved based on their differing characteristics. A separation by size is achieved with size exclusion chromatography (SEC), where smaller components have access to more volume of the porous resin and thus show reduced migration speed. Larger molecules are simply excluded by their size and therefor elute earlier. If components interact with the resin surface, it is referred to as adsorption. In industrial downstream processes of therapeutic proteins, adsorption chromatography is primarily applied and can be divided in three main mechanisms as schematically illustrated in Figure 1. Hydrophobic interaction chromatography (HIC) adsorbs proteins based on their hydrophobicity. Usually, hydrophobic amino acids are located to the interior of the protein and hydrophilic to the exterior. However, high salt concentrations disturb the water shell of the protein which enforces hydrophobic interaction of exterior hydrophobic patches with the ligand. The hydrophobic binding is sensitive to changes in ionic strength, pH, organic solvents, temperature, and hydrophobicity of the protein. In simplified terms, the hydrophobic adsorption increases with a protein close to its isoelectric point (pI), high ionic strength, high temperature, and absence of organic solvents. When the ligand is positively or negatively charged, adsorption is enabled by ionic interaction, known as ion exchange chromatography (IEX). A negatively charged resin ligand is referred to as cation-exchange chromatography (CEX) and a positively charged ligand as anion-exchange chromatography (AEX). Both forms are of interest in this thesis and therefore discussed in detail in section 1.2.3.2. The term mixed-mode chromatography (MMC) refers to a ligand with at least two orthogonal interactions, for example if a ligand consists of anionic and hydrophobic ligands. Affinity chromatography (AC) binds a product via multipoint adsorption according to a group-specific molecular structure. The affinity chromatography is discussed in more detail in section 1.2.3.1.

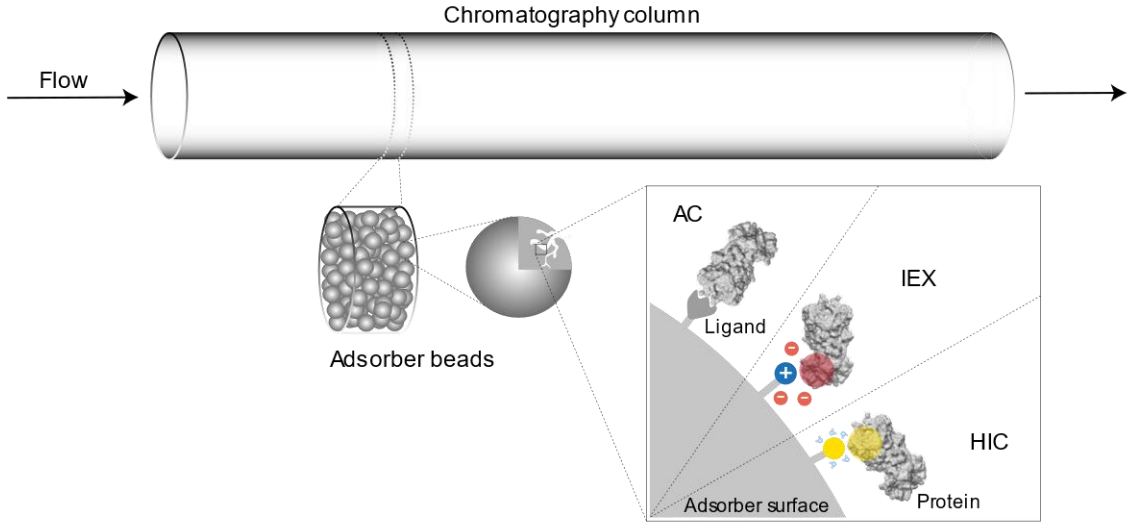

Figure 1: Schematic illustration of preparative adsorption chromatography. The column is packed with adsorber beads. The adsorber surface is coated with functional groups referred to as ligands, which define the interaction mode. The protein can adsorb to the resin surface via affinity, ionic interaction, or hydrophobic interaction: Affinity chromatography (AC), ion-exchange chromatography (IEX), or hydrophobic interaction chromatography (HIC). In this figure, the IEX is exemplary an anion-exchange chromatography (AEX) indicated by the positive charge of the ligand.

The six phases of a preparative chromatography bind-elute process start with an initial equilibration phase. This ensures that the mobile phase and stationary phase are in equilibrium. During the second phase the protein is loaded onto the column. This is followed by at least one wash phase to remove weakly bound impurities. In the fourth elution face, the protein is eluted and collected. Then impurities removed from the resin during the fifth phase, the so-called regeneration phase. During the last phase the column is buffer exchanged in storage conditions. If the loading conditions are non-binding, the mode is referred to as flow through. This mode is advantageous when impurities bind to the column, but not the target protein, under these conditions. Since the flow through is collected the elution phase is skipped, whereas the wash, regeneration, and storage phase are performed similarly to the bind-elute mode [27]. An illustration for a bind-elute and flow-through chromatogram is presented in Figure 2.

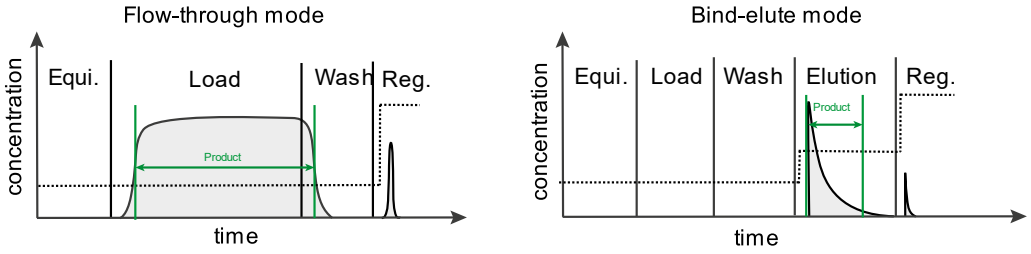

Figure 2: Chromatogram illustration for bind-elute and flow-through chromatography. In flow-through mode the target protein does not interact with the chromatography column, but the impurities bind to the resin. In bind-elute mode, the target protein binds to the resin and is eluted under conditions that aim to elute the product without the impurities. The dashed line indicates intended buffer changes e.g., salt concentration. The final storage phase was not included in this figure.

During process development the overall aim is to identify the optimal combination of orthogonal chromatography steps and process conditions to achieve a maximum of purity and yield. In general, the more similar the impurities are in process behavior to the target protein, the more challenging their depletion becomes. In instances of this nature, the selection of resin variations, even those of the same chromatography classification, can yield significant distinctions in outcome. For example, the depletion capability of a weak cation-exchange utilizing a functional group of carboxyl may diverge from that of a strong cation-exchange employing a sulfopropyl group.

1.1.2 Introduction to membrane systems

Membrane filtration processes play an indispensable role in biopharmaceutical processes. The general mechanism separates components from solution through a membrane, mainly by steric exclusion and adsorption. Depending on the membrane pore size, the membrane either retains the product or contaminants such as host cell proteins, DNA, microorganisms, and viruses. The two types of filtration operations are (i) normal flow filtration, where the filtrate passes the membrane in direction of the flow, and (ii) tangential flow filtration. Commonly used normal flow filtration processes are the microfiltration, depth filtration and virus filtration. Normal filtration processes are controlled either by constant pressure or constant flow. Microfiltration membranes in biopharmaceutical downstream processes are commonly used as sterile filtration of protein solutions and buffers. The membranes usually consist of polyethersulfone (PES) or polyvinylidene fluoride (PVDF) with a pore size of 0.1 – 0.2 µm. This pore size allows smaller molecules such as the target protein to pass and excludes cells and other larger contaminants [29,30]. In contrast, the depth filtration consists of complex pore

structures and multiple pore sizes. The filter retains particles through the entire depth of the filter pore due to size and adsorption. These filters provide a high capacity for clarification purposes. The filter material is usually composed of cellulose or polypropylene fibers combined with diatomaceous earth [31–33]. Virus filters are specifically designed in pore size to exclude viruses and are an integral part of a downstream process. A pore size of usually 20 nm retains viruses while letting the target protein pass the membrane. The membrane material consists of PES, PVDF or cuprammonium regenerated cellulose. To decrease protein binding, the hydrophobic PES and PVDF material can be modified to be more hydrophilic. The overall filtration performance also depends on the pore asymmetry and the number of membrane layers [34]. A schematic illustration of the standard blocking mechanisms during normal flow filtration are presented in Figure 3. The foulant is thought to either clog an entire pore, form a cake layer on the surface, constrict the pore diameter, or show a combination of these. Although the blocking mechanisms are simplified models and filter pores are not perfect cylinders, they are useful to interpret a filtration process as discussed in section 1.3.1.

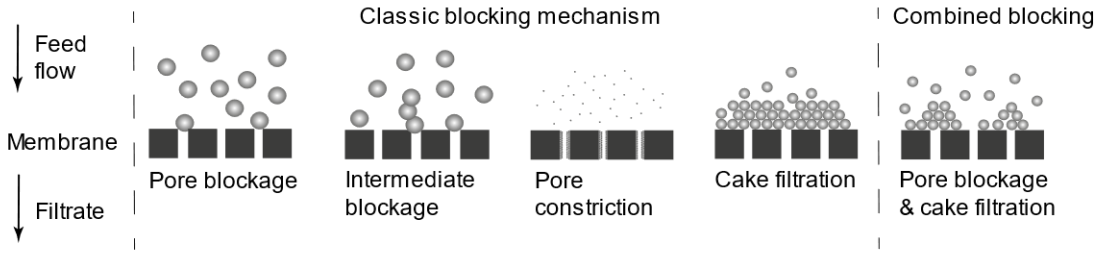

Figure 3: Filtration blocking mechanisms: The reduction in filtrate flow over time can be attributed to various blocking mechanisms. The dominant blocking mechanism is determined by the process parameters and the properties of the foulant and filter. It is even possible to observe a combination of classic blocking mechanisms, such as pore blockage and cake filtration.

Tangential flow filtration also referred to as ultrafiltration or crossflow filtration retains the target protein with a pore size between smaller than 20 nm. Typically, the membrane exclusion is defined by the size of proteins that are excluded, such as those with a molecular weight of 30 kDa. The most common application is for ultrafiltration and diafiltration (UF/DF) processes with flat sheet cassettes. Due to the tangential crossflow, the membrane is prevented from fouling which allows to reach high protein concentrations up to 200 g/L. For processing, the cassette is connected in a circle to a stirred tank as presented in Figure 4. The protein solution is pumped by the feed pump in circles from the stirred tank, tangential through the TFF membrane sheets and

back to the stirred tank. Inflows can be either buffer or feed solution and the outflow is referred to as permeate. The overall aim of a UF/DF process is to achieve a defined buffer composition and target concentration which is achieved in multiple filtration phases. First the load material is concentrated in an ultrafiltration step to reduce the volume. This concentrated pool is then buffer exchanged by continuously adding buffer in the same rate as the filtrate flow, also referred to as permeate flow, and thus maintain a constant volume in the stirred tank. For this a buffer volume of 6-12 times of the stirred tank volume is exchanged which is referred to as diafiltration volumes (DV). Finally, the buffer exchanged pool can be concentrated in a final ultrafiltration step to reach the target concentration [29,30]. The main control parameter for the permeate flow is the transmembrane pressure (TMP) via a retentate valve. A detailed description on the control of UF/DF processes is given in Section 1.3.2.

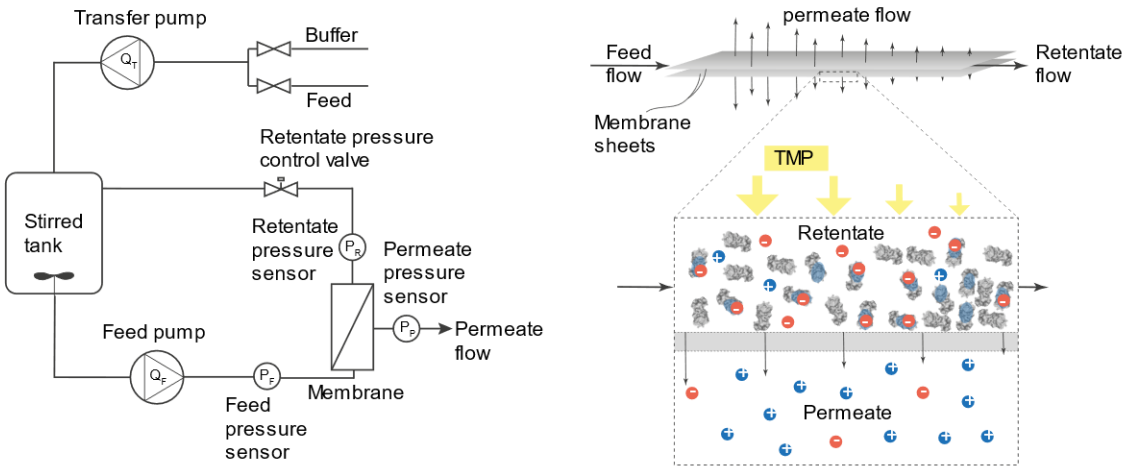

Figure 4: UF/DF filtration process: The left part of the figure shows a schematic illustration of the UF/DF system flow paths. The right side illustrates a zoom into a membrane sheet visualizing general effects of TFF. The membrane is permeable for small solutes such as ions but retentative for the relatively large protein of interest. The TMP drives the permeate flow and the crossflow prevents blockage of the membrane surface. This results in a concentration increase on the membrane length in the crossflow direction. In the meantime, a pressure loss results in a reduction of the local TMP. In addition, the positively charged patches (blue) of the protein attract negatively charged ions (red). The resulting difference in ion composition between the retentate and permeate side of the membrane can influence the solution pH which is referred to as Donnan effect.

The semipermeable membrane and the charged patches of the protein can result in different ion concentrations between the retentate and the permeate. This can result in undesired concentration and pH shifts of the final concentrated pool. The described phenomenon is known as the Donnan effect and is further discussed in Section 1.3.2.

1.1.3 Downstream sequence

As mentioned earlier, most biopharmaceuticals are monoclonal antibodies or related products. Today's production is primarily based on recombinant Chinese hamster ovary (CHO) cell fermentation. The cells have proven to be stable over time and express proteins with glycoforms that are bioactive in humans. Furthermore, continuous vector, cell, and process engineering increased the productivity with titers up to 10 g/L [35]. The filtered or centrifuged cell culture fluid, harvested after about 14 days of fermentation, contains the product but also a number of contaminants.

A possible downstream process sequence for the purification is presented in Figure 5. Most of the HCPs, cell debris, DNA, cell culture additives can be removed with a capture chromatography step (Unit I). This is usually a protein A affinity chromatography step performed in bind-elute mode. The protein binds under neutral pH as described in more detail in Section 1.2.3.1. Subsequently to specific wash steps, the elution is accomplished with a low pH buffer of approximately pH 3.5. The remaining impurity levels can depend on the molecules' surface chemistry, the cell culture, and harvest condition. Since most mAbs are stable under low pH conditions, the already low pH is used to proceed with a low pH hold step (Unit II) to inactivate retro viruses [16]. In general, for pH adjustments, strong acids and bases are avoided due to possible product denaturation. The neutralized pool typically shows high turbidity levels which can be clarified by depth filtration (Unit III). The subsequent chromatography steps are referred to as polishing sequence and typically consist of two orthogonal chromatography steps. The neutral pH after depth filtration can be adjusted (Unit IV) to meet pH conditions suitable for AEX (Unit V). The typically elevated pI of mAbs enables this chromatography step to be performed under flow-through conditions at neutral or above pH, where negatively charged DNA and HCPs bind to the resin.

At this step aggregates, which can be considered a critical quality attribute (CQA) are still in the bulk solution. The second polishing step, exemplary CEX, aims to remove product related impurities. An pH adjustment step (Unit VI) is used to ensure suitable loading conditions for CEX bind-elute around pH 5. The positively charged mAb binds to the CEX column and is eluted either with a salt step or salt gradient elution. Aggregates tend to have higher charges and thus bind stronger to the resin. In rare cases a third chromatography might be necessary to reach the demanded purity. The CEX eluate of high ionic strength might be pH adjusted (Unit VIII) for virus filtration (Unit IX). The virus filtration is an orthogonal step to Unit II and excludes potential retroviruses and parvoviruses. Usually, the final downstream unit is the UF/DF to concentrate the product (ultrafiltration) and buffer exchange the solution

(diafiltration) (Unit X). The concentrated and buffer exchanged UF/DF pool can then be formulated with a formulation buffer.

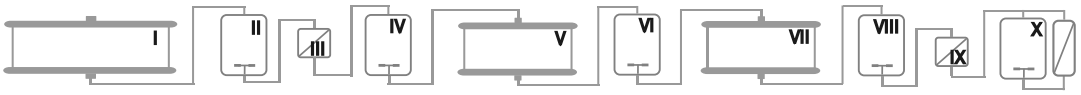

Figure 5: Downstream process at a glance: I - capture, II - pH virus inactivation, III - depth filtration, IV - adjustment 1, V - polishing chromatography, VI - adjustment 2, VII - polishing chromatography, VIII - adjustment 3, IX - virus filtration, X - UF/DF

1.2 Fundamentals of preparative liquid chromatography

1.2.1 Modeling liquid chromatography

1.2.1.1 Column model

The chromatography column is a cylinder of volume V_C [m³], length L_C [m] and radius r_C [m] packed with resin beads of radius r_P [m]. The column is operated under an incompressible fluid flow at isothermal and isobaric condition. In this section the molar material transport equation of fluid flow outside the particles, referred to as interstitial phase, for a chromatography column is derived. Figure 6 illustrates a differential volume element of a chromatography column.

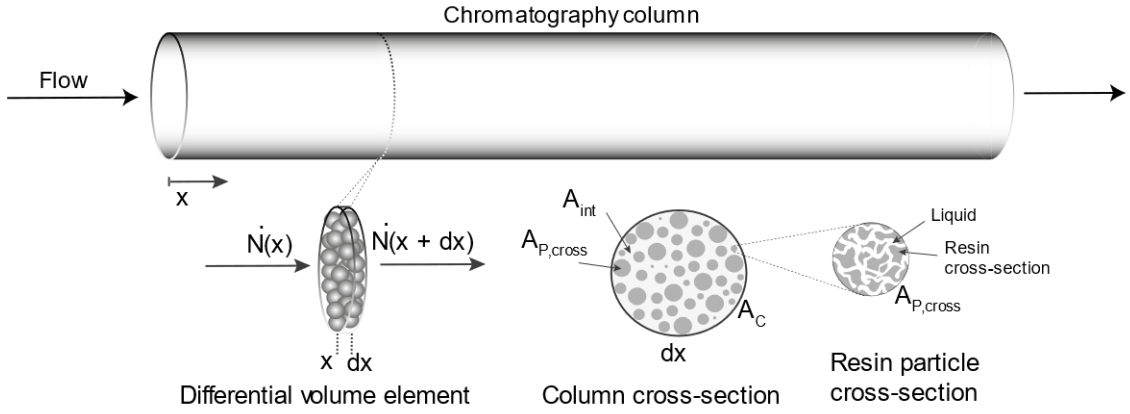

Figure 6: Molar material flux of a differential distance in a cylindrical chromatography column. The solid phase is represented in grey color and the liquid phase in white. The area of the differential column cross-section A_C illustrates the division in the resin cross-section area and the liquid interstitial area A_{int}. The resin particle itself is further divided in the liquid and the solid resin fraction, also referred to as resin backbone or resin skeleton. The protein-resin interaction takes place at the boundary area between liquid and resin backbone.

First the interstitial fluid flow along the column length axis $x \in [0, L_C]$ within a differentially small distance can be described by a material balance for component i:

$$\frac{\partial(dN_i(x,t))}{\partial t} = \dot{N}_i(x) - \dot{N}_i(x+dx) - d\dot{N}_{\text{trans},i}(x) \qquad (1)$$

where $\dot{N}_i(x)$ [mols^{-1}] represents the material inflow, $\dot{N}_i(x+dx)$ the outflow and $d\dot{N}_{\text{trans},i}(x)$ the conversion term. The outflow term can be approximated by a first order Taylor approximation:

$$\dot{N}_i(x + dx) = \dot{N}_i(x) + \frac{d\dot{N}_i(x)}{dx} dx \qquad (2)$$

which inserted for the outflow term in Eq. (1), results in:

$$\frac{\partial(dN_i(x,t))}{\partial t} = -\frac{d\dot{N}_i(x)}{dx} dx - d\dot{N}_{\text{trans},i}(x) \qquad (3)$$

The molar material transport $\dot{N}_i(x)$ within the interstitial liquid phase consists of diffusion and convection:

$$\dot{N}_i(x) = \dot{N}_{\text{diffusion},i}(x) + \dot{N}_{\text{convection},i}(x) \qquad (4)$$

defined by Fick's law for diffusion:

$$\dot{N}_{\text{diffusion},i}(x) = -A_{\text{int}} D_{\text{AX}} \frac{\partial c_i(x,t)}{\partial x} = -A_C \varepsilon_{\text{int}} D_{\text{AX}} \frac{\partial c_i(x,t)}{\partial x} \qquad (5)$$

where D_{AX} [m²s⁻¹] represents the axial dispersion, A_{int} [m²] the interstitial cross-sectional area, and c_i [molm³] the concentration in the interstitial fraction. The convective flow is given by:

$$\dot{N}_{\text{convection},i}(x) = u_{i,\text{int}} A_{\text{int}} c_i(x,t) = \frac{u}{\varepsilon_{\text{int}}} A_C \varepsilon_{\text{int}} c_i(x,t) = u A_{\text{C}} c_i(x,t). \qquad (6)$$

where the interstitial flow $u_{i,\text{int}}$ [ms⁻¹] is the driving term. Both Eq. (5) and Eq. (6) are described in terms of the column cross-sectional area A_{C} [m²] and the flow rate u [ms⁻¹]. This is achieved with the interstitial fraction ε_{int} [-] defined as the interstitial column volume V_{int} [m³] to V_{C} ratio:

$$\varepsilon_{\text{int}} = \frac{V_{\text{int}}}{V_{\text{C}}} = \frac{A_{\text{int}}}{A_C} \qquad (7)$$

In the following, Eq. (3) is considered and simplified. First, inserting Eq. (4)-(6) for the first term in Eq. (3) results in:

$$\begin{aligned} \frac{d\dot{N}_i(x)}{dx} &= \frac{d\left(-A_{\text{C}} \varepsilon_{\text{int}} D_{\text{AX}} \frac{\partial c_i(x,t)}{\partial x} + u A_{\text{C}} c_i(x,t)\right)}{dx} dx \\ &= \left(-D_{\text{AX}} \varepsilon_{\text{int}} \frac{\partial^2 c_i(x,t)}{\partial x^2} + u \frac{\partial c_i(x,t)}{\partial x}\right) A_{\text{C}} dx. \end{aligned} \qquad (8)$$

The conversion term in Eq. (3) accounts for transfer through the film layer which is formed between the interstitial and the particles liquid phase. The transfer through the film layer surrounding the particles surface A_p[m²] is driven by the concentration difference between interstitial and the solute concentration in the particle $c_{\mathrm{p},i}$ [molm³]:

$$\dot{N}_{\mathrm{trans},i}(x) = k_{\mathrm{eff},i}\left(c_i(x,t) - c_{p,i}(x,t)\right)A_\mathrm{p} \qquad (9)$$

where $k_{\mathrm{eff},i}$ [ms^{-1}] represents the effective mass transfer coefficient. A schematic illustration of the film transfer concentration profile is presented in Figure 7. Eq. (9) needs to be described in terms of the column volume. Therefore, the resin particle surface to resin particle volume ratio V_p [m³] is required:

$$\frac{\mathrm{A_p}}{V_\mathrm{p}} = \frac{4\pi {r_\mathrm{p}}^2}{\frac{4}{3}\pi {r_\mathrm{p}}^3} = \frac{3}{r_\mathrm{p}} \qquad (10)$$

where the particle volume in terms of the column volume is defines as:

$$V_\mathrm{p} = (1-\varepsilon_\mathrm{int})V_\mathrm{C} \qquad (11)$$

which leads to the expression:

$$A_\mathrm{p} = \frac{3}{r_\mathrm{p}}(1-\varepsilon_\mathrm{int})V_C \qquad (12)$$

for the particle surface area. Now Eq. (9) and Eq. (12) can be inserted in Eq. (3) for the boundary layer transport description in a differential column volume:

$$\begin{aligned} d\dot{N}_{\mathrm{trans},i}(x) = {} & d\left(k_{\mathrm{eff},i}\frac{3}{r_\mathrm{p}}(1-\varepsilon_\mathrm{int})\left(c_i(x,t) - c_{p,i}(x,t)\right)V_C\right) \\ & = k_{\mathrm{eff},i}\frac{3}{r_\mathrm{p}}(1-\varepsilon_\mathrm{int})\left(c_i(x,t) - c_{p,i}(x,t)\right)A_\mathrm{C}dx. \end{aligned} \qquad (13)$$

The left-hand side of Eq. (3) can be transformed for an incompressible fluid with the product rule to:

$$\frac{\partial(dN_i(x,t))}{\partial t} = \frac{\partial(dV_\mathrm{int}c_i(x,t))}{\partial t} = \varepsilon_\mathrm{int}A_\mathrm{C}dx\frac{\partial c_i(x,t)}{\partial t} \qquad (14)$$

The Eqs. (8), (13) and (14) derived in this section inserted in Eq. (3) result in:

$$\begin{aligned}\varepsilon_{\text{int}} A_{\text{C}} dx \frac{\partial c_i(x,t)}{\partial t} \\ = \left(-u \frac{\partial c_i(x,t)}{\partial x} + D_{\text{AX}} \varepsilon_{\text{int}} \frac{\partial^2 c_i(x,t)}{\partial x^2}\right) A_C dx \\ - k_{\text{eff},i} \frac{3}{r_{\text{p}}} (1-\varepsilon_{\text{int}}) \left(c_i(x,t) - c_{p,i}(x,t)\right) A_{\text{C}} dx\end{aligned} \quad (15)$$

which can be simplified to

$$\begin{aligned}\frac{\partial c_i(x,t)}{\partial t} = -\frac{u}{\varepsilon_{\text{int}}} \frac{\partial c_i(x,t)}{\partial x} + D_{\text{AX}} \frac{\partial^2 c_i(x,t)}{\partial x^2} \\ - \frac{(1-\varepsilon_{\text{int}})}{\varepsilon_{\text{int}}} \left(k_{\text{eff},i} \frac{3}{r_{\text{p}}} \left(c_i(x,t) - c_{p,i}(x,t)\right)\right)\end{aligned} \quad (16)$$

which is a partial differential equation (PDE) referred to as transport dispersive model (TDM). Eq. (16) can be simplified to the equilibrium dispersive model (EDM) when the boundary layer transport term is neglected:

$$\frac{\partial c_i(x,t)}{\partial t} = -\frac{u}{\varepsilon_{\text{int}}} \frac{\partial c_i(x,t)}{\partial x} + D_{\text{AX}} \frac{\partial^2 c_i(x,t)}{\partial x^2} - \frac{(1-\varepsilon_{\text{int}})}{\varepsilon_{\text{int}}} \frac{dq_i(x,t)}{dt}. \quad (17)$$

To solve the EDM or TDM boundary conditions are required. The Danckwerts boundary conditions at the inlet and outlet can be considered the industry standard [36]. The concentration at the column inlet is defined by the first boundary condition:

$$\frac{\partial c_i(x=0,t)}{\partial t} = \frac{\text{u}_{\text{int}}}{D_{\text{AX}}} \left(\text{c}_i(0,t) - c_{\text{in},i}(t)\right). \quad (18)$$

where $c_{\text{in},i}$ represents the inlet concentration and at the outlet a zero gradient is assumed by:

$$\frac{\partial c_i(x=L_C,t)}{\partial t} = 0 \quad (19)$$

1.2.2 Pore model

The concentration in the particles liquid phase $c_{\text{p},i}(x,t)$ of the TDM can be achieved by different pore model approaches. The assumption of a equally distributed concentration within the particle leads to the lumped rate model (LRM) that is derived later. A more general approach would be the general rate model (GRM) [Eq. (27)] which additionally considers radial pore diffusion as illustrated in Figure 7.

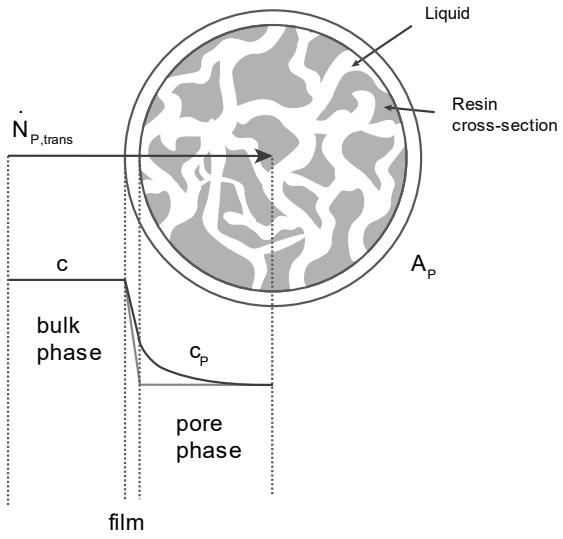

Figure 7: The transport of the substance from the bulk phase to the particle phase occurs through the liquid film. The concentration profiles depicted with the grey line represents the lumped rate model, assuming a uniform concentration within the particle. The concentration depicted by the curved black line represents the transport through the particle, applying the general rate model (GRM).

The particle is divided into a liquid phase volume $V_{\mathrm{p,liquid}}$ [m³] and solid phase volume $V_{\mathrm{p,solid}}$ [m³], representing the resin skeleton volume or resin backbone. In the following, the pore model is derived.

The following molar material balance boundary surrounds the particles liquid phase:

$$\frac{\partial N_{\mathrm{p},i}(x,t)}{\partial t} = \dot{N}_{\mathrm{trans,p},i}(x) - \dot{N}_{\mathrm{bound,p},i}(x) \qquad (20)$$

The material inflow from the interstitial through the film layer is defined similarly to $\dot{N}_{\mathrm{trans},i}(x)$ in Eq. (9) as:

$$\dot{N}_{\mathrm{trans,p},i}(x) = k_{\mathrm{eff},i}\left(c_i(x,t) - c_{p,i}(x,t)\right) A_{\mathrm{p}} \qquad (21)$$

and the outflow due to binding to the resin skeleton $q_i(x,t)$ [molm^{-3}] is defined as:

$$\dot{N}_{\mathrm{bound,p},i}(x) = \frac{dq_i(x,t)}{dt} V_{\mathrm{p,solid}} = \frac{dq_i(x,t)}{dt}\left(1-\varepsilon_{\mathrm{p}}\right)\cdot V_{\mathrm{p}}. \qquad (22)$$

In Eq. (22) the skeleton volume can be described by the particle porosity defined as:

$$\varepsilon_\mathrm{p} = \frac{V_\mathrm{p,liquid}}{V_\mathrm{p}} \; or \; \left(1-\varepsilon_\mathrm{p}\right) = \frac{V_\mathrm{p,solid}}{V_\mathrm{P}}. \tag{23}$$

Assuming a constant particle volume, the left hand-side equation can be transformed to:

$$\frac{\partial N_{\mathrm{p},i}(x,t)}{\partial t} = \varepsilon_\mathrm{p} V_\mathrm{p} \frac{\partial c_{\mathrm{p},i}(x,t)}{\partial t} \tag{24}$$

which inserted with Eqs. (21) and (22) into Eq. (20) results in:

$$\varepsilon_\mathrm{p} V_\mathrm{p} \frac{\partial c_{\mathrm{p},i}(x,t)}{\partial t} = k_{\mathrm{eff},i}\left(c_i(x,t) - c_{p,i}(x,t)\right) A_\mathrm{p} - \frac{dq_i(x,t)}{dt}\left(1-\varepsilon_\mathrm{p}\right)\cdot V_\mathrm{p} \tag{25}$$

where the particles surface to volume ratio [Eq. (10)] and further simplification leads to the LRM:

$$\frac{\partial c_{\mathrm{p},i}(x,t)}{\partial t} = \frac{3}{r_\mathrm{p}} \frac{k_{\mathrm{eff},i}}{\varepsilon_\mathrm{p}}\left(c_i(x,t) - c_{p,i}(x,t)\right) - \frac{\left(1-\varepsilon_\mathrm{p}\right)}{\varepsilon_\mathrm{p}} \frac{dq_i(x,t)}{dt} \tag{26}$$

The general rate model (GRM) accounts for diffusion within the particles liquid phase along the particle radius. Therefore, Eq. (26) can be changed including an Fickian pore diffusion:

$$\frac{\partial c_{\mathrm{p},i}(x,r,t)}{\partial t} = D_\mathrm{pore}\left(\frac{\partial^2 c_i(x,r,t)}{\partial r^2} + \frac{2}{r}\frac{\partial c_i(x,r,t)}{\partial r}\right) - \frac{\left(1-\varepsilon_\mathrm{p}\right)}{\varepsilon_\mathrm{p}} \frac{dq_i(x,r,t)}{dt} \tag{27}$$

where the pore diffusion parameter D_pore [m²s⁻¹] and the first term describe symmetrical diffusion and the second term the convection towards the center of the bead.

1.2.3 Binding models

1.2.3.1 Affinity chromatography binding model

The binding of a protein *P* to an affinity ligand *L* builds a protein ligand complex LP_complex. The reversible adsorption-desorption reaction can be expressed by:

$$P + L \underset{k_\mathrm{des}}{\overset{k_\mathrm{ads}}{\rightleftarrows}} LP_\mathrm{complex} \tag{28}$$

which leads, based on the law of mass action, to the following binding model:

$$\frac{dq(x,t)}{dt} = k_{\text{ads}}[P][L] - k_{\text{des}}q(x,t) \quad (29)$$

where LP_{complex} is replaced by $q(x,t)$. The amino acids involved in the complex formation of the protein and ligand are known to be protonated at low pH which prevents complex formation. The sum of protein P_{total} must equal the sum of protein states which in turn must equal the sum of bound and solute protein:

$$[P_{\text{total}}] = [P] + [P^+] + \left[LP_{\text{complex}}\right] = q(x,t) + c_{\text{p}}(x,t). \quad (30)$$

and likewise for the total ligand L_{total}:

$$[L_{total}] = [L] + [L^+] + \left[LP_{\text{complex}}\right] = q_{max}. \quad (31)$$

where the LP_{complex} can be replaced by $q_i(x,t)$. The maximum achievable concentration bound to the resin is represented by q_{max} [molm^{-3}]. To accomplish an expression for P and L, an expression for the protonated version of the protein and ligand is derived. The pH or specifically the hydrogen ion concentration H^+ induces the protonation described by the reversible reaction for the protein:

$$P^+ \overset{K_a'}{\leftrightarrow} H^+ + P \quad (32)$$

$$[P^+] = \frac{[H^+][P]}{K_a'} \quad (33)$$

and similarly for the ligand L:

$$L^+ \overset{K_a''}{\leftrightarrow} H^+ + L \quad (34)$$

$$[L^+] = \frac{[H^+][L]}{K_a''}. \quad (35)$$

Replacing the protonated state in Eq. (30) by Eq. (32) leads to:

$$[P] + \frac{[P][H^+]}{K_a'} + q(x,t) = q(x,t) + c_{\text{p}}(\text{x},\text{t}) \quad (36)$$

which can be simplified to:

$$[P] = \frac{c_\mathrm{p}(x,t)}{\left(1+\frac{[H^+]}{K_a'}\right)} = \frac{c_\mathrm{p}(x,t)}{\left(1+10^{\mathrm{p}K_\mathrm{a}'-pH}\right)}. \tag{37}$$

for the protein concentration available for complex formation. Likewise, replacing the protonated ligand in Eq. (34) by Eq. (31) leads to:

$$[L] + \frac{[L][H^+]}{K_a''} + q(x,t) = q_{max}. \tag{38}$$

which can be transformed to:

$$[L] = q_{max}\frac{\left(1-\frac{q(x,t)}{q_{max}}\right)}{\left(1+\frac{[H^+]}{K_a''}\right)} = q_{max}\frac{\left(1-\frac{q(x,t)}{q_{max}}\right)}{\left(1+10^{\mathrm{p}K_\mathrm{a}''-pH}\right)}. \tag{39}$$

The expression in the denominator was transformed with the log of basis 10 to achieve an expression of pH and pK_a. The derived equations for the ligand Eq. (39) and protein Eq. (37) can be inserted to Eq. (29) which results in:

$$\frac{dq(x,t)}{dt} = k_\mathrm{ads}q_{max}\frac{c_\mathrm{p}(x,t)}{\left(1+10^{\mathrm{p}K_\mathrm{a}'-pH}\right)\left(1+10^{\mathrm{p}K_\mathrm{a}''-pH}\right)}\left(1-\frac{q(x,t)}{q_{max}}\right) - k_\mathrm{des}q(x,t). \tag{40}$$

The kinetic form is obtained by dividing by k_des. Further, the sum of bound protein i of n species is considered for the multicomponent binding resulting in the isotherm expression for affinity chromatography:

$$k_{\mathrm{kin},i}\frac{dq_i(x,t)}{dt} = K_{\mathrm{eq},i}q_{max}\frac{c_{\mathrm{p},i}(x,t)}{\left(1+10^{\mathrm{p}K_\mathrm{a}'-pH}\right)\left(1+10^{\mathrm{p}K_\mathrm{a}''-pH}\right)}\left(1 - \sum_{i=1}^{n}\frac{q_i(x,t)}{q_\mathrm{max}}\right) - q_i(x,t) \tag{41}$$

Based on Eq. (41), the equilibrium and local state for a single component is given by:

$$q = q_\mathrm{max}\frac{K_\mathrm{eq}c_\mathrm{p}}{\left(1+10^{\mathrm{p}K_\mathrm{a}'-pH}\right)\left(1+10^{\mathrm{p}K_\mathrm{a}''-pH}\right)+c_\mathrm{p}} \tag{42}$$

which represents the Langmuir formulation.

1.2.3.2 Ion-exchange chromatography binding model

The interaction of protein and a charged adsorber can be considered a function of pH and ions in solution. In the past, adsorption modeling in IEX was dominated by stoichiometric adsorption models, especially the steric mass action (SMA) model [37]. The SMA model is derived in the supplementary and describes a reversible stoichiometric displacement of counter-ions and charged proteins on the adsorber surface. Limitations of the model describing protein elution behavior might be compensated by multiple binding states [38] or an activity coefficient [39]. The alternative colloidal binding models present a promising alternative class of models [40–42]. In contrast to stoichiometric models, colloidal models approximate the protein as a perfect sphere and assume a limiting adsorber surface. Electrostatic interactions are typically based on a mean-field approach using the Poisson -Boltzmann theory [43]. A colloidal particle adsorption (CPA) model for the nonlinear adsorption range of IEX, for multicomponent systems and with a similarly count of unknown parameters compared to SMA was derived by Briskot [42,44,45].

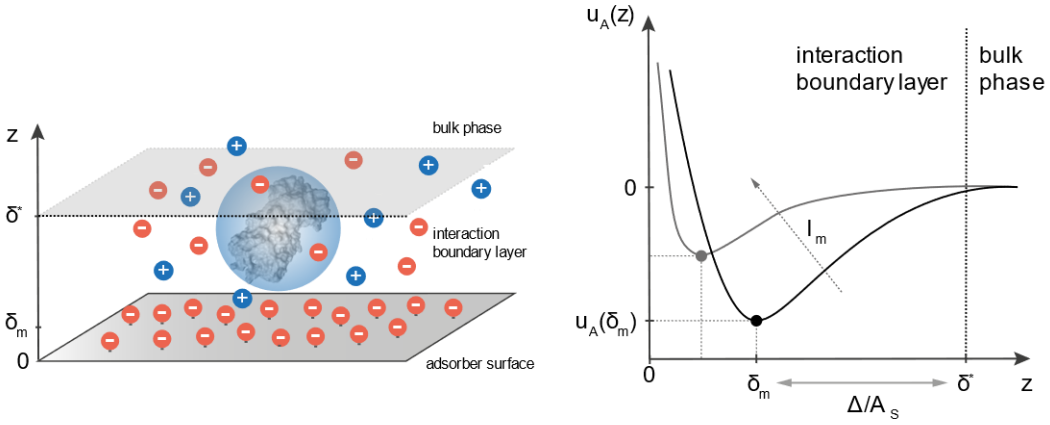

Figure 8: Schematic representation of the Colloidal particle adsorption (CPA) mechanism: Left represents a charged protein approximated by a perfect sphere colloid. The charged colloid interacts with the charged adsorber surface covered with immobilized charges. The interaction can be described by the interaction free energy represented on the right. Adsorption is considered solely within the interaction boundary layer. The thickness of the interaction boundary layer depends on the minimum interaction free energy which in turn depends on the ionic strength as schematically demonstrated.

Figure 8 presents a schematic representation of the electrostatic double layer interaction profile included in the CPA model. The interaction of a charged colloidal protein i with a charged adsorber surface in an electrolyte solution can be described by the interaction free energy $u_{A,i}$ [J] which is a function of the distance z [m]. The electrostatic interaction between the colloid and the surface, and thus adsorption, is limited within the interaction boundary layer constraint by the distance of minimum interaction free energy δ_m [m] and the

thickness of the boundary layer δ^* [m]. The protein bound to the adsorber surface is given by:

$$q_i = c_{\mathrm{p},i} K_i B_i \exp\left(-\frac{u_{lat,i}}{k_\mathrm{b} T}\right) \qquad (43)$$

where K_i [m] represents the partitioning coefficient, B_i [-] represents the available surface function, and the last term accounts for protein-protein interactions. The Boltzmann constant is represented by k_b [JK^{-1}], the temperature by T [K], and the lateral protein-protein interaction energy by $u_{\mathrm{lat},i}$ [J]. For the linear regime the protein adsorbed to the resin approaches zero and Eq. (43) reduces to:

$$q_i = c_{\mathrm{p},i} K_i = \frac{c_{\mathrm{p},i} \Delta_i k_\mathrm{b} T}{u_{\mathrm{A},i}(\delta_\mathrm{m})}\left(1 - \exp\left(-\frac{u_{\mathrm{A},i}(\delta_\mathrm{m})}{k_\mathrm{b} T}\right)\right) \qquad (44)$$

where $u_{\mathrm{A},i}$ is a function of the ionic strength I_m [molm^{-3}] and the characteristic protein charge Z [-]. The measure for the thickness of the interaction boundary layer defined as:

$$\Delta_i = A_{\mathrm{S},i}(\delta^* - \delta_\mathrm{m}) \qquad (45)$$

is a fitting parameter. The specific adsorber surface per skeleton volume is represented by $A_{\mathrm{S},i}$ [m^{-1}]. The pH dependency of the CPA model results from the change of the protein charge with pH.

For non-linear adsorption, the steric surface blocking effects are described by B_i and $u_{lat,i}$. The steric surface blockage is a function of the colloid radius and based on the scaled particle theory (SPT) [42,46]. For the electrostatic interactions of bound proteins, a hexagonal Yukawa lattice was used to describe $u_{lat,i}$ which is a function of the protein radius, the ionic strength and characteristic lateral charge $Z_{\mathrm{lat},i}$ of both proteins. Unknown model parameters, that need to be determined experimentally are Z_i, $Z_{\mathrm{lat},i}$, Δ_i, and $A_{\mathrm{S},i}$. A detailed description of the model can be found in previous publications [42,44,45].

1.3 Fundamentals of filtration

1.3.1 Dead-end filtration modeling

The flow through a porous filter membrane is typically controlled by a constant pressure difference ΔP [Pa] between the feed side and filtrate side of the membrane. The initial flow rate Q_0 [m^3s^{-1}] is mainly driven by the membrane hydraulic permeability [$ms^{-1}Pa^{-1}$] [30]:

$$L_\mathrm{p} = \frac{Q}{\Delta P A_\mathrm{m}} \qquad (46)$$

where the flow rate Q [m^3s^{-1}] linearly depends on the transmembrane pressure and the membrane area A_m [m^2]. With filtration time the filtrate flow decreases due to blocking. Assuming uniform cylindric pores, the classic filtration mechanisms follow the differential equation [47]:

$$\frac{d^2t}{dV^2} = k\left(\frac{dt}{dV}\right)^n \qquad (47)$$

where V [m^3] is the filtrate volume, the constants n [-] defines the blocking mechanism and k represents the blocking constant. A graphical illustration of blocking mechanisms was presented in Section 1.1.2. Exemplary for the pore blockage, also referred to as complete blockage, defined by $n = 2$ gives the following solution for Eq. (47):

$$t = C_2 - \frac{\ln(\mathrm{C}_1 + kV)}{k} \qquad (48)$$

The first derivative is given by:

$$\frac{dt}{dV} = -\frac{1}{\mathrm{C}_1 + kV} \qquad (49)$$

and the second derivative by:

$$\frac{d^2t}{dV^2} = \frac{k}{(C_1 + kV)^2} = k\left(-\frac{1}{\mathrm{C}_1 + kV}\right)^2 = k\left(\frac{dt}{dV}\right)^2 \qquad (50)$$

which demonstrates the form given in Eq. (47). The inverse function of Eq. (48) leads to an expression describing the filtrate volume over time:

$$V = \frac{C_3}{k} e^{(-kt)} - \frac{C_1}{k} \qquad (51)$$

The flow rate Q [$m^3 s^{-1}$] is given by:

$$\frac{dV}{dt} = Q = -C_3 \exp(-kt) \qquad (52)$$

The constants can be derived by two initial conditions. First, an initial flow Q_0 [$m^3 s^{-1}$] is assumed in Eq. (52) and second, the initial filtrate volume of zero is used in Eq. (51) which leads to $C_1 = C_3 = -Q_0$.

Further solutions of Eq. (47) for the classic blocking mechanisms are given in Table 1. During cake filtration the fouling adds a resistance layer in series to the membrane resistance. The other models block cylindrical pores (pore blockage, intermediate blockage) or reduce the effective pore size (pore constriction). The linear form can be useful to analyze filtration data and identify a blocking mechanism based on linear trends. However, filtration data possibly show mixed forms of blocking. Combined models and flow-controlled filtration, which is derived similarly to pressure-controlled filtration, are discussed in more detail in the following publications [30,48,49].

Table 1: Classic blocking equations for constant pressure filtration [30]. For illustration purposes, the constant β replaces the model-specific constant given in the last column.

Blocking model	n	Flow rate	Linear form	Constant β
Pore blockage	2	$\frac{Q}{Q_0} = \exp(-\beta t)$	$\ln\left(\frac{Q}{Q_0}\right) = -\beta t$	k_b
Pore constriction	$\frac{3}{2}$	$\frac{Q}{Q_0} = (1+\beta t)^{-2}$	$\sqrt{\frac{Q_0}{Q}} = \beta t + 1$	$\frac{k_\mathrm{p} Q_0}{2}$
Intermediate blockage	1	$\frac{Q}{Q_0} = (1+\beta t)^{-1}$	$\frac{Q_0}{Q} = \beta t + 1$	$k_\mathrm{i} Q_0$
Cake filtration	0	$\frac{Q}{Q_0} = (1+\beta t)^{-\frac{1}{2}}$	$\left(\frac{Q_0}{Q}\right)^2 = \beta t + 1$	$2k_\mathrm{c} Q_0^2$

1.3.2 Tangential flow filtration modeling

Tangential flow filtration is a commonly used method for concentrating products, particularly proteins. This process is typically operated at high protein concentrations. The pressure and flow performance of the filtration process is influenced by various protein characteristics, such as viscosity and osmotic pressure. Additionally, the presence of charged proteins can lead to

electrostatic interactions. In this section, the topic of permeate flow is discussed, followed by the role of electrostatic interactions during UF/DF.

1.3.2.1 Pressure and permeate flow model

The permeate flow or filtrate flow is controlled by the transmembrane pressure difference:

$$\Delta P_{TMP} = \frac{(P_{feed} + P_{retentate})}{2} - P_{permeate} \qquad (53)$$

which describes the pressure difference between the feed side and permeate pressure. Therefore, the feed pressure P_{feed} [Pa] and retentate side pressure $P_{retentate}$ [Pa] get averaged and the permeate side pressure $P_{permeate}$ [Pa] is subtracted. The resulting permeate flow typically increases with increasing TMP, but reaches a plateau as illustrated in Figure 9. The permeate flow during TFF processes can be described by gel-polarization models, resistance models, and osmotic pressure models [50]. First, the osmotic pressure model is discussed and subsequently the resistance model referred to as stagnant film model.

The osmotic pressure model in Eq. (54) describes the pressure driven permeate flow per membrane area J_v [ms^{-1}] based on the Kedem-Katchalsky equations:

$$J_v = L_p(\Delta P_{TM} - \Delta\Pi) \qquad (54)$$

The osmotic pressure ΔΠ [Pa] across the membrane can be considered equal to the osmotic pressure of the protein concentration in the retentate for a fully retentive membrane [51,52].

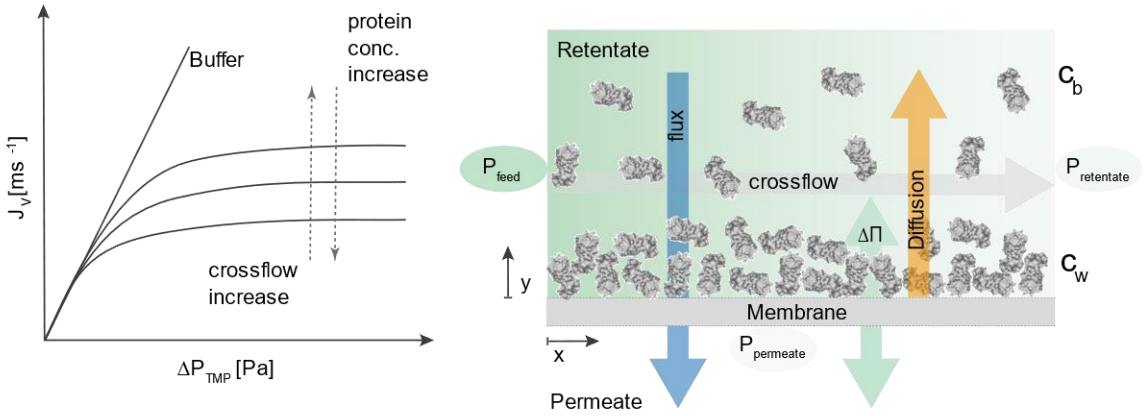

Figure 9: Tangential flow filtration: The figure on the left depicts the relationship between flux and TMP in TFF processes. As TMP increases, the flux also increases, but eventually reaches a plateau that is independent of TMP. On the other hand, an increase in crossflow leads to a decrease in boundary layer thickness, resulting in an increase in flux. However, an increase in protein concentration in the bulk leads to a decrease in flux due to the polarization effect. The figure on the right illustrates the concentration polarization phenomenon in TFF processes. The green color gradient represents the pressure loss along the membrane length, which increases depending on the membrane screen design, crossflow, and viscosity.

In addition, the pressure driven solute mass transfer through the membrane results in higher protein concentration towards the membrane surface. This effect is referred to as concentration polarization described by the stagnant film model and illustrated in Figure 9. Assuming a steady state, the one-dimensional solute flux through the membrane must be equal to the net solute flux towards the membrane:

$$\frac{\dot{N}_\mathrm{p}}{A_\mathrm{m}} = -J_\mathrm{v} c_\mathrm{p} = -J_\mathrm{v} c - D\frac{\partial c}{\partial y} \qquad (55)$$

including Fick's diffusion and a convective contribution. The term D [m^{2}s^{-1}] denotes the diffusion coefficient, $\dot{N}_\mathrm{p}$ [mols^{-1}] is the mass flow on the permeate membrane side, and c [molm^{-3}] is the local concentration in the positive y [m] direction. Note that filtrate flux J_v [ms^{-1}] is taken as positive quantity although the filtrate velocity is in the negative y direction. Integrating the Eq. (55) across the polarization boundary layer from 0 to δ [m] and from the constant wall concentration c_w [molm^{-3}] to the bulk concentration c_b [molm^{-3}] yields the Stagnant film model:

$$J_\mathrm{v} = \frac{D}{\delta}\ln\left(\frac{c_w - c_p}{c_b - c_p}\right) \qquad (56)$$

The permeate side c_p can be assumed to be zero for a fully retentive membrane. The ratio of the diffusion coefficient and the boundary layer thickness is usually combined to a single mass transfer coefficient. A more detailed derivation of the stagnant film model describing the polarization effect during TFF can be found in the following publication [53]. A constant diffusion coefficient and assuming a constant viscosity, limits the model's capability to describe concentration polarization of highly concentrated protein solutions. To include protein-protein interactions, the diffusive term in Eq. (55) can be assumed to be proportional to the gradient in the chemical potential μ [Jmol^{-1}] leading to an alternative expression for Eq. (55)[52,54]:

$$\frac{\dot{n}_\mathrm{p}}{A_\mathrm{m}} = -J_\mathrm{v} c_\mathrm{p} = -J_\mathrm{v} c - \frac{Dc}{RT}\frac{d\mu}{dy} \qquad (57)$$

The chemical potential can be rewritten in terms of the protein osmotic pressure Π [Pa]:

$$\frac{d\mu}{dy} = \frac{M_\mathrm{P}}{c}\frac{d\Pi}{dc}\frac{dc}{dy} \qquad (58)$$

Furthermore, the diffusion coefficient can be expressed as function of the solution viscosity:

$$D = D_0\left(\frac{\eta_0}{\eta}\right) \qquad (59)$$

where D_0 [m²s^{-1}] and η_0 [Pas] are the diffusivity of the protein free solution. The local viscosity is represented by η [Pas]. Eq. (58) and Eq. (59) inserted in Eq. (57) for a fully retentive membrane leads to the modified concentration polarization model:

$$J_\mathrm{v} = \frac{D_0}{\delta}\int_{c_\mathrm{b}}^{c_\mathrm{w}}\left(\frac{\eta_0}{\eta}\frac{M_\mathrm{P}}{RT}\frac{d\Pi}{dc}\right)\frac{dc}{c} \qquad (60)$$

A more detailed description of the model is given by the following publications [52,55]. The unknown wall concentration might be evaluated using the osmotic pressure model [52]. The crossflow is assumed to increase the permeate flow due to the reduction of boundary layer thickness. However, the crossflow Q [molm^{-3}] also leads to an increase in pressure drop within the feed channel in the form of [30]:

$$\Delta P = k_{\mathrm{m}} Q^{\alpha} \qquad (61)$$

where the constant k_{m} depends on the membrane properties such as the screen geometry and the feed channel height. The exponent α [-] changes between 1 - 2 dependent on the flow regime which can range from laminar to turbulent flow.

1.3.2.2 Electrostatic interaction

A protein in solution exposes amino acid groups on the surface. Oxides are usually negatively charged due to the dissociation of a proton ($\sim OH \rightarrow \sim O^- + H^+$) and amino groups become positively charged due to protonation ($\sim NH_2 + H^+ \rightarrow NH_3^+$). This leads to charges at the protein surface depending on the pK_{a} of the side chains and the surrounding pH. The surface charges can be summarized to a total surface charge density σ [Cm²] assuming a spherical colloid. This surface charge causes an electric field that interacts with ions in solution in a way to maintain electroneutrality. The layer compensating opposite charges is referred to as diffuse double layer and can be described by the mean-field Poisson-Boltzmann (PB) model [56,57]. First, charge density and electric potential Ψ [V] are related by the Poisson equation. Assuming radial symmetry, the Laplace operator $\nabla^2\Psi$ of the Poisson equation can be replaced leading to the radial form of the Poisson equation:

$$\frac{1}{r^2}\frac{d}{dr}\left(r^2\frac{d\Psi}{r}\right) = -\frac{\rho_e}{\varepsilon\varepsilon_0} \qquad (62)$$

where ρ_e [Cm^{-3}] represents the charge density, ε_0 [C²N^{-1}m^{-1}] is the vacuum permittivity, and ε [-] represents the relative permittivity. Since ions are free to move in solution the special distribution must be known. This local ion density can be described by the Boltzmann statistics. Assuming that only electric work $e\psi$ [J] has to be done to move an ion i of charge z_i [-] leads to the Boltzmann expression:

$$\rho_e = eN_A \sum z_i\, c_i^0\, e^{-\frac{z_i e\psi}{k_{\mathrm{b}}T}} \qquad (63)$$

where c_i^0 [molm^{-3}] is the bulk concentration of an ion, N_A [mol^{-1}] is the Avogadro constant and e [C] is the elementary charge. Combining the Poisson Eq. (62) and Boltzmann Eq. (63) leads to the following Poisson-Boltzmann expression:

$$\frac{1}{r^2}\frac{d}{dr}\left(r^2\frac{d\Psi}{r}\right) = -\frac{eN_A}{\varepsilon\varepsilon_0}\sum z_i\, c_i^0\, e^{-\frac{z_i e\psi}{k_{\mathrm{b}}T}} \qquad (64)$$

The ions attracted or repulsed by the electric field caused by the charged protein can lead to deviations between the retentate and permeate ion concentration during filtration with a semipermeable membrane. This effect is known as Gibbs-Donnan effect and can lead to undesired shifts in pH. The effect becomes predominant at high protein concentrations and low ionic strengths which is a common condition for industrial ultrafiltration processes. Furthermore, the protein volume exclusion needs to be considered at high protein concentration. More detailed description of this phenomenon can be found in literature [56–59].

2 Thesis outline

2.1 Research proposal

The biopharmaceutical industry is currently facing increasing competition, which has led to a demand for cost savings and efficiency, as highlighted in the introduction Chapter 1. In addition, new drug formats, such as non-standardized monoclonal antibodies, are introduced into drug development pipelines, making the application of standardized process conditions and control strategies almost impossible. Despite the advantages of mechanistic models in addressing these challenges, which have been highlighted by academia and demonstrated by the chemical industry, they are rarely applied in the biopharmaceutical industry. However, regulatory authorities encourage a scientifically sound understanding of the process to ensure process efficiency and drug safety.

The goal of this research is to develop a mechanistic model of an exemplary biopharmaceutical downstream process from a holistic perspective. Since the underlying mechanisms do not change between processes for different drug candidates, the knowledge and strategies gained from this research are expected to be transferable. This could lead industry to adapt to change and bring new candidates to market efficiently. However, for industrial purposes, the models must meet high standards to provide confidence in the results. To ensure confidence in the models, this work is dedicated on the three main requirements. First, the model must be able to respond to changing process conditions, similar to its real-world counterpart. Second, the scalability of the model must be demonstrated. Third, the predictability of the model outside its calibration range must be ensured.

A typical biopharmaceutical downstream process involves various chromatography, adjustment, and filtration steps. In this area, mechanistic models usually focus on individual steps or on sequences or networks of similar steps, such as different chromatography columns, while entire processes are usually modeled with relatively simple mass and energy balances. In addition, there is often a lack of application of the existing models to real process conditions and manufacturing data. To develop a comprehensive understanding of the models and process, it is essential to discriminate each

unit operation model. Particular attention should be given to the polishing chromatography, which is critical for ensuring product quality. Filtration steps range from dead-end depth filtration to tangential flow filtration to viral filtration. However, as the last unit operation of the downstream sequence, UF/DF is typically critical and shows a high complexity of the pressure flow relations. This is probably why the description of an entire UF/DF process for a biopharmaceutical process has not yet been shown.

A connected process model for the downstream should be able to describe the causes and effects of process parameters such as ion concentration, protein concentration, impurities, pH, and volume. The model should be applied to real data, including manufacturing data, to underline its relevance for industrial use. In conclusion, this research should address the challenge of describing an entire downstream process through mechanistic models. The results could contribute to an interconnected process understanding of cause and effect across the entire process flow. Thus, the model would have the potential to improve biopharmaceutical process development as a tool to understand scale effects and process variability, help in troubleshooting, support overall decision making, and improve experimental design.

2.2 Manuscript overview and author statement

This section provides an overview of this publication-based work. The task of modeling a downstream process was divided into sub-tasks. Chapter 3 presents the modeling of two consecutive IEX chromatography steps and the enclosing adjustment steps from lab to manufacturing scale. Chapter 4 addresses the pressure-flow modeling of the UF/DF process. Chapter 5 completes the downstream sequence with the missing steps of capture chromatography, adjustment, and filtration. In addition, the application of the process model to manufacturing data and predictability with respect to manufacturing variability is addressed. The manuscripts have been published internationally in established peer-reviewed journals and have not been used in any other publication-based work.

Chapter 3: Integrated process model for the prediction of biopharmaceutical manufacturing chromatography and adjustment steps

Federico Rischawy, Till Briskot, Adrian Schimek, Gang Wang, David Saleh, Simon Kluters, Joey Studts, Jürgen Hubbuch

Journal of Chromatography A (2022), Volume 1681

In this study, consecutive ion-exchange chromatography was of interest. The chromatography steps are critical for CQAs. The models are usually considered individually, and model limitations are rarely addressed. For model discrimination, challenging process conditions were used that could only be described by the CPA model. In addition, the associated simulation requires the ionic strength as a process input for ion exchange chromatography. Therefore, a mean-field approach was used to cover adjustment steps. The presented mechanistic models were validated as digital representations of the process at laboratory and production scale. As a potential application, the model was used to investigate the robustness of the process to input variations.

Chapter 4: Modeling of biopharmaceutical UF/DF from laboratory to manufacturing scale

Federico Rischawy, Till Briskot, Frederik Nitsch, David Saleh, Gang Wang, Simon Kluters, Joey Studts, Jürgen Hubbuch

Computers & Chemical Engineering (2023), Volume 177

The pressure and flow relationship of ultrafiltration and diafiltration (UF/DF) processes is complex and depends on the protein concentration. This may be one reason why UF/DF development in the biopharmaceutical industry is largely empirical and rarely mechanistic. In this study, a model for a biopharmaceutical UF/DF process is presented and applied to a Fab fragment from laboratory to production scale using an Ultracel Pellicon® 3 C-screen cassette. The model required offline viscosity data, membrane permeability, and a single ultrafiltration experiment. The model was then able to correctly respond to extrapolating process conditions with respect to the control parameters of crossflow and transmembrane pressure. This was demonstrated using a multivariate data set of ultrafiltration experiments with protein concentrations ranging from 5 g/L to 200 g/L. The model was able to describe the overall UF/DF process at laboratory and production scale.

Chapter 5: Connected mechanistic process modeling to predict a commercial biopharmaceutical downstream process

Federico Rischawy, Till Briskot, Nathalie Hopf, David Saleh, Gang Wang, Simon Kluters, Joey Studts, Jürgen Hubbuch

Computers & Chemical Engineering (2023), Volume 176

The objective of this study is to provide a comprehensive description of the downstream process for a Fab fragment. The study addresses the models that were not covered in previous chapters, such as capture chromatography, depth filtration, virus filtration, and adaptations. To model the capture step, a transport-dispersion model (TDM) combined with an extended Langmuir isotherm was utilized. The depth filtration was modeled using a combined pore blocking model. The tangential flow filtration model accounted for both the Donnan effects and flow limitations.

The final model, developed at the laboratory scale, was used to extrapolate to the manufacturing scale of 12,000 liters. Additionally, the model was provided with the initial inputs of 23 runs from the manufacturing process, and the model response was compared to the actual measurements.

3 Integrated process model for the prediction of biopharmaceutical manufacturing chromatography and adjustment steps

F. Rischawy[a,b], T. Briskot[b], A. Schimek[a,b], G. Wang[b], D. Saleh[b], S. Kluters[b], J. Studts[b], J. Hubbuch[a]*

[a] Karlsruhe Institute of Technology (KIT), Institute of Process Engineering in Life Sciences, Section IV: Biomolecular Separation Engineering, Karlsruhe, Germany

[b] DSP Development, Boehringer Ingelheim Pharma GmbH & Co. KG, Biberach an der Riß, Germany

* Corresponding author

Abstract

A fundamental process understanding of an entire downstream process is essential for achieving and maintaining the high-quality standards demanded for biopharmaceutical drugs. A holistic process model based on mechanistic insights could support process development by identifying dependencies between process parameters and critical quality attributes across unit operations to design a holistic control strategy.

In this study, state-of-the-art mechanistic models were calibrated and validated as digital representations of a biopharmaceutical manufacturing process. The polishing ion-exchange chromatography steps (Q-Sepharose FF, Poros 50 HS) were described by a transport-dispersive model combined with a colloidal particle adsorption model. The elution behavior of four size variants was analyzed and included in the model. Titration curves of pH adjustments were simulated using a mean-field approach considering interactions between the protein of interest and other ions in solution. By including adjustment steps the important process control inputs ionic strength, dilution, and pH were

integrated. The final process model was capable to predict online and offline data at manufacturing scale. Process variations at manufacturing scale of 94 runs were adequately reproduced by the model. Furthermore, the process robustness against a 20% input variation of concentration, size variant and ion composition, volume, and pH could be confirmed with the model.

The presented model demonstrates the potential of the integrated approach for predicting manufacturing process performance across scales and operating units.

3.1 Introduction

A shorter timeline of biopharmaceutical candidates to Phase I is even more expected after the COVID-19 pandemic outbreak [23]. Therefore, a fast process development leading to an optimized and robust process is essential. The complexity of biopharmaceutical downstream processes consists of the connection and interdependencies between multiple process units including chromatography, adjustment, and filtration steps. During process development the criticality of each process parameter across the manufacturing process needs to be determined at great expense for process control. To this end, Process System Engineering (PSE) techniques such as mechanistic models provide a systematic platform for challenges such as holistic process design [60–63]. Despite the many possible application and advantages, integrated process models have not yet been implemented in the pharmaceutical industry, although they are standard in the chemical industry [64]. One reason for the rare application of such process models is that there are not general models for each process step available that would make an application easily possible. Furthermore, model selection and parameter determination can be a major challenge.

Due to the lack of mechanistic understanding of most biopharmaceutical unit operations, empirical approaches such as Design of experiments (DOE) are mostly applied to investigate the impact of critical process parameters (CPPs) on critical quality attributes (CQAs) [65]. Disadvantages of such empirical approaches are the limited number of factors that can be considered due to the large number of experiments required leading to material limitations and time pressure. If, however, many historical process and development data is available, integrated regression models were shown to be an option [66]. This method is solely descriptive on historical data and improves with more data especially for nonlinear systems. Usually, new data is obtained from manufacturing at set-point conditions, which alone is not well suited for training machine learning algorithms [67]. Data outside set-point conditions is

usually rare and mostly obtained during process development. In contrast, prior knowledge stored in equations of mechanistic models, also called digital twins, allows for using information of a few experiments for model calibration and validation. Validated process models then describe the underlying physics and enable understanding of the systems overall behavior even under extrapolation conditions [68]. Previous studies demonstrated the advantages of modeling integrated chromatography steps like hydrophobic interaction chromatography (HIC) and anion-exchange chromatography (AEX) and cation-exchange chromatography (CEX) to identify optimal process conditions [69–72]. In the study of Huuk et al., model proteins (cytochrome c, chymotrypsin, ribonuclease A) were successfully used in linear gradient and break through operation mode. However, the capability to describe industrially relevant step elution and gradient elution under high loading conditions was not demonstrated [71].

Recently, the mechanistic understanding and application of models especially for industrial ion-exchange chromatography has shown significant progress regarding the calibration strategy and model limitations for single unit operations [45,73]. Without significantly increasing the number of parameters, the colloidal particle adsorption (CPA) model showed promising data to overcome the limitations of the SMA isotherm, especially at high column loadings [45]. Although the introduction of ionic strength to the feedstock possibly impacts impurity clearance in ion-exchange chromatography steps [74], the feedstock pH adjustment is not included mechanistically in previously published integrated process models. Recent interest in biopharmaceutical pH modeling can be found in the field of tangential flow filtration (TFF) to describe the Donnan effect [58,59]. The TFF pH models successfully apply the Poisson-Boltzmann (PB) mean-field theory to describe pH even at high protein concentrations. To date, there are no integrated mechanistic process models successfully applied to biopharmaceutical processes that combine feedstock adjustment and chromatographic steps to investigate the interactions between process units.

A digital process twin should use “the best available” physical models to describe the process [75]. In other words, a digital process twin is therefore an integrated representation of complete process trains and is therefore best based on a sequence of mechanistic models, where possible. In this study, a state-of-the-art integrated mechanistic model for an industrial downstream polishing sequence including pH adjustment steps was calibrated and validated in lab scale. For the adjustment steps a mean field theory model considering protein charge and ion in solution was applied. The presented model was challenged by extrapolating to manufacturing scale data demonstrating the predictivity of

the model. Furthermore, the applicability of the integrated model to investigate manufacturing process robustness was demonstrated by a Latin hypercube sampling (LHS). The manufacturing data might be used to further improve the model, which is outside the scope of this study.

3.2 Theory

3.2.1 Manufacturing process

A manufacturing process of a typical therapeutic protein is presented schematically in Figure 10. Used buffer components and pH are chosen on the basis of the manufacturing scale used to validate the integrated model of our study. The downstream sequence starts with a capture chromatography step followed by virus inactivation and depth filtration (Unit: I - III). The sequence of interest for this study is marked by a red dashed circle which surrounds the polishing sequence (Unit: IV – VIII). The first step IV of this sequence is a pH adjustment step from pH 7 to pH 8 with 1 M Tris. The loading material of step IV includes glycine and Tris as buffer components. The product of step IV is further purified in one or two polishing trains (1,2) of unit V to VII depending on the maximal loading capacities of step V. The first polishing chromatography is an anion-exchange chromatography step in flow through mode. The resulting product pool is adjusted to pH 4.9 with 1 M acetic acid (AcOH) and transferred to the cation-exchange chromatography column. The CEX elution is achieved by a salt step elution at pH 5.0. The polishing trains are subsequently pooled, and pH adjusted in step VIII to pH 5.5 by 0.1 M NaOH. The final process sequence comprises to virus filtration and tangential flow filtration (TFF) (Unit: VIII – X).

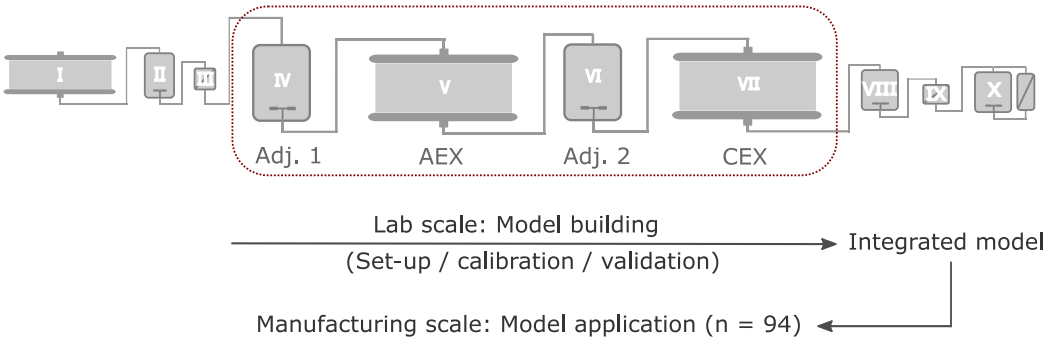

Figure 10: Scheme of manufacturing process: I - Capture, II - Virus inactivation, III - Depth filtration, IV Adjustment 1 (Adj. 1), V AEX, VI Adjustment 2 (Adj. 2), VII CEX, VIII Adjustment 3 (Adj. 3), IX Virus filtration, X tangential flow filtration. The dashed red circle surrounds the polishing sequence of interest. Depending on the load condition of the AEX unit the polishing sequence is performed in two trains (from V to VII) and pooled prior to VIII Adjustment 3.

3.2.2 Chromatography model

Any mechanistic description of chromatographic steps consists of an model describing transport processes and a model assumption describing protein adsorption onto the stationary phase. In our study we employed the Transport dispersive model (TDM) combined with the Colloidal particle adsorption (CPA) model. The chromatography column of length L_C [m] and diameter d_C [m] is assumed to contain spherical resin beads of equal particle radius r_p [m]. The transport dispersive model (TDM) is a partial differential equation (PDE) derived by a differential mass balance of the liquid phase of the column. The TDM in Eq. (65) describes the change in concentration in the solute bulk c_b [molm^{-3}] of component j over time and over column length $x \in [0, L_\mathrm{C}]$. The concentration c_P [molm^{-3}] is solute bulk in the particles liquid phase.

$$\begin{aligned}\frac{\partial c_{\mathrm{b},j}}{\partial t}(x,t) = & -u_\mathrm{int}(t)\frac{\partial c_{\mathrm{b},j}}{\partial x}(x,t) + D_\mathrm{ax}\frac{\partial^2 c_{\mathrm{b},j}}{\partial x^2}(x,t) \\ & -\frac{1-\varepsilon_\mathrm{int}}{\varepsilon_\mathrm{int}}\frac{3}{r_\mathrm{p}}k_{\mathrm{eff},i}\left(c_{\mathrm{b},j}(x,t) - c_{\mathrm{p},j}(x,t)\right)\end{aligned} \tag{65}$$

Parameters of the model are the interstitial velocity of the mobile phase u_int [ms^{-1}], the axial dispersion coefficient D_ax [m^{2}s^{-1}], the interstitial fraction ε_int[-] and the effective mass transfer coefficient k_eff [ms^{-1}] [27].

The PDE is completed with Danckwert's boundary conditions at the column inlet and outlet [36].

$$\frac{\partial c_{b,j}}{\partial t}(x=0,t)=\frac{u_{int}(t)}{D_{ax}}\left(c_{b,j}(x=0,t)-c_{inlet,j}(t)\right) \tag{66}$$

$$\frac{\partial c_{\mathrm{b},j}}{\partial t}(x=L_{\mathrm{C}},t)=0 \tag{67}$$

A lumped rate model with an effective mass transfer equation $k_{\mathrm{eff,j}}$ as presented in Eq. (65) and Eq (68) was used to describe the mass transfer from the void fraction to the liquid phase of the particle. The model assumes a constant c_{p} inside the particle and lumps transport mechanism to $k_{\mathrm{eff},j}$ described by

$$\frac{\partial c_{\mathrm{p},j}}{\partial t}(x,t)=\frac{3}{r_{\mathrm{p}}}\frac{k_{\mathrm{eff},j}}{\varepsilon_{\mathrm{P}}}\left(c_{\mathrm{b},j}(x,t)-c_{\mathrm{p},j}(x,t)\right)-\frac{1-\varepsilon_{\mathrm{P}}}{\varepsilon_{\mathrm{P}}}\frac{\partial q_{\mathrm{v},j}}{\partial t}(x,t). \tag{68}$$

The solute adsorbed on the particles stationary phase q_{v} [molm^{-3}] is referring to the adsorber skeleton volume. The surface density of the protein is given by $q_j = q_{\mathrm{v},j}A_{\mathrm{s},j}^{-1}$ [molm^{-2}] [45]. In this study, a constant specific adsorber surface per skeleton volume A_{s} [m^{-1}] was assumed for all components.

The adsorption and desorption rate of a protein on the adsorber surface was described by a colloidal particle adsorption (CPA) model. [45]. This model assumes the protein j to be a perfect sphere with radius a_j [m]. Further, it is assumed that temperature remains constant at $T = 298.15$ K and the relative permittivity at $\varepsilon = 78.3$ (water) in the mobile phase. The adsorber surface A in electrolyte solution with ionic strength I_{m} [molm^{-3}] is assumed to be solid and planar with a ligand density Γ_{L} [molm^{-2}] and the surface charge density σ_{A} [Cm^{-2}]. The protein bound to the resin skeleton volume $q_{\mathrm{v},i}$ is given by

$$\frac{\partial q_{\mathrm{v},i}}{\partial t}= k_{\mathrm{kin},i}\left(K_{\mathrm{v},i}c_{\mathrm{p},i}-q_{\mathrm{v},i}\right). \tag{69}$$

The kinetic parameter is given by Eq. (70) where $u_{\mathrm{A},i}\left(\delta_{\mathrm{m},i}\right)$ [J] represents the minimum of the interaction energy and depends on protein charge, ionic strength I_{m} and pH. The equation includes the Boltzmann constant k_{b} [JK^{-1}] and the fitting parameter $k^{*}_{\mathrm{kin},i}$ [s^{-1}] which defines the rate of adsorption/desorption.

$$k_{\mathrm{kin},i}=k^{*}_{\mathrm{kin},i}\frac{1}{2}\left(\frac{u_{\mathrm{A},i}\left(\delta_{\mathrm{m},i}\right)}{k_{\mathrm{b}}T}\right)^{2}\frac{1}{\cosh\left(\frac{u_{\mathrm{A},i}\left(\delta_{\mathrm{m},i}\right)}{k_{\mathrm{b}}T}\right)-1} \tag{70}$$

The equilibrium coefficient $K_{\mathrm{v},i}$ [-] in Eq. (69) is given by

$$K_{\mathrm{v},i} = \Delta_i B_i(\Theta) \frac{k_\mathrm{b} T}{u_{\mathrm{A},i}\left(\delta_{\mathrm{m},i}\right)} \exp\left(-\frac{u_{\mathrm{lat},i}}{k_\mathrm{b} T}\right)\left(1 - \exp\left(-\frac{u_{\mathrm{A},i}\left(\delta_{\mathrm{m},i}\right)}{k_\mathrm{b} T}\right)\right), \tag{71}$$

and depends on the available surface function $B_i(\Theta)$ [-]

$$B_i(\Theta) = (1-\Theta)\exp\left(-\frac{\pi a_i^2 \sum_j q_j N_\mathrm{A} + 2\pi a_i \sum_j a_j q_j N_\mathrm{A}}{(1-\Theta)} - \frac{\pi a_i^2 \left(\sum_j a_j q_j N_\mathrm{A}\right)^2}{(1-\Theta)^2}\right) \tag{72}$$

The available surface function contains the surface coverage Θ [-] given by

$$\Theta = \pi N_\mathrm{A} \sum a_i^2 \frac{q_{\mathrm{v},i}}{A_{\mathrm{s},i}}. \tag{73}$$

The interaction boundary layer thickness Δ_i [-] in Eq. (71) is an unknown parameter that needs to be estimated *via* experimental data. The lateral interaction energy between the protein of interest and all other adsorbed proteins is represented by $u_{\mathrm{lat},i}$ [J] in Eq. (71). The lateral interaction energy depends on the characteristic lateral charge $Z_{\mathrm{lat},i}$ [-] which is an additional parameter to be estimated. The Avogadro number is represented by N_A.

Change of counter ions in the diffuse layer caused by protein adsorption and desorption is accounted by the neutrality condition in Eq. (74). The equation includes the counter-ions per adsorber surface q_c [molm^{-2}], the charge compensated by the adsorbed protein $z_{\mathrm{c},i}$ and the elementary charge e [C].

$$\sigma_\mathrm{A} - \mathrm{e} N_\mathrm{A}\left(\mathrm{sgn}(\sigma_\mathrm{A}) q_\mathrm{c} - \sum_i z_{\mathrm{c},i} q_i\right) = 0 \tag{74}$$

A more detailed description of the CPA model can be found in the following publications. [42,45].

3.2.3 Adjustment model

The adjustment model described in the following is used to predict the amount of titrant needed to achieve a desired pH value. It accounts for the ion composition, protein concentration, and the pH of the initial protein solution. The pH of the solution is a complex function that depends on several factors, including the applied buffer system, the protein concentration, and the protein charge, with the latter being a function of the ionic strength and pH itself. The mechanisms involved in predicting titration curves of protein mixtures in this study are based on the model presented by Briskot et al. with the difference that the tank system in this study is considered a closed system [58]. This is

achieved by the boundary condition presented in Eq. (80). For reasons of clarity the model is presented in this chapter.

The pH adjustment tank is considered a system of mixed ion solution and perfect sphere proteins in electroneutral equilibrium. To derive a mathematical expression of the electrostatic interaction of the proteins surface charge and ions in solution a Wigner-Seitz (WS) cell approximation was considered. The advantage of the applied WS cell model is that each cell represents the entire adjustment tank illustrated in Figure 11.

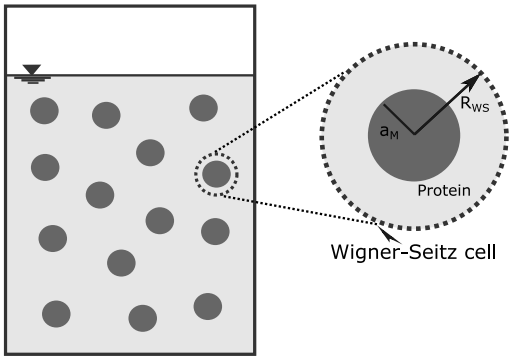

Figure 11: Schematic illustration of the cell model approximation of the adjustment tank by a Wigner-Seitz cell model. The tank is divided into multiple identical Wigner-Seitz cells which radius depends on the protein concentration.

Thus, the problem is reduced to a single and electroneutral Wigner-Seitz cell with a charged protein in the center. Inside the WS cell the solute concentration $c_{i,j}(r)$ [molm^{-3}], ionic strength I_m [molm^{-3}], and pH are a function of the radial position driven by the radial electrostatic potential between the protein outer radius a_M [m] and the radius of the WS cell R_WS given by

$$R_\mathrm{WS} = \left(\frac{3}{4\pi N_\mathrm{A} c_\mathrm{M}}\right)^{\frac{1}{3}}. \tag{75}$$

The $\overline{\mathrm{pH}}$ and ion concentration $\bar{c}_{i,j}$ as average values within the WS cell correspond to the measured pH and concentration. The proteins surface charge density σ_M [Cm^{-2}] given by

$$\begin{aligned}\sigma_\mathrm{M}(\mathrm{pH}_0) = \mathrm{e}N_\mathrm{A}\sum_k \Gamma_k\Big((\zeta_k - 1)[1 + 10^{\mathrm{p}K_k - \mathrm{pH}_0}]^{-1} \\ + \zeta_k[1 + 10^{\mathrm{pH}_0 - \mathrm{p}K_k}]^{-1}\Big),\end{aligned} \tag{76}$$

depends on the pH_0 at the proteins surface. Based on the Boltzmann relation this surface pH_0 relates to the average $\overline{\mathrm{pH}}$ by

$$\mathrm{pH}_0 = \overline{\mathrm{pH}} + \frac{1}{\ln(10)} \frac{\mathrm{e}}{k_\mathrm{b} T} \left(\psi_0 - \overline{\psi}\right), \tag{77}$$

and in turn depends on the average electrical potential $\overline{\psi}$ [V] [76]. Charged amino acids were considered mainly at the protein surface in accordance with Briskot [58]. Therefore, the surface density Γ_k [molm^{-2}] in Eq. (76) is directly related to the number of amino acids in the primary structure. The charge of the protonated side chain is represented by ζ_k, e [C] represents the elementary charge and pK_k the dissociation constant of the k-th amino acid side chain. The resulting proteins surface charge density σ_M is required in the following Eq. (78) and Eq. (81).

In the following the electric potential $\overline{\psi}$ as required for Eq. (77) inside the WS is discussed. A basic Stern model was introduced to describe the electrostatic potential inside the WS cell resulting in a linear charge-free Stern layer domain and a diffuse layer. The linear domain ranges from the protein surface ψ_0 to the origin of the diffuse layer ψ_D. Within the Stern layer the electrostatic potential of the proteins surface ψ_0 drops linearly to the origin of the diffuse layer ψ_D [77]. The linear drop is given by Eq. (78) and depends on the stern capacitance

$$C_\mathrm{S} = \frac{\sigma_\mathrm{M}(\psi_0)}{\psi_0 - \psi_\mathrm{D}}. \tag{78}$$

Within the diffuse layer driving electrostatic potential ψ can be described by the PB equation system Eq. (79). To calculate the arising potential the Poisson equation (79) is solved under the boundary condition of the Wigner-Seitz (WS) cell and the Boltzmann relation Eq. (82). In contrast to Briskot et al., describing a semipermeable filtration system, the tank can be considered as a closed system with the potential vanishing at $r = R_\mathrm{WS}$ represented by the first boundary condition given in Eq. (80). The second boundary condition in Eq. (81) ensures electroneutrality within the WS cell.

$$\frac{\partial^2 \psi}{\partial r^2}(r) + \frac{2}{r}\frac{\partial \psi}{\partial r} = -\frac{\mathrm{e} N_\mathrm{A}}{\varepsilon \varepsilon_0} \sum_i \sum_j z_{i,j} c_{i,j}(r) \tag{79}$$

$$\psi(r = R_\mathrm{WS}) = 0 \tag{80}$$

$$\frac{\partial \psi}{\partial r}_{r = a_\mathrm{M}} = -\frac{\sigma_\mathrm{M}(\psi_0)}{\varepsilon \varepsilon_0} \tag{81}$$

$$c_{i,j}(r) = \overline{c}_{i,j}(\overline{\mathrm{pH}}) \exp\left(-z_{i,j} \frac{\mathrm{e}}{k_\mathrm{b} T} \left(\psi(r) - \overline{\psi}\right)\right) \tag{82}$$

The resulting PB equation can be solved numerically under the stated boundary conditions and reference electrostatic potential $\overline{\psi}$ and $\overline{\mathrm{pH}}$. This is achieved by solving the equation system including the PB equation iteratively until Eq. (83) and Eq. (84) are fulfilled.

$$\overline{\psi} = -\frac{k_\mathrm{b}T}{\mathrm{e}z_{i,j}}\ln\left(\frac{3}{(R_\mathrm{WS}^3 - a_\mathrm{M}^3)}\int_{a_\mathrm{M}}^{R_\mathrm{WS}}\exp\left(-z_{i,j}\frac{\psi(r)}{k_\mathrm{b}T}r^2 dr\right)\right) \tag{83}$$

$$0 = \sum_i\sum_j z_{i,j}c_{i,j}(r = R_\mathrm{WS}) = \sum_i\sum_j z_{i,j}\bar{c}_{i,j}(\overline{pH})\,exp\left(z_{i,j}\frac{e\bar{\psi}}{k_\mathrm{b}T}\right) \tag{84}$$

The concentration $c_{i,j}$ of ionization state j of the i-th solute are required in Eq. (83) and can be derived by the total concentration c_i and pH according to Ladwig [59]. The concentration of the fully protonated state $c_{i,0}$ is given by Eq. (85), where c_{H^+} represents the hydrogen ion concentration and K the dissociation constant of solutes.

$$c_{i,0} = \frac{c_{i,\mathrm{total}}}{1 + \sum_{j=1}^{N_{k_i}}\frac{\prod_{j=1}^{N_{k_i}}K_{i,j}}{(c_{H^+})^j}} \tag{85}$$

All the other dissociation states of the solute are given based on the concentration of the fully protonated state and pH by

$$c_{i,j} = c_{i,0}\frac{\prod_{j=1}^{N_{k_i}}K_{i,j}}{(c_{H^+})^j}. \tag{86}$$

A shift of the ideal pK_k according to Davies equation is a function of ionic strength I_m for conditions $I_m \lessapprox 0.3$ molL^{-1}. The fully protonated state is represented by ζ_i of the k-th pK value of solute i. The Debye Hueckel constant A_H of 0.5 L$^{0.5}$mol$^{-0.5}$ and the constant b of 0.2 were applied [78].

$$\mathrm{p}K_{i,k}^* = \mathrm{p}K_{i,k} + A_\mathrm{H}(2(\zeta_i - k) + 1)\left(\frac{\sqrt{I_\mathrm{m}}}{1 + \sqrt{I_\mathrm{m}}} - bI\right) \tag{87}$$

To find the amount of titrant required to reach the target pH the concentration in the tank was updated iteratively. The addition of titrant was adjusted by an increase in volume V_t [L/L] of titrant concentration c_t [mol/L] by

$$c_{i,\mathrm{total}} = \frac{c_{\mathrm{i,total}} + c_{\mathrm{t}} V_{\mathrm{t}}}{(1 + V_{\mathrm{t}})}, \tag{88}$$

yielding the target pH. The protein concentration $c_{\mathrm{M},i}$ was adjusted accordingly by

$$c_{\mathrm{M},i} = \frac{c_{\mathrm{M},i}}{(1 + V_{\mathrm{titrant}})}. \tag{89}$$

3.3 Material and methods

3.3.1 Protein and adsorbers

The protein in this study was a therapeutic protein with a molecular weight M_{w} of approximately 50 kDa. The protein radius a_{i} [m] was estimated based on the molecular weight with an empirical correlation applied by Briskot et al. 2021 and used in the adjustment and CPA model [42] [79]. The experiments were performed on the AEX resin Q-Sepharose FF (Cytiva, Uppsala, Sweden) and CEX resin Poros 50 HS (Thermo Fisher Scientific, Waltham, Massachusetts, USA). The backbone of Q-Sepharose FF consists of highly crosslinked agarose based matrix and quaternary amine ligands whereas the Poros 50 HS resin consists of crosslinked poly[styrene divinylbenzene] with sulphopropyl ligands.

3.3.2 Buffer and titration

The pH adjustment model has no fitting parameter and thus no calibration experiments were needed. For all experiments the parameters in Table 1 and pK_{a} values listed in Table 2 and Table 3 were applied. The capture step buffer substance was glycine, the AEX buffer was based on Tris and CEX buffer on acetate. Buffer component concentration were analyzed for a manufacturing run for the capture pool. Addition of buffers and salts by adjustment steps was calculated by mass balancing. The charged amino acids were quantified based on the sequence. In general, experiments used for model calibration have the suffix "_C" and validation experiments a "_V".

Table 2: pH adjustment model parameters.

Parameter	Value
Stern capacitance C_S [Fm^{-2}] [58]	0.2
Colloid radius a_M [nm]	2.35
Relative permittivity of water ε [-]	78.3
Molecular weight M_W [kDa]	~ 50
Temperature T [K]	298.15

Table 3: Thermodynamic ideal pKa values of buffer systems with fully protonated charge ζ_i.

Buffer	p$K_{i,1}$	p$K_{i,2}$	ζ_i
Glycine pK	2.34	9.60	1
Tris pK	8.08	-	1
Acetate pK	4.76	-	0

Table 4: Average residual pK values and the charge ζ_k of the fully protonated side chain [80].

Residual	pK_k	ζ_k
N-terminal	7.5	1
Glutamic acid	4.4	0
Aspartic acid	4.0	0
Tyrosine	9.6	0
Lysine	10.4	1
Arginine	12.0	1
Histidine	6.3	1
C-Terminal	3.8	0

Small scale titrations were performed to validate the predictivity of the model. Adj.B_V was a pure buffer titration experiment of the capture elution buffer without protein. For Adj.1-3_V load material from a manufacturing run was used for the respective steps Adj.1 and Adj.2 of the polishing sequence. The ion

composition of Adj.1-2_V was estimated *via* analytical ion-exchange chromatography for sodium and Tris, and *via* reverse phase chromatography for glycine and acetate. For Adj.3_V the elution buffer composition was assumed. The load conditions are listed in Table 4.

Table 5: Initial conditions of pH adjustment model validation experiments. The titrations were performed at room temperature.

Exp.	pH	pH target	Titrant	Protein conc. [g/L]	Sodium [mM]	Chloride [mM]	Glycine [mM]	Tris [mM]	Acetate [mM]
Adj.B_V	2.4	8.1	1 M Tris	0	31.0	42.0	40.0	0.0	0.0
Adj.1_V	6.9	8.0	1 M Tris	4.55	22.2	39.6	41.3	14.2	0.0
Adj.2_V	8.0	5.0	1 M AcOH	3.95	26.2	40.0	41.6	26.7	0.0
Adj.3_V	5.0	5.4	0.1 M NaOH	5.16	110	75	0.0	0.0	50

3.3.3 Column experiments

AEX experiments were conducted on a 12.1 mL self-packed column of 1 cm diameter and 15.4 cm height. The calibration experiments were designed to cover a realistic process range and investigate the interaction based on varying pH, flow rate and ionic strength as shown in Table 5. The equilibration and running buffer were pH adjusted 50 mM Tris buffer.

Table 6: Summary of calibration and validation experiments used for AEX model development.

No	pH	Cond. [mS/cm]	Loading density [g/L]	Flow [cm/h]
AEX_C1	7.7	5.4	187	77
AEX_C2	8.3	2.8	187	231
AEX_V1	8.0	3.7	100	116

CEX experiments were conducted on a prepacked Poros 50 HS (Repligen GmbH, Ravensburg, Germany) column of 10.0 mL column volume (CV), 1.1 cm diameter, and 10 cm height. The running buffer was a pH adjusted 50 mM acetic acid (AcOH) buffer for all runs. Additional low load linear gradients

elution (LGE) experiments were performed with purified size variants 4 and 5 to obtain a pH dependency for those species of interest and information for parameter estimation [81]. The load material was prepared by size exclusion chromatography (SEC) with a HiLoad 26/600 Superdex 75 pg column (Cytiva, Uppsala, Sweden). The purification with the Superdex column was performed according to the manufacturer instructions. All calibration and validation experiments including the Superdex runs were conducted on an Äkta™ avant 25 system (Cytiva, Uppsala, Sweden). The size variants were analyzed with a HP-SEC Shodex KW403-4F column (Showa Denko Europe GmbH, Munich, Germany).

*Table 7: Overview of calibration and validation experiments for CEX model development. * Linear gradient runs were additionally performed with purified size variant 4 and 5.*

No.	pH	Gradient/step [mM]	Loading density [g/L]	Flow [cm/h]
CEX_C1	5.0	110	10	100
CEX_C2	5.0	34-500 / 20 CV	40	100
CEX_C3	5.0	34-500 / 20 CV	>40	120
CEX_C4	5.0	110	40	100
CEX_LG1-3*	4.6, 4.8, 5.0, 5.2	50-500 / 10, 20, 30 CV	1	100
CEX_V1	4.6	34-500 / 20 CV	20	100
CEX_V2	5.2	34-500 / 20 CV	20	100

3.3.4 Manufacturing scale: Model application

The integrated process model was used to predict the manufacturing process and thus to demonstrate an applicability of an integrated mechanistic model. In total 94 manufacturing runs were used to test the ability of the model to predict inferences about production variability based on varying inputs. The production scale column volume of AEX was 80 L with a bed height of 25.5 cm and the CEX had a column volume of 212 L and a column length of 27 cm. The linear flow rate of AEX was constant at 175 cm/h and for CEX the linear flow rate was constant at 150 cm/h. All other column properties except volume and length were held constant during scaling. The integrated process model transferred the loading concentration, loading size variance composition, ion composition, ion strength, and pH from one process step to the next. When the

maximum loading of 100 g/L for AEX was reached, the pool was divided and processed sequentially in separate process runs from AEX to CEX. This is indicated by (1) for train 1 and (2) for train 2. For two partial trains, the resulting CEX eluates were pooled. Target loading composition, concentration, volumes, and pH conditions were considered based on historical offline data to represent pH variance. The ion composition of the load was calculated based on mass balancing prior process steps.

The production run predictions were performed at set-point condition. However, the model can also be used to investigate the process performance for larger input variations, which can be interesting especially in process development to detect possible weak points. For this purpose and to demonstrate the model application, Latin hypercube sampling was applied, varying the process parameters volume, concentration, size variant composition, and ion composition in a range of +-20%. Additional variation was included by sampling CEX elution pH and ionic strength within the normal distribution observed in 94 manufacturing runs.

3.3.5 Software

The column models were solved by using ChromX (Cytiva, Uppsala, Sweden) with fractional step as time stepping scheme and linear Galerkin method for space discretization. The number of finite elements was set greater or equal to 60 and the step size smaller or equal to 0.7 seconds. MATLAB 2019b (The Mathworks Inc., Natick, MA, USA) was used to solve the PB Equation of the pH adjustment model using bvp5c. All process steps were connected and plotted in MATLAB.

3.3.6 Parameter estimation

System parameters were determined by pulse experiments. Dextran (2000 kDa) pulses were used for the estimation of the void volume ε_v, high salt pulses for the total porosity and non-binding protein pulses for particle porosity ε_p of the protein. For AEX Dextran tracer experiments were used fit a velocity dependent axial dispersion:

$$D_{AX}(u) = D_{AX,0} + D_{AX,1}u + D_{AX,2}u^2 \tag{90}$$

To approximate the effective mass transfer coefficient k_{eff} Eq. (91) was applied [27].

$$\frac{1}{k_{eff}} = \frac{d_p}{10\varepsilon_p D} + \frac{1}{k_{film}} = \frac{1}{k_{pore}} + \frac{1}{k_{film}} \tag{91}$$

The correlation used to calculate the film transfer coefficient

$$k_{\text{film}} = \frac{1.09}{\varepsilon_{\text{b}}} \frac{D_m}{d_{\text{P}}} \left(\frac{\varepsilon_{\text{int}} u_{\text{int}} d_{\text{p}}}{D_{\text{m}}} \right)^{0.33} \tag{92}$$

is based on the Wilson and Geankoplis correlations. The intraparticle (pore) diffusion coefficient D [cm^2s^{-1}] and the molecular diffusion coefficient D_{m} [cm^2s^{-1}] were determined based on the Mackie-Meares correlation [82,83]. In contrast, for CEX the dispersion coefficient $D_{\text{AX}}(u)$ in Eq.(90) was estimated based on non-binding protein pulse experiments at various flowrates. The effective mass transfer coefficient k_{eff} was set to not limiting $\frac{r_{\text{p}}}{3}$. The ligand density was determined by acid-base titration according to Huuk et al. 2016. [84]

Fitting parameters of the CPA model for each protein are the protein charge $Z_i(\text{pH})$ as a function of pH in Eq. (93), the boundary thickness layer Δ_i, the lateral charge $Z_{\text{lat},i}$ and the kinetic parameter. The reference pH pH_{ref} represents the pH of the buffer solution. The accessible surface area A_{S} was set equal for all species.

$$Z_i(\text{pH}) = Z_i(\text{pH}_{\text{ref}}) + \sum_{k=1}^{m} Z_{k,i}(\text{pH} - \text{pH}_{\text{ref}})^k \tag{93}$$

3.4 Results and Discussion

An integrated mechanistic model of a two-column polishing sequence including pH adjustment steps was built, calibrated, validated, and applied. The focus was on the interconnection of the process steps and predictivity across scales.

3.4.1 Model calibration – laboratory scale

The model for adjustment has no fitting parameter and is therefore not calibrated on experimental data.

3.4.1.1 Parameter estimation – general

All system parameters of the chromatography columns were kept constant across all experiments, conditions, and scales. The resulting column parameters obtained by tracer experiments, acid base titration, and inverse size exclusion chromatography (iSEC) are listed in Table 7. The total available adsorber surface $A_{\text{S},0}$ of AEX and CEX was adopted by iSEC evaluation published by Briskot et al. [42]. The parameters are in alignment with previous

published data and the differences in resin types reveal known distinctions between agarose (Q-Sepharose FF) and polystyrene divinylbenzene (Poros 50 HS) beads [42]. Poros resin is known to be a perfusion resin with bimodal pore sizes [85]. This is caused by its agglomerated microspheres which form the resin particles. The intraparticle macropores allow convective flow and axial dispersion, which is the predominant effect to peak broadening in perfusion chromatography [86]. To avoid biases in protein parameters by these effects, the non-binding protein pulses were used to determine a flow dependent D_{ax} function. Moreover, a constant protein particle porosity was introduced to match protein pulses under non-binding conditions. Non-binding protein pulses as reliable data source for column parameters was presented for a Fractogel CEX resin by Heymann et al. [87]. Furthermore, the film diffusion was assumed to be not limiting for the Poros 50 HS resin [88]. The model assumptions were validated by simulating the non-binding protein pulses at different flow rates (data not shown).

Table 8: Summary of column parameters. Except for volume and concentration, all parameters were transferred for the manufacturing scale runs.

Parameter	Q-Sepharose FF (AEX)	Poros 50 HS (CEX)
V_C [mL]	12.10	10.00
L_C [cm]	15.40	10.00
Void fraction ε_{int} [-]	0.338	0.402
Total column porosity ε_t [-]	0.854	0.725
Bead radius r_P [µm]	45	25
Protein particle porosity ε_P [-]	0.854	0.411
$D_{ax,0}$ [mm^2s^{-1}]	-0.136	0
$D_{ax,1}$ [mm]	0.252	0.195
$D_{ax,2}$ [s]	0	0.445
Ionic capacity Λ_{IEX} [M]	1.50	0.31
$A_{S,0}$ [m^2m^{-3}]	4.80e8	1.40e8
A_S [m^2]	3.60e8	6.25e7
Ligand density $\Gamma_L = \Lambda_{IEX} A_{S,0}^{-1}$ [$molm^{-2}$]	3.12e-6	2.19e-6

Protein specific isotherm parameters summarized in Table 4 were estimated by fitting the model to the calibration data set (Table 6). The calibration set

and procedure was aligned with straight forward calibration procedure published by Saleh et al. [81]. In this study, size variants (1-5) were included in the model based on HP-SEC results. First, all parameters of the highest concentrated size variant 1 were estimated, including the accessible surface AS to reduce the estimation problem complexity. [88]. The parameter estimates of Z_i, Δ_i, $k^*_{kin,i}$ and $Z_{lat,i}$ were able to describe the entire calibration set by a single protein species. The pH dependency of Z_i was estimated based on LGE experiments at 4 equidistant points between pH 4.6 and pH 5.2.

To link the model to relevant analytic size exclusion chromatography offline data, the size variants (1-5) were introduced to the model. To avoid high parameter uncertainty, parameters of size variances were estimated in subsets as suggested by Hoffmann et al. [89,90]. Additional LGE experiments with purified size variants 4 and 5 were used to estimate Z_i and Δ_i including pH dependency parameters $Z_{1,i}(pH_{ref})$ and $Z_{2,i}(pH_{ref})$. Parameters of low abundant species were initially set constant to parameter values of size variant 1, which were considered reasonable initial estimates. If Z_i and Δ_i estimation of a variant could not yield a good fit, $k^*_{kin,i}$ and $Z_{lat,i}$ were set free for estimation. A free kinetic parameter could not achieve improvement and was therefore mostly adopted from size variant 1.

Table 9: Summary of all CPA model parameters of protein species on CEX. Parameters that were transferred from size variant 1 estimates and size variant of the same radius are presented by merged cells.

Parameter	Size variant 1	Size variant 2	Size variant 3a	Size variant 3b	Size variant 4	Size variant 5
a [m]	2.4e-9		1.8e-9			3.4e-9
Δ_i [-]	5.3e-3	4.3e-3	7.2e-3	5.2e-3	5.5e-3	7.8e-4
$k^*_{kin,i}$ [s^{-1}]	41.0					32.0
$Z_i(pH_{ref})$ [-]	17.5	17.5	10.9	12.9	13.4	32.9
$Z_{1,i}(pH_{ref})$ [-]	-7.9				-7.6	-13.6
$Z_{2,i}(pH_{ref})$ [-]	3.5				8.8	-5.3
$Z_{lat,i}$ [-]	6.0					17.1

The calibration set of AEX revealed no significant adsorber interaction for the size variants. However, interactions might occur in different pH regions which were not relevant for this study. Thus, the isotherm parameters could be set to

zero without loss of model quality, which reduces the influence of uncertain parameter values.

3.4.1.2 Parameter estimation – CEX specific

To limit the possible parameter combinations, a combination of gradient and step elution with low and high loading conditions was chosen. The resulting simulations and measured data are shown in Figure 12. Simulations and measured data agree well for the strongly different conditions, increasing the chance of a predictable parameter set.

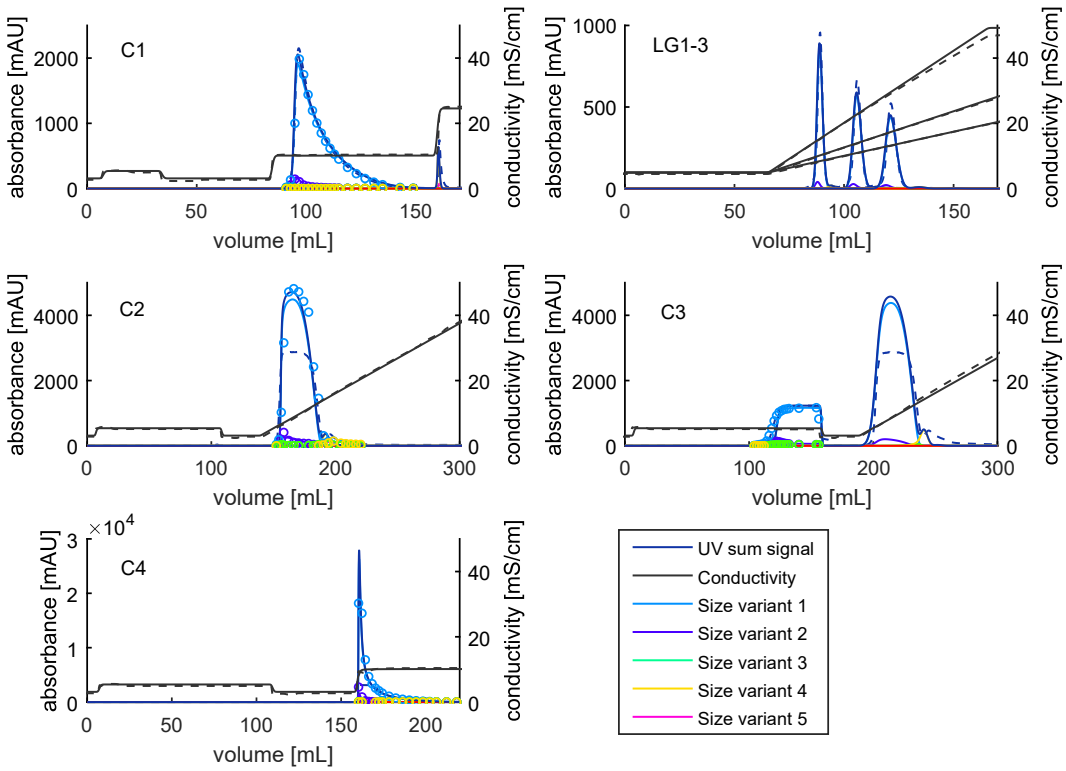

Figure 12: Model calibration set for CEX. Dashed line represents the UV280 nm measurement data and solid lines the simulation. Fraction data is depicted by points. Experiment order starting from top left to bottom right: CEX_C1, CEX_LG1-3, CEX_C2, CEX_C3, CEX_C4.

The presented model to measurement data alignment was not achievable by a steric mass action SMA model (data not shown). The advantages of the CPA model over the SMA model were discussed by Briskot and could be confirmed in this case [42,44]. The zoomed version of Figure 12 is presented in Figure 13. A good agreement of model and data alignment for low abundant size variants could be observed. However, some deviations were present for example in the BTC experiment. Since no parameter combination could be identified to describe this trend, the deviation can be stated as model limitations or caused

by measurement errors. In this study, it was assumed that all proteins reach the same accessible surface area. For different size variants this assumption might not hold. However, exact predictions of breakthrough curves are not critical for future applications of the model due to the strict control of the maximal loading density.

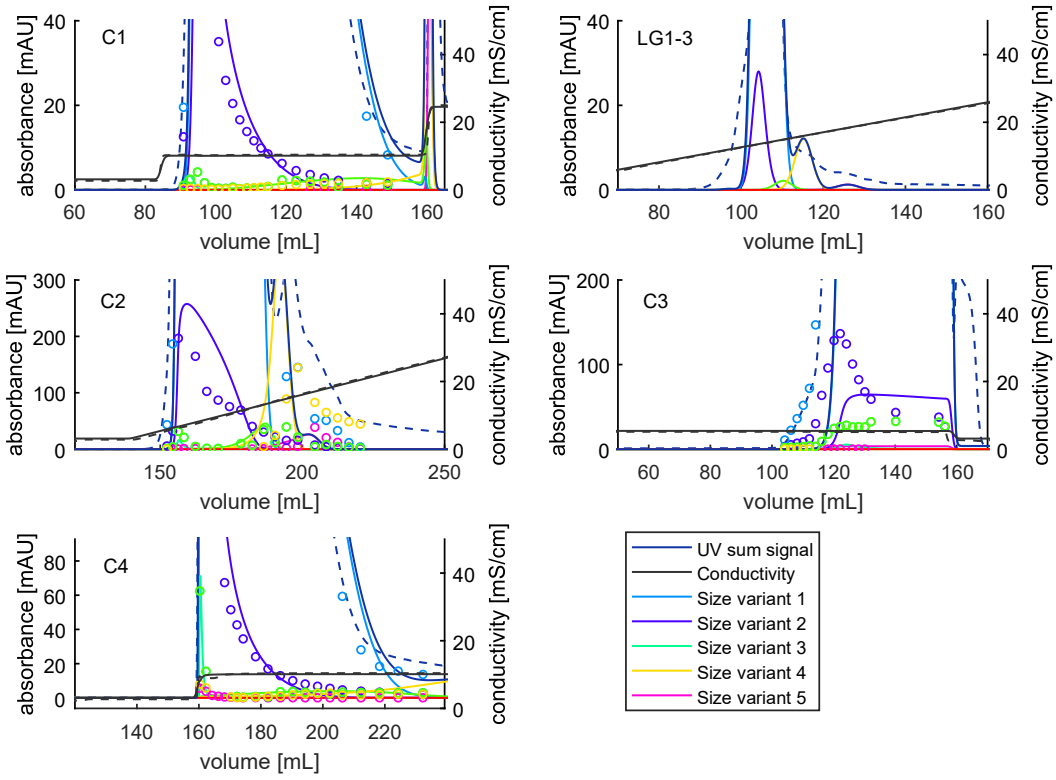

Figure 13: Zoom into the model calibration set for CEX shows the model fit to measurement data. Experiment order starting from top left to bottom right: CEX_C1, CEX_LG1-3, CEX_C2, CEX_C3, CEX_4.

The following explains the assumptions that were required to fit the analytic data to the elution chromatogram without violating mass balance. Size variant 4 was found to be significantly higher in the load than in the elution peak of high load gradient elution experiment CEX_C2. This observation was verified with LGE experiments of purified size variant 4 by preparative SEC (not shown). Based on mass balance the loaded size variant 4 was assumed to mainly elute during NaOH regeneration step. This might be explained by hydrophobic interaction with the hydrophobic backbone of CEX, as pointed out by Huang et al [91]. By mass balancing the ratio of ~20 % size variant 4 was found to elute during salt gradient and thus was considered in the model. The other strongly bound part of size variant 4 was considered to bind to the column with a Δ_i of $10e^3$ to simulate the strong binding behavior. Furthermore, no parameter set was found to achieve a fit with a single size variant 3, which

indicates that the size variant 3 possibly consists of an early and late eluting variant which could be caused by charge variants [73,81,88]. Hence, the size variant 3 was split in an early (~10 %) and late eluting component based on CEX_C2 mass balance to match offline measurement data. All assumptions made were adopted to manufacturing process runs. The assumptions demonstrate the challenge to stay consistent in mass balance and SEC analytic variants.

3.4.2 Model validation experiments

Model validation is performed under conditions for which the model has not been calibrated. This is intended to emphasize the validity of the model selection and calibration procedure. The estimates of the parameters of a validated model should therefore have physical meaning that allows extrapolation.

3.4.2.1 Adjustment model

Since the pH adjustment model has no parameters that need to be determined experimentally, it was directly applied to predict titration curves of adjustment steps based on protein concentration amino acid composition and ion concentration. As shown in Figure 14, the model was able to predict titration curves and the amount of titrant required to reach a certain pH. Minor deviations could be explained by measurement errors or the neglect of the impact of small temperature variations between or within experiments on buffer pK values. Aggregation kinetics were negligible since no measurable changes of size variant concentrations could be observed during pH adjustment experiments.

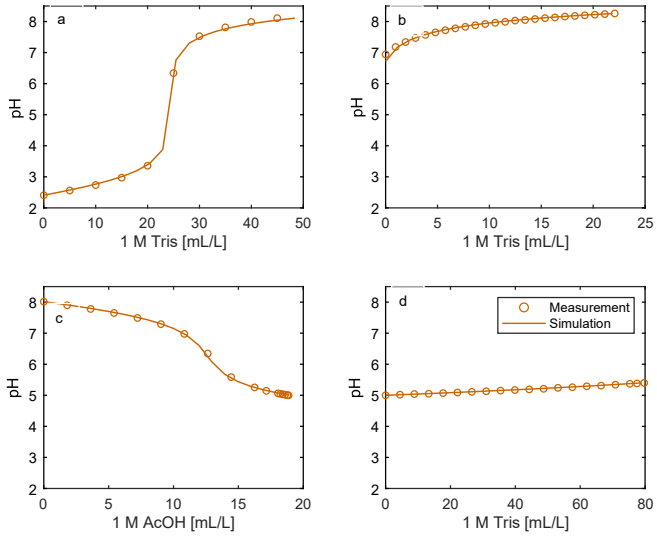

Figure 14: Validation of the pH adjustment model: (a) shows the neutralization step of the low pH virus inactivation (Adj.B_V), (b) is the adjustment (Adj.1_V) with 1 M Tris prior to AEX, (c) is the adjustment (Adj.2_V) prior to the CEX loading and (d) is the adjustment step (Adj.3_V) prior to virus filtration. (AcOH represents acetic acid)

3.4.2.2 Chromatography model - AEX

Figure 15 shows simulation, offline and online data of the AEX flow through experiments presented in Table 5. The experiment set was designed to reveal possible interactions of size variants within the relevant pH, ionic strength, and loading. However, the data set did not show any relevant interactions for the size variants with the AEX resin, resulting in a pure flow-through model. At the beginning of the subsequent salt gradient, elution proteins composed mainly of host cell proteins (HCP) were observed and could not be evaluated with SEC. This information could be helpful to extend the model by HCPs as demonstrated in other studies [74,92].

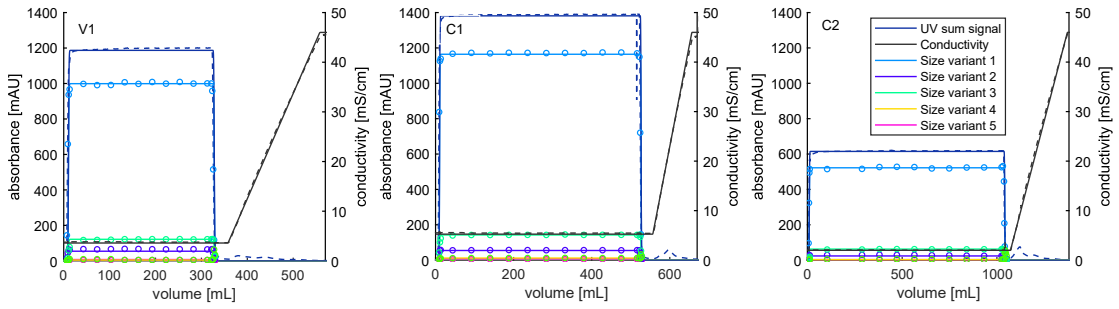

Figure 15: Calibration and validation experiments: The flow through mode showed no interaction with the resin for the investigated protein species and conditions. From left to right: AEX_V1, AEX_C1, AEX_C2.

3.4.2.3 Chromatography model – CEX

The calibration set of the CEX model covered a broad range of conditions. However, the pH dependency was only calibrated based on low load LGE. Therefore, the validation in Figure 16 included high load experiments at the outer edges of the pH calibration range. The prediction shows a good alignment of measurement data and simulation with only minor deviations. Peak width and shape prediction especially at low pH was well met. It is worth mentioning, that the size variant 4 is deviating from the main peak indicating an improved depletion at low pH. Discrepancies of the sum signal of simulation and measurement signal are caused by neglecting various underlying species not correlated with SEC offline analytics. The validation results underline the validity of the calibrated model to produce trustworthy results at least within the calibrated and validated range.

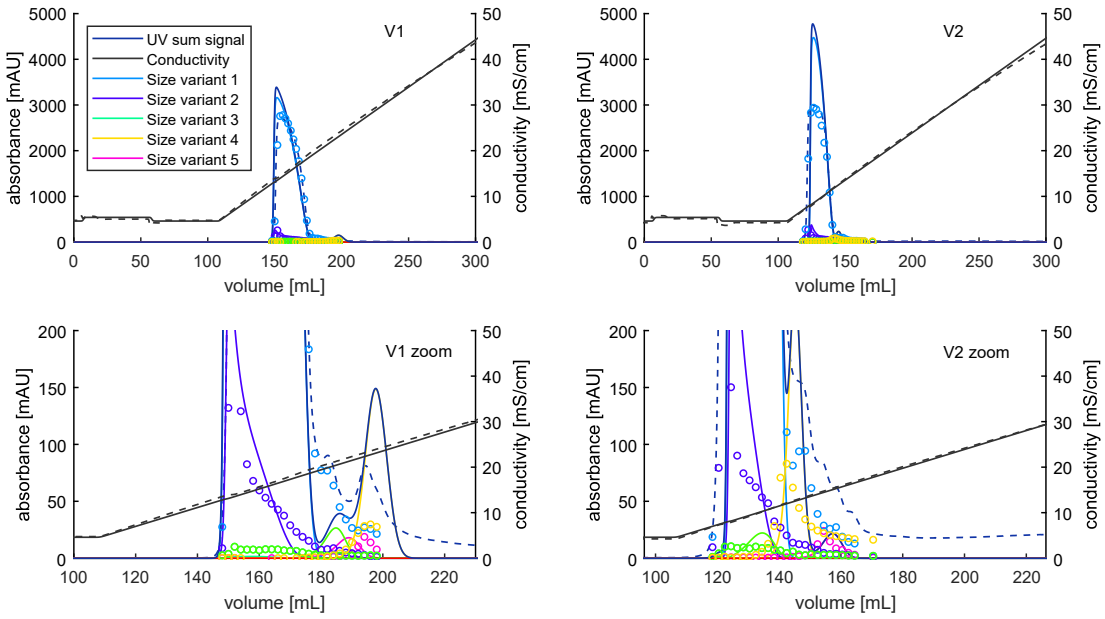

Figure 16: Validation set of the CEX model: In the upper left is pH 4.6 and in the upper right is pH 5.2. The two lower plots are the zoom view and belong to the plots above.

3.4.2.4 Model application – manufacturing scale

The laboratory scale calibrated, and validated individual models were combined to an integrated model and applied to extrapolate the manufacturing run shown in Figure 17. The integrated model consists of 4 individual models and the output of one step was the input of the next. Parameters passed through were the protein concentration, ionic strength, ion composition and the pH. In the following, the results are discussed in process order. The pH adjustment model predicted the titrant amount of pH adjustment 1 (Adj.1) with minor deviation. The bubble trap prior to the AEX column was approximated

by an 8 cm stirred tank reactor to account for additional dispersion. The model prediction of the manufacturing elution chromatogram was in very good agreement with the measurement data. Minor deviation of the conductivity signal can be caused by molar conductivity causing a nonlinear relation with ionic strength, which was assumed in this study [93]. The protein ion mixture consists of varying concentration between glycine, sodium chloride, acetate, and Tris along the process. The second adjustment step (Adj.2) underpredicted the AcOH titrant required to reach the target pH by ~ 3 mL/L. This trend was also observed in the validation data set; however, the deviation was less pronounced. The underprediction of titrants can have various causes like measurement uncertainty, choice of pk_k or the temperature sensitivity of Tris and requires further investigation. The subsequent CEX step showed very good agreement with the elution profile in the manufacturing scale. Compared to the calibration column the bed height was more than doubled with no significant deviations in peak shape underlining the extrapolation capability of the mechanistic model. In summary, the scaling of the integrated mechanistic process model describing the basic electrostatic interactions of the proteins with the adsorber surface and solutes provides a satisfactory prediction of the manufacturing data across the steps.

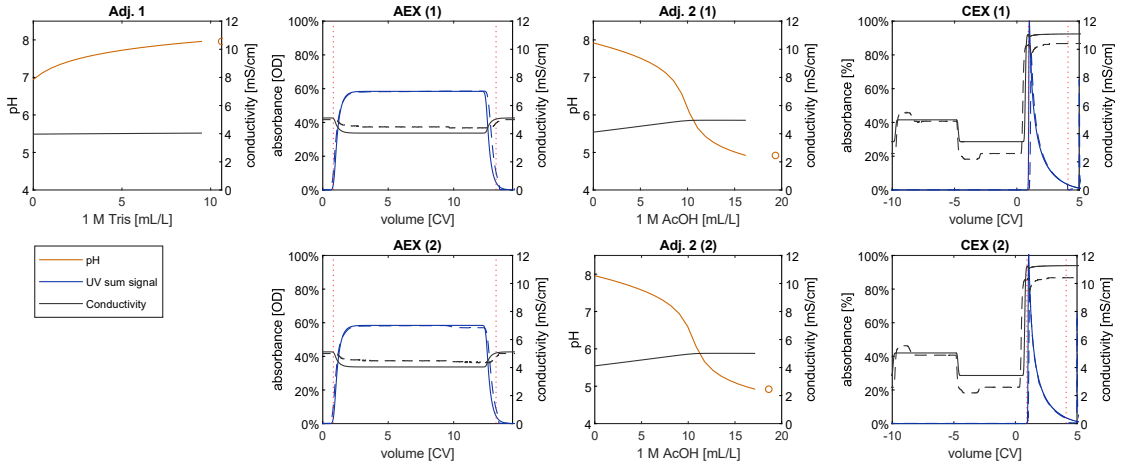

Figure 17: Manufacturing sequence prediction: Starting with a pooled adjustment step (Adj.1), the resulting adjusted pool is split into two polishing trains (1) and (2). The output of one unit is the input of the next unit operation. Dashed lines represent the measurement data and solid lines the simulation. Cutting lines are shown in dashed red vertical lines. Points at the end of the adjustment steps are the measured amount of titrant required to reach the target pH.

The integrated model was applied to 94 historical manufacturing runs to investigate the model's ability to describe process variations based on real input variations at set-point conditions. The input variation included varying protein concentrations, volumes, size variant composition, ion compositions,

and pH values. Measured process parameters and analytic results are compared to the model predictions. The results in the sequenced boxplots in Figure 18 show that the model was capable of predicting the median of the process across units as well as the process variation. The high variance in the volume was due to the division in one or two polishing sequences trains and was well reproduced by the model. Also, the prediction of the concentration and its variation fits well to the measured data. The yield trend, however, showed small systematic deviations, which may due to measurement inaccuracy. However, the variation of the yield was also be reproduced well. The pH model was able to reproduce the process dispersion of the titration volume, even if there were small systematic deviations. The ion input to the process was higher for Adjustment 2 (Adj.2), but still within a moderate spread. Regarding the size variant analytics, the size variants 1-5 are well predicted in their depletion under process variance by the model. Size variant 3 + 4 and size variant 5 were depleted efficiently while size variant 1 was enriched. Hence, the model correctly predicted which variant was enriched or depleted. Small systematic deviations could also be caused by measurement inaccuracies but also by the assumptions made as discussed earlier. It is worth noticing, that for some unit inputs/outputs a normal distribution assumption may not apply.

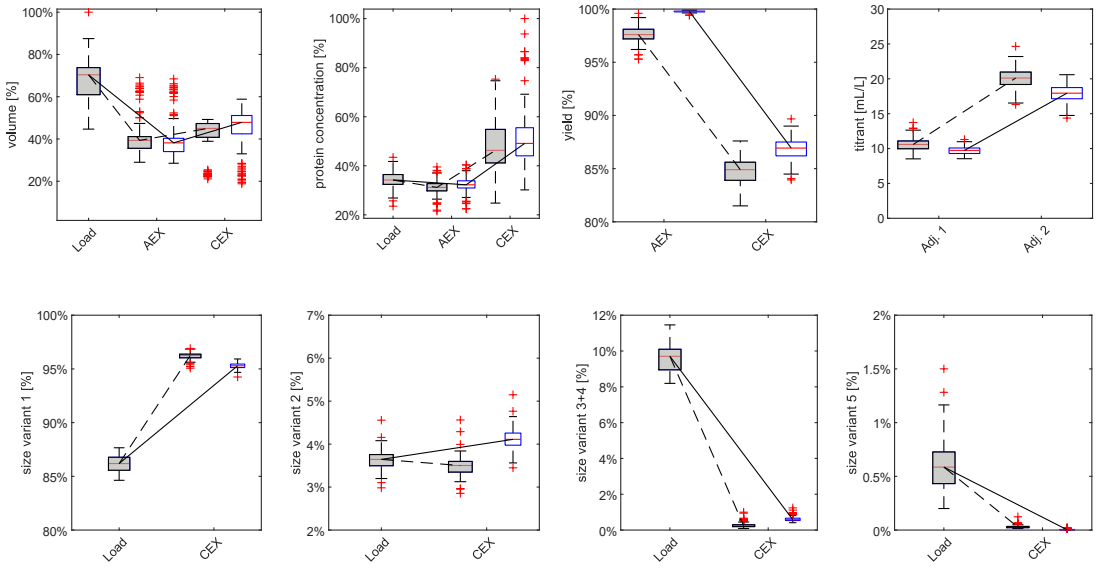

Figure 18: Comparison of model predictions and measured data of historical production data set: The process variance was given as input to the integrated process model and the comparison of the model prediction to the production data was visualized. Process variables as well as quality attributes are considered. Gray boxplots represent measured data variation and white filled boxplots represent the simulation prediction for the input variation. The lines connecting the medians are only for visual representation, where the dashed line was used for the measured data and the solid line leads to the simulation data. Volume and concentration were normalized to the maximum value.

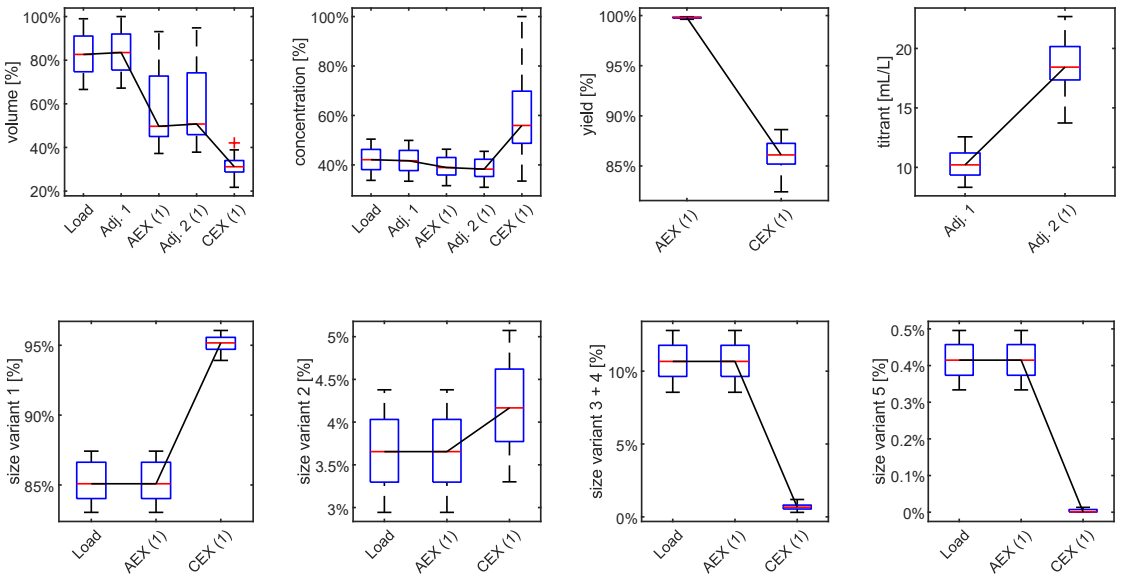

Figure 19: Latin hypercube sampling of loading conditions: Latin hypercube sampling (LHS) was performed by varying the loading conditions of the integrated process model between +- 20% and plotting the process variation across process units. The process parameters elution pH and ionic strength of CEX were additionally varied within the observed production normal distribution. The sequence was reduced to the first train (1), and redundant boxplots were masked out for clarity. Volume and concentration were normalized to the maximum value.

In general, the calibrated model at laboratory scale confirmed the ability of the process to retain depletion capability and high yields under varying loading conditions and usual input process perturbation as demonstrated in Figure 18. This allows the process to be investigated *in silico* for optimization potential and reveal potential robustness issues. The demonstrated ability of the model to predict process performance and variation at the set-point is only one possibility in the application of process development and process control. A question that can be difficult to address experimentally is whether the process chain is capable of maintaining process performance at higher process variation. Such issues could be investigated by deflecting process parameters further than it would be expected based on historical data. Figure 19 shows the results of a LHS with a 20% deflection and 100 sample points of all input data of unit IV. Here, it can be directly investigated where the highest process variance can be expected as a function of input variance. It becomes clear that a variance in the volume is reduced by the CEX step, but results in a high variance in concentration. This in turn exhibits a skewed distribution towards low concentration. The step yield, however, shows a robust variance range for Poros of around 5%. By examining the volumes of the titrants, the input of AcOH by Adjustment 2 (Adj.2) is almost twice as high compared to Tris by

Adjustment 1 (Adj.1). The robust abundance of the size variants considered indicates that the ion input and its variation had no significant influence on the process performance. The presented model and data allow to quantitatively evaluate propagation of process variance in manufacturing scale. Based on these results, statistical methods like the partial rank correlation coefficient might be used to further investigate the interrelationships and influencing factors to further increase the process understanding across process units [60].

3.5 Conclusion

The downstream process is a series of chromatography, filtration, and adjustment steps that interact with the immediately adjacent units. Therefore, the impact of process parameters and feed material composition on the product quality must be understood across the entire process chain. By means of a purely experimental approach, however, this is a very material-intensive, if not impossible challenge. This study demonstrated that the state-of-the-art mechanistic models could describe a concatenation of ion-exchange chromatography as well as adjustment steps. Furthermore, the scale-independence of the models allowed direct extrapolation from bench scale to the production scale and thus conclusions on process capability and facility fit. This was demonstrated on 94 historical manufacturing data sets.

The calibration set presented for CEX was sophisticated in design, providing confidence in the CPA model predictions. The approximated pH dependency derived by only LGE experiments could be successfully validated to higher loading gradients. However, to match analytical measurement data from low abundance variants, assumptions were required that underscore the complexity of describing analytical variants within a CEX elution profile. For scale-up, a bubble trap was added to describe production scale elution behavior. Surrounding adjustment steps to the chromatography steps could be predicted including titrant volumes and titration curves. The polishing steps in particular are crucial for product quality and thus have a significant share in the industrial development timeline. The presented model provides a basis on which quantitative risk analyses regarding process variance and criticality of parameters can be performed at an early stage of development. Variation propagation of volume, concentrations, pH, ionic strength can be analyzed for their criticality across process units without the need for manufacturing data. A control strategy across process units might also lower the criticality of specific process unit parameters thereby reducing development and process control effort.

We demonstrated that the presented electrostatic-based polishing model allows to investigate the performance of the concatenated manufacturing process including adjustment steps at the very early stage of development *in silico*, which can be an accelerator for development. The size variants included in this study are only one of various analytics to consider. Analytic measures like charge variants, HCP, DNA, and virus removal might be added to cover even more CQAs. Modeling of the underlying mechanisms contributes to the fundamental process understanding including interactions between process units.

4 Modeling of biopharmaceutical UF/DF from laboratory to manufacturing scale

Federico Rischawy[a,b], Till Briskot[a], Frederik Nitsch[a,b], David Saleh[a], Gang Wang[a], Simon Kluters[a], Joey Studts[a], Jürgen Hubbuch[b]

[a] DSP Development, Boehringer Ingelheim Pharma GmbH & Co. KG, Biberach, Germany

[b] Karlsruhe Institute of Technology (KIT), Institute of Engineering in Life Sciences, Section IV: Biomolecular Separation Engineering, Karlsruhe, Germany

Corresponding author: Jürgen Hubbuch, Tel.: +49 721 608 47526, juergen.hubbuch@kit.edu

Abstract

The development of ultrafiltration and diafiltration (UF/DF) processes in the biopharmaceutical industry is largely empirical and rarely mechanistic. As a result, the full potential of process understanding is not unleashed. In this study, a model for a biopharmaceutical UF/DF process is introduced and applied for a Fab fragment from lab to manufacturing scale using a Ultracel Pellicon® 3 C-Screen cassette. For model calibration viscosity data, membrane permeability and a single ultrafiltration experiment were used. The calibrated model responded correctly to extrapolating process conditions regarding the control parameters crossflow and transmembrane pressure (TMP). This was demonstrated by a multivariate dataset of ultrafiltration experiments ranging from a protein concentration of 5 g/L to 200 g/L. The validated model was used to predict the entire UF/DF process at lab and manufacturing scale.

4.1 Introduction

Ultrafiltration and diafiltration (UF/DF) is used in biopharmaceutical downstream processes for concentration and buffer exchange, typically as the final purification step facilitating the formulation of the drug substance. Current process development is mostly based on an empirical approach using generic platform conditions and membranes. However, challenges like demand for high concentrated liquid formulation (HCLF) [94], manufacturing capacity limitations, and new antibody formats [22] can result in development challenges and a lack of fit to platform conditions. Challenges that need to be addressed are, among others, the Donnan effect [58], aggregation [95], optimization, and control [30]. Especially for UF/DF experiments, the material consumption per experiment is typically high and therefore only possible in limited numbers. Mechanistic models offer an efficient way to extract information from individual experiments. Subsequently, the models can provide guidance for action due to their extrapolation capabilities. The extrapolation is possible because the model equations describe underlying mechanisms that establish a causal relationship between input and output parameters [68]. The objective of this study is to describe the pressure-flow relationships for an entire UF/DF process.

The permeate flow declines with increasing protein concentration during tangential flow filtration (TFF). This decline can be usually described by a concentration polarization on the membranes surface [53,96]. Mechanistic models describing the concentration polarization phenomena can be subdivided in resistance models, gel-polarization models and osmotic pressure models [50]. The theories can also be combined to determine unknown model parameters, such as the combination of the stagnant film model and the osmotic pressure model. The stagnant film model is a resistance model that describes the permeability of the concentration polarization layer at the membranes surface [53]. For this model it is assumed that the permeate flow is limited by the osmotic pressure of the concentrated protein at the membrane wall. This wall concentration is required for the stagnant film model and can be evaluated by the osmotic pressure model [52]. Consequently, the osmotic pressure model introduces a transmembrane pressure (TMP) and osmotic pressure dependency to the model. However, the stagnant film model is limited because it assumes a constant mass transfer coefficient and depends only on the bulk protein concentration and the wall concentration. Binabaji et al. introduced the modified polarization model, where the gradient in solute concentration is replaced by the gradient in chemical potential [52,54]. With this change, the concentration polarization model depends on the change of protein osmotic pressure and viscosity during ultrafiltration. In addition, the crossflow scaling

of the mass transfer was demonstrated to describe the crossflow dependency of the permeate flow. Limitations of the model at low protein concentrations and the discussion about the wall concentration estimation was later addressed by Baek et al. [97,98]. The applied resistance in series model provides a smooth transition between the osmotic pressure model and the modified concentration polarization model. Furthermore, Baek found that the wall concentration was insensitive above a certain concentration value and therefore set the parameter constant. Hence, the model presented by Baek et al. should be in theory responsive to most relevant process parameters including crossflow, TMP, concentration, pressure drop in the module, viscosity, and osmotic pressure. For this, additional measurements of osmotic pressure and viscosity, especially at high protein concentration, are required. However, the osmotic pressure measurements are time consuming which is a disadvantage for an application in time-critical industrial process development. Although the model was shown to describe the filtrate flux at protein concentrations from 8-100 g/L at varying TMPs, a combination of TMP and crossflow was not investigated over a broad range of protein concentration. In addition, the pressure combined with flow rate progression were not demonstrated simultaneously during ultrafiltration.

In this study, a model describing the online data of varying TMP, and crossflows is introduced. Therefore, the permeate flow model presented by Baek et al. was extended and applied from the point of view of applicability in process development and transfer. A resistance in series model was calibrated and validated in lab scale and the TFF system specific control of the permeate and retentate pressure were addressed and incorporated into the model. In contrast to previous studies, the pressure drop was described with an effective crossflow. The effective crossflow considers membrane-specific influences of the permeate flow on the pressure drop, which are neglected in a simple crossflow consideration. Viscosity data were measured under low and high salt conditions which is required for the filtration and pressure model. Ultrafiltration online data was used to determine remaining model parameters. The diafiltration phase was approximated by combining the initial ultrafiltration (UF1) and the final ultrafiltration (UF2) models based on the buffer mixture percentage of a non-retained salt. The final model was applied to extrapolate to manufacturing scale of different process conditions.

4.2 Theory

In this section, the equations describing the laboratory-scale UF/DF experiments are presented. A schematic overview of a UF/DF system is presented in Figure 21. The first step of a UF/DF filtration process is

ultrafiltration 1 (UF1). The protein solution with relatively high volume and low protein concentration is concentrated at constant tank volume. This is achieved by adding the protein solution to the tank at the permeate flow rate. The second step is diafiltration (DF), in which a buffer solution is added in the permeate flow instead of the protein solution, thus achieving buffer exchange. In the final ultrafiltration (UF2) phase, the buffer-exchanged protein solution is concentrated by reducing the volume at the rate of the permeate flow. In the following section. First, general mass balances are defined to describe the change in concentration and volume of the filter system over time. Then, the permeate flux is described by a general concentration polarization model. The model is completed by a model to describe the membrane pressure drop, which is presented in the last subsection.

4.2.1 Mass balance

To provide a tank model that can describe experimental online data, a time dependent description of the UF/DF process is required. This was achieved by an ordinary differential equation (ODE) system derived by material balance with boundaries around the reservoir and membrane compartment as shown in Figure 21. The reservoir of the UF/DF system was considered a perfectly mixed stirred tank reactor of varying reservoir volume. The UF/DF system volume V [L] includes the reservoir and dead volume. Depending on the filtration phase, the volume inflows were the protein solution inflow F_{in} [Ls^{-1}] or the buffer flow during DF F_{buffer} [Ls^{-1}]. With the single outflow of the permeate flow F_{permeate} [Ls^{-1}], the volume equation is given by Eq. (94).

$$\frac{dV(t)}{dt} = F_{\mathrm{in}} + F_{\mathrm{buffer}} - F_{\mathrm{permeate}} \tag{94}$$

The mass balance for the protein in the bulk solution c_{p} [gL^{-1}] within the system boundaries results in Eq. (95):

$$\frac{dc_{\mathrm{p}}(t)}{dt} = \frac{(F_{\mathrm{in}}c_{\mathrm{p,in}} - \frac{dV(t)}{dt}c_{\mathrm{p}}(t))}{V} \tag{95}$$

assuming a fully retentive membrane. For the salt concentration i in the system $c_{\mathrm{s},i}$ [gL^{-1}] the ODE is given by:

$$\frac{dc_{\mathrm{s},i}(t)}{dt} = \frac{(F_{\mathrm{in}}c_{\mathrm{s},i,\mathrm{in}} + F_{\mathrm{buffer}}c_{\mathrm{s},i,\mathrm{buffer}} - F_{\mathrm{permeate}}c_{\mathrm{s},i,\mathrm{permeate}} - \frac{dV(t)}{dt}c_{\mathrm{s},i}(t))}{V} \tag{96}$$

In this study, the Donnan effect was neglected and thus the permeate concentration of salt $c_{s,i,\mathrm{permeate}}$ was considered to be equal to the concentration in the bulk solution. The diafiltration buffer concentration of salt ions i is given by $c_{s,i,\mathrm{buffer}}$. The presented equation system was solved over time for every UF/DF phase (UF1, DF, UF2) until a specific phase target, e.g., the DF volume or target concentration, was reached. Between different phases the feed flow and other process parameters are variable. For example, during DF the F_{buffer} is set equal to F_{in} and during UF F_{in} is set to zero once the load volume is empty or the target concentration is reached.

4.2.2 Permeate flow model

The permeate flow required for Eqs. (94) - (96) depends on various process parameters which include protein characteristics, concentration, membrane characteristics, pressure and flow conditions. For the sake of simplicity, F_{permeate} was considered to be approximately at steady state. The permeate flow is given by:

$$F_{\mathrm{permeate}} = \bar{J}_{\mathrm{v}} M_{\mathrm{n}} A_{\mathrm{m}} 10^{-3} = 10^{-3} M_{\mathrm{n}} \frac{A_{\mathrm{m}}}{\mathrm{L}} \int_0^L J_{\mathrm{v}}(x)\,dx \tag{97}$$

where the length average permeate flux $\bar{J}_{\mathrm{v}}$ [ms^{-1}] is the integral of the local permeate flux J_{v} [ms^{-1}] along the membrane length L [m] with $x \in [0, L]$. The number of membranes is represented by M_{n} [-] and the membrane filtration area by A_{m} [m^2]. In this study, the resistance-in-series expression first derived by Yeh et al. [99]:

$$\frac{1}{J_{\mathrm{v}}(x)} = \frac{1}{J_{\mathrm{lim}}} + \frac{R^*}{J_{\mathrm{membr}}(x)} \tag{98}$$

was used to describe the local permeate flux J_{v} [ms^{-1}]. The local permeate flux depends on the resistance share of the concentration polarization (first term) and the membrane resistance share (second term). In contrast to Baek et al. [97] the additional R^* [-] accounts for possible resistances due to other fouling phenomena such as adsorption and provides an additional degree of freedom. The limiting local permeate flux J_{lim} [ms^{-1}] in Eq. (98) was described by the modified concentration polarization model developed by Binabaji et al. [52]:

$$J_{\mathrm{lim}} = k_0 \left(\frac{\eta_{\mathrm{p}}}{\eta_0}\right)^{\frac{1}{3}} \int_{c_{\mathrm{p}}}^{c_{\mathrm{w}}} \left(\frac{M_{\mathrm{p}}}{RT}\right)\left(\frac{\eta_0}{\eta}\right)\left(\frac{d\Pi}{dc}\right)\frac{dc}{c} \tag{99}$$

where the integral was solved for the protein concentration from the bulk concentration to the concentration at the membranes surface wall c_{w} [gL^{-1}]. The protein molecular weight is represented by M_{p} [kgmol^{-1}], the mass transfer

coefficient by k_0 [ms^{-1}], the ideal gas constant by R [Jmol^{-1}K^{-1}], the osmotic pressure of the protein solution by Π [Pa] and the absolute temperature by T [K]. Although it has been shown that the mass transfer coefficient k_0 [ms^{-1}] depends on known membrane quantities [100,101] the parameter was estimated from experimental data due to its high sensitivity. By scaling the k_0 coefficient by $u^{0.5}$ according to Binabaji et al. [52] a crossflow dependency of the permeate flow is achieved. The viscosity of the protein free buffer solution in Eq. (99) is represented by η_0 [Pas] and the viscosity of the protein bulk solution by η_p [Pas]. Back filtration could be neglected and thus was not included in this study. Eq. (99) has been used in previous works to study the permeate behavior at high protein concentration [52,55,102,103]. However, the model has shown to overpredict the permeate flow at low protein concentration due to the neglected membrane resistance [97]. As pointed out by Baek et al. the effect of the membrane resistance given by Eq. (100):

$$J_\mathrm{membr}(x) = \frac{L_\mathrm{p}}{\eta_0}\left(P(x) - P_\mathrm{permeate} - \Delta\Pi\right) \tag{100}$$

should be considered, where the local feed pressure is represented by $P(x)$ [Pa], the permeate pressure by P_permeate [Pa], and the hydraulic membrane permeability by L_p [m]. Inserting in Eq. (100) a linear pressure drop function $\Delta P(x)$ [Pa]:

$$P(x) = P_\mathrm{feed} - \Delta P(x) \tag{101}$$

as presented in section 4.2.3, results in:

$$J_\mathrm{membr}(x) = \frac{L_\mathrm{p}}{\eta_0}\left(P_\mathrm{feed} - \Delta P(x) - P_\mathrm{permeate} - \Delta\Pi\right) = J_0 - \frac{L_\mathrm{p}}{\eta_0}\Delta P(x) \tag{102}$$

where P_feed [Pa] represents the feed pressure and J_0 [ms^{-1}] represents the flow at the inlet of the membranes feed channel. The integral of the local permeate flux along x is given by:

$$\bar{J_\mathrm{v}} = \frac{1}{\mathrm{L}}\int_0^L J_\mathrm{v}(x)dx = \frac{1}{\mathrm{L}}\int_0^L \frac{J_\mathrm{lim}J_\mathrm{membr}(x)}{J_\mathrm{lim}R^* + J_\mathrm{membr}(x)}dx \tag{103}$$

which can be solved for any upper integral bound $L^* \in (0, L]$ resulting in:

$$\bar{J_\mathrm{v}} = \frac{J_\mathrm{lim}L^*}{L} + \frac{J_{lim}^2 R^*}{\frac{L_p}{\eta_0}\Delta P(L^*)}\log\left(\frac{J_{lim}R^* + J_0 - \frac{L_p}{\eta_0}\Delta P(L^*)}{J_{lim}R^* + J_0}\right) \tag{104}$$

Since $\overline{J_v}$ in Eq. (104) depends on the pressure drop [Eq.(110)], which in turn depends on J_v due to u_{eff}, the equations were solved iteratively. In contrast to Baek et al., Eq. (104) is solved between $0 < L^* \leq L$. This is required to describe the lab scale filtration system due to the pressure control. The equation that possibly reduces the upper integral bound to be lower than L is given by Eq. (116). Furthermore, Eq. (104) contains the parameter R^* and thus an increased degree of freedom.

For Eq. (99) and Eq. (100) the osmotic pressure of the protein solution is required. The osmotic pressure is commonly described with three virial coefficients as presented in Eq. (105). The first virial coefficient B_1 [kgmol^{-1}] describing the ideal case by the van't Hoff equation [50,104] given by M_p^{-1}, the second virial coefficient B_2 [molm^{3}kg^{-2}] and the third virial coefficient B_3 [molm^{6}kg^{-3}] can be estimated experimentally or approximated by potential of mean forces [103,105,106].

$$\Pi = RT(B_1 c_p + B_2 c_p^2 + B_3 c_p^3) \tag{105}$$

The viscosity of the protein bulk solution as required for Eq. (99) and the pressure model presented in section 4.2.3, can be described by the Mooney equation Eq. (106) which was first introduced by Ross and Minton [107]:

$$\frac{\eta}{\eta_0} = \exp\left(\frac{b c_p}{1 - \left(\frac{c_P}{c_{max}}\right)}\right) \tag{106}$$

The protein concentration c_{max} [gL^{-1}] at which the viscosity becomes infinite and b [Lg^{-1}] are fitting parameter to be estimated based on viscosity measurements. Another fitting parameter is b^* which is a reduced b. The parameter leads to an effective viscosity in the pressure model which is further described in section 4.4.4.2.

4.2.3 Pressure model

The pressures in a UF/DF process are essential for the system description and control. Usually, the filtration process is controlled by TMP. The TMP in Eq. (107) is defined by the feed side pressure, the retentate pressure $P_{retentate}$ [Pa] and the permeate pressure.

$$TMP = \frac{(P_{feed} + P_{retentate})}{2} - P_{permeate} \tag{107}$$

If the system is TMP controlled and the pressure drop is known, all the relevant system pressures can be described with:

$$P_{\text{feed}} = \text{TMP} + P_{\text{permeate}} - \frac{\Delta P}{2} \tag{108}$$

and

$$P_{retentate} = P_{\text{feed}} - \Delta P \tag{109}$$

with a constant P_{permeate}. A constant permeate pressure can be assumed due to the permeate pressure control by the filtration system. In order to describe all relevant system pressures, the pressure drop is of interest. The linear modified Hagen-Poiseuille equation used by Binabaji et al. [55] and Baek et al. [97] considers the crossflow u [ms^{-1}] to describe the pressure drop in the membranes feed channel. Kaiser et al. [108] showed for single-pass tangential flow filtration (SPTFF), that a linear relationship of crossflow u [ms^{-1}] and pressure drop is limited and needs to be extended. Therefor Kaiser applied a quadratic Darcy-Forchheimer equation which accounts for additional losses due to inertial effects at high Reynolds numbers and crossflows. The Darcy-Forchheimer equation was solved along the membrane as a function of a local crossflow $u(x)$. In this study, the pressure drop along a single 20 cm membrane was assumed to be reasonable approximated by the linear formulation of the Darcy-Forchheimer given in Eq. (110).

$$\Delta P(x) = \left(\frac{\eta}{k_{\text{p}}} u_{\text{eff}} + \frac{\rho}{k_{\text{l}}} u_{\text{eff}}^2\right) x \tag{110}$$

where ρ [kgm^{-3}] represents the solution density, k_{p} [m²] the Forchheimer permeability coefficient and k_{l} [m] the additional loss coefficient. For high values of k_{l} Eq. (110) becomes the Darcy equation [109]. To account for the influence of u on the pressure drop, which was considered to show membrane specific characteristics, an effective crossflow u_{eff} [ms^{-1}] was introduced:

$$u_{\text{eff}} = \frac{10^{-3}(F_{\text{feed}} - a_{\text{p}} F_{\text{permeate}})}{A_{\text{cs}}} \tag{111}$$

where the constant permeate flow factor a_{p} [-] is dependent on the membrane type. The feed channel cross-sectional area is represented by A_{cs} [m²]. This pressure model was validated by membrane permeability experiments presented in section 4.4.1. The sub-models and the quantities exchanged between them are illustrated at a glance in Figure 20. Due to the interdependence of the permeate and the pressure model, the models have to be solved iteratively.

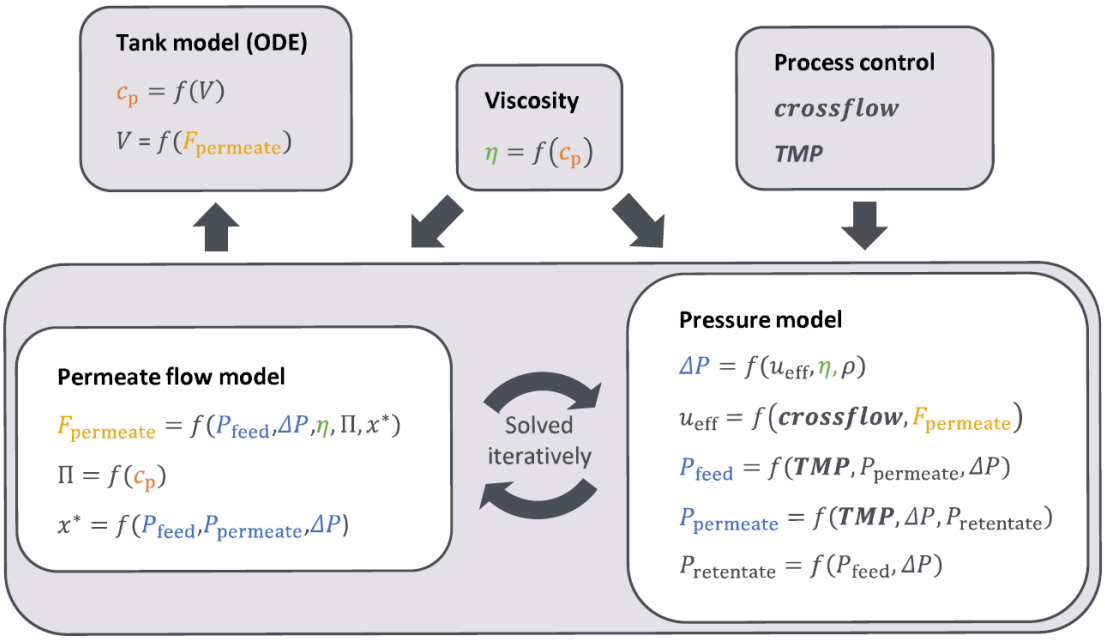

Figure 20: The ultrafiltration model at a glance. The sub-models include the ODE tank model, the permeate model and the pressure model. Since the permeate model and the pressure model depend on each other, the models must be solved iteratively. The viscosity model affects the permeate model and the pressure model. The process controls TMP and crossflow are inputs of the pressure model. The quantities that are exchanged between the models are colored for illustration purposes. Exchanged pressure quantities are shown in blue, permeate flow quantities in yellow, tank model quantities in orange, viscosity model quantities in green, and process controls in bold gray.

4.3 Materials and methods

4.3.1 Protein and buffers

The protein used in this study is a Fab fragment with a molecular weight M_P [gmol^{-1}] of approximately 50 kDa and was produced in-house by Boehringer Ingelheim Pharma GmbH &Co. KG, Biberach an der Riß, Germany. All protein solutions were filtered through a 0.2 µm sterile filter before use. All chemicals in this study were from Merck Millipore (Burlington, USA). The UF/DF load pool condition and first ultrafiltration (UF1) buffer was a 46 mM acetate buffer with a salt concentration of 65 mM NaCl. The buffer was pH adjusted with approximately 38 mM NaOH to pH 5.4. The diafiltration buffer and second ultrafiltration (UF2) buffer was a 25 mM acetate buffer adjusted with approximately 20.9 mM NaOH to pH 5.4. Prior to TFF experiments the protein solutions were diafiltrated to adjust to the mentioned buffer condition and diluted to a concentration of 5 g/L.

4.3.2 System description

The UF/DF system used for lab scale experiments was an ÄKTAcrossflow (Cytiva, Uppsala, Sweden) controlled via Unicorn 7.5. The device provides a control system which is further explained. The crossflow is controlled via the feed pump and the TMP [Eq. (107)] via the retentate control valve and the permeate pump at second instance. In addition, the permeate pump is controlled for a minimal pressure of 0.2 bar to accurately measure the permeate flow. The retentate pressure is controlled if necessary to stay above 0.45 bar. Device flow paths and applied system boundaries are shown in Figure 21.

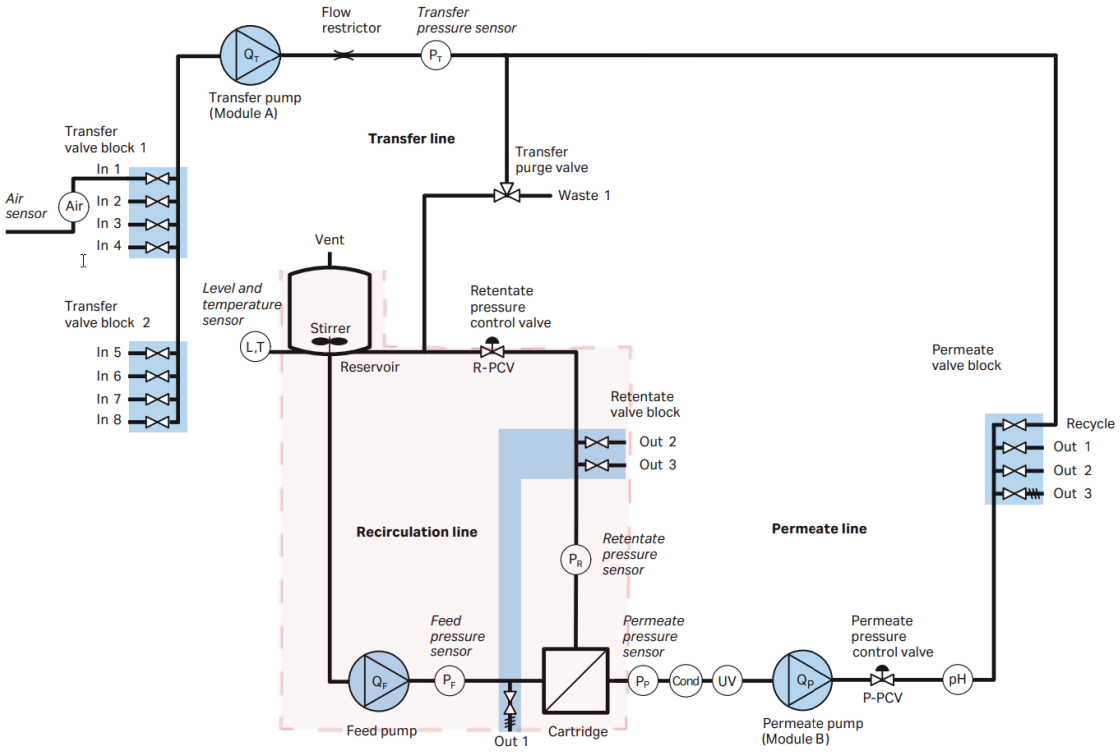

Figure 21: ÄKTAcrossflow [1] (The system flow path) ©2008 Cytiva – Reproduced with permission of owner. The red dashed line surrounds the system boundaries for mass balance.

In small scale, an 88 cm² Ultracel Pellicon® 3 C-Screen cassette from Merck Millipore (Burlington, USA) based on composite regenerated cellulose was used. The dimensions of the membrane sheet were assumed to be of length $L = 20$ cm, width $w = 2.2$ cm, and channel height $w = 0.024$ cm according to Binabaji et al. [55]. At manufacturing scale, a stack of the same type of cassettes with 1.14 m² was used. Dead volumes were determined before experimentation and membrane storage was performed according to the manufacturer recommendation.

The installed UF/DF membrane characteristics were described by the hydraulic permeability and the constant permeate flow factor a_{p} [-] determined by a permeability water experiment. The parameter L_p in Eq. (112) was determined to account for membrane fouling effects prior to each TFF experiment at room temperature (RT) conducted with purified water of viscosity η_{water} [Pas]. The slope of permeate flow J_{v} [ms^{-1}] against TMP shows a linear relation and was determined by linear regression.

$$L_{\mathrm{p}} = \frac{\eta_{\mathrm{water}} J_{\mathrm{v}}}{\mathrm{TMP}} \tag{112}$$

The parameter a_{p} is estimated based on permeability experiments.

4.3.3 Viscosity

Viscosity measurements were performed with the HAAKE MARS III plate-cone rheometer (Thermo Fisher Scientific Waltham, USA) with sterile filtrated samples. The shear rate $\dot{\gamma}$ [s^{-1}] ranged from 100 to 2000 s^{-1} at a set temperature of 23°C. The measurements were conducted using a titan alloy cone with 1% slope (TiAl5L). The dynamic viscosity for samples which showed no deviation between increasing and decreasing shear rates were evaluated at a high shear rate of 2000 s^{-1} to compensate observed shear thinning effects. This procedure was chosen following Castellanos et al [110], who showed that rheometric measurements at high shear rates approximate Newtonian viscosity for protein solutions with non-Newtonian behavior. The data was used to describe the relative viscosities over the required range of protein concentration by a semi-empirical model.

4.3.4 Experiments

The experiments conducted in lab scale on the ÄKTAcrossflow system are listed in Table 10. This includes the calibration experiment and validation experiments differing in crossflow and TMP condition. The first four experiments are in the format of a two-factorial Design of Experiments (DoE) with the UF/DF condition (TMP 1.4 bar, 395 Lm^{-2}h^{-1}) as center point. The manufacturing scale run was performed with the center point condition on a customized device of known dead volumes. The online data was transformed from time to protein concentration by the theoretical concentration based on the permeate flow which was in very good agreement with offline measurements (not shown).

Table 10: The experiments conducted in lab scale for model calibration and validation. The brackets (+), (0), (-) indicate DoE labels.

Experiment	Buffer condition	TMP [bar]	Crossflow [$Lm^{-2}h^{-1}$]	pH	Acetate [mM]	NaCl [mM]
Validation (a)	UF2	1.8 (+)	511 (+)	5.4	25	10
Validation (b)	UF2	1.0 (-)	272 (-)	5.4	25	10
Validation (c)	UF2	1.0 (-)	511 (+)	5.4	25	10
Calibration (d)	UF2	1.8 (+)	272 (-)	5.4	25	10
Calibration (e)	UF1	1.4 (0)	395 (0)	5.4	46	65
Validation UF/DF	UF1 / UF2	1.4 (0)	395 (0)	5.4	46 / 25	65 / 10

4.3.5 Analytics

The protein concentration in sample was determined by a Lunatic UV/Vis spectrometer (Unchained Labs, UK) at 280 nm including a scatter correction at 320 nm. Samples above 200 g/L were diluted prior to measurement.

4.3.6 Software

All modelling activities and plotting was performed within the MATLAB 2019b (The Mathworks Inc., Natick, MA, USA) environment. The ODE system, presented in the following, was solved with the ODE15s solver. Parameter estimation was performed by solving a least square minimization problem with the MATLAB nonlinear programming solver lsqnonlin. The solver converged with default solver parameters. The confidence intervals were determined by passing the jacobian provided by lsqnonlin to the nlparci function of the Statistics Toolbox.

4.4 Results and discussion

4.4.1 System and membrane description

A prerequisite for describing the flow and pressure behavior during TFF with protein solution is the ability to describe the behavior of pure water. Therefore, the normalized water permeability (NWP) experiment with increasing TMPs, shown in Figure 22, was of interest.

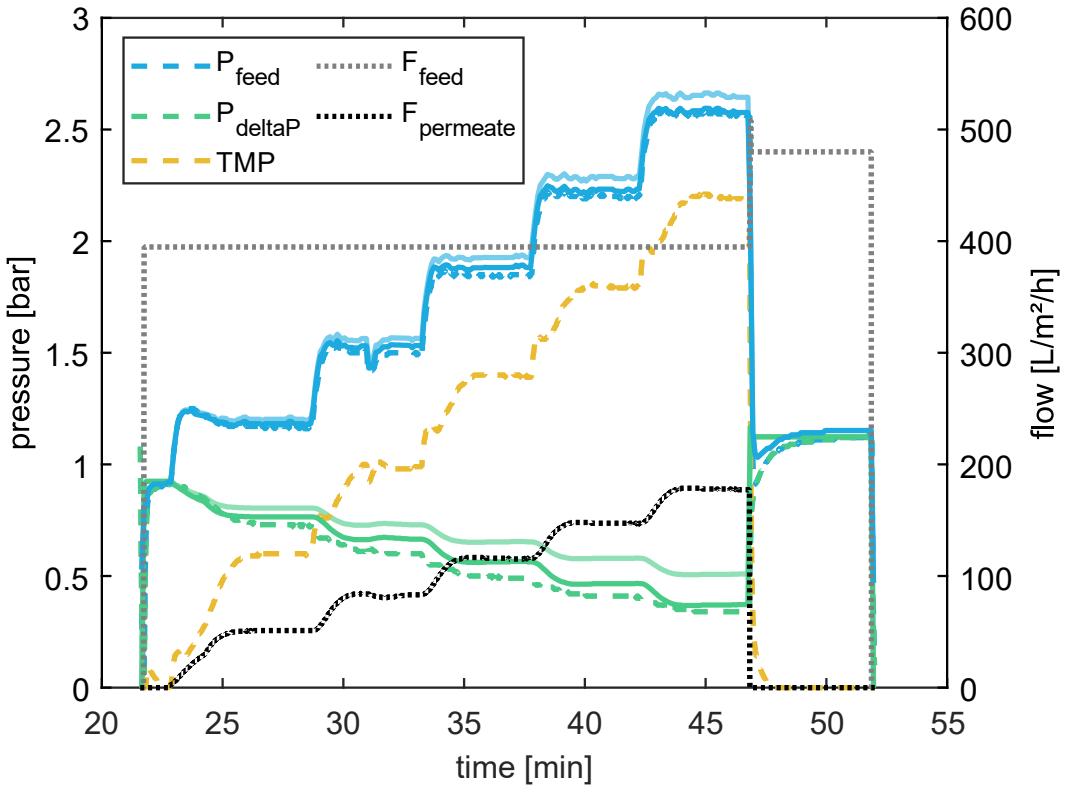

Figure 22: Hydraulic permeability (L_p) estimation based on a normalized water permeability (NWP) experiment. Measurement data is represented in dashed lines and the model in solid lines for the pressure drop and feed pressure. Transparent lines represent model calculation with a_p equal to 1.

For the L_p estimation the permeate flow increases due to a stepwise increase in TMPs at steady crossflow. The estimated permeate flow increase depends on membrane permeability which in turn is affected by e.g., resistant membrane fouling. The L_p estimates for all calibration and validation UF experiments were averaged to L_p to 1.94 mPa with a viscosity of water of $\eta_{H_2O} = 0.932$ mPas at 23 °C. L_p estimates varied depending on the membrane cycle and storage duration with a coefficient of variation of 8 %. For the UF/DF lab scale run, L_p

during UF1 was set to 1.81 mPa, which is in the range of the observed L_p variability, to match the initial flow more accurately.

The membrane feed channel is characterized by its geometry and screen design. Characteristics like the channel height and mesh design (screen) highly influence the feed channel pressure drop [52]. Thus, the pressure drop depends on the membrane condition and fluid dynamics and is not trivial to predict. In addition, the pressure drop is sensitive and can change with new membrane installations due to different torque of membrane fastening. Main process parameters that influence the pressure drop are the crossflow and the viscosity [52]. In Figure 22 a membrane water permeability experiment is shown at constant crossflow but varying TMP. This experiment shows that the additional influence of the permeate flow on the pressure drop at constant crossflow and viscosity is predominant. Thus, the pressure drop cannot be described with the crossflow solely. In addition, a simple subtraction of permeate flow from the crossflow still overpredicted the pressure drop by the pressure drop model (shown by transparent lines). However, the introduced effective crossflow with the constant permeate flow factor described the pressure drop accurately [Eq. (111)]. The factor a_p of 1.33 was determined based on the experiment presented in Figure 22 which led to a better description of the measurement data (solid line). The value for a_p was found to vary for different membrane types. The remaining parameters k_p and k_l were estimated based on initial pressure drop data of UF (a,b) experiments. The estimated k_p was 3.66e-10 m² and k_l was 2.40e-4 m, which is in the order of magnitude compared to Kaiser et al. [108].

4.4.2 Viscosity model

This section describes the parameter determination as required for Eq. (104). First, the viscosity was described by a fit based on off-line rheometer data to estimate c_{max} and b. The results are shown in Figure 23. The viscosity of the high ionic strength condition (Buffer 1) during UF1 was above the viscosity of the UF2 at low salt condition (Buffer 2). This can be interpreted as shielding of repulsive charges of the protein leading to stronger attractive interactions [102]. However, for this protein the difference in viscosity was not strongly pronounced. Compared to full length mAbs viscosity measurements, the viscosity of the molecule is on the lower end [111].

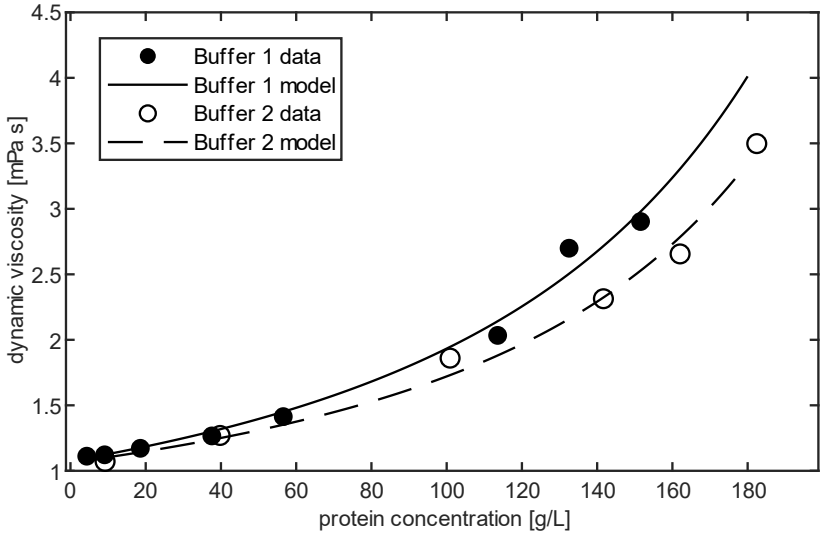

Figure 23: Mooney equation fitted to viscosity data. Buffer 1 represents the first ultrafiltration step condition and Buffer 2 the final ultrafiltration condition.

4.4.3 Osmotic pressure

In literature, the osmotic pressure is widely studied during ultrafiltration to understand the impact of different buffer conditions on filtration performance [102,103]. The measurement of the osmotic pressure of highly concentrated protein solutions, however, is time consuming and difficult to achieve with high accuracy [112]. Thus, theoretical values for the osmotic pressure were calculated. The virial coefficient $B_1 = 0.021$ kgmol^{-1} can be directly calculated as described in Chapter 4.2.2. The second virial coefficient B_2 [molm^{3}kg^{-2}] was included considering the proteins excluded volume contribution in Eq. (113) [104,113]:

$$B_2 = \frac{16}{3}\left(\frac{\pi r_\mathrm{p}^3 N_A}{M_\mathrm{p}^2}\right) \tag{113}$$

which depends on the protein radius r_p [m] and resulted in a B_2 of 5.74e-05 molm^{3}kg^{-2}. The B_3 is then given by $B_3 = \frac{5}{8}B_2^2$ according to Vilker et al. [105]. The inclusion of the integral over the potential of mean force [106] could not improve the model performance and was therefore neglected. To that, the difference between high salt (e) and low salt (a,b,c,d) could be described by the viscosity differences solely. This might be explained by the strong correlation of viscosity and B_2 [114,115]. In addition, small errors of the osmotic pressure could be compensated by the correlated parameter k_0. The resulting osmotic pressure was in the lower range of measurements presented by Binabaji et al. [103].

4.4.4 Inverse calibration and validation

The aim of a mechanistic approach is to extrapolate to conditions that are not present in the calibration set. If the model reacts correctly to input parameter changes, the model can be applied to explore a process parameter space. As mentioned previously, the process control parameters of interest are TMP and crossflow. The results of the DoE are presented in Figure 24 with the applied conditions listed in Table 10. In the following the inverse calibration and validation is discussed.

4.4.4.1 Permeate model

As pointed out by Baek et al. [97], c_w can be set constant and was found to be not sensitive above a certain value. Furthermore, the parameter c_w cannot be larger than c_{max} when solving for J_v without causing numerical issues. To ease the estimation problem and fix non-sensitive parameters [88] c_w could be set to c_{max} after confirming low sensitivity. Assuming an initial R^* equal to one, the remaining parameter to be determined was k_0. Although k_0 is related to membrane properties and the diffusion coefficient, inputs like the characteristic channel diameter are not trivial to determine but show a strong influence on k_0. Therefore, k_0 was estimated on UF experiment (d). Experiment (d) was chosen, because the condition of high TMP and low crossflow should theoretically induce a strong concentration polarization effect suitable for parameter estimation. To emphasize this strategy, estimating the parameters on UF experiments with low polarization effects, such as experiment (c), the model was found to have diminished predictive power for experiments with increased polarization effects. The best fit of the permeate flow is presented in Figure 24 in a grey solid line. The permeate flow for concentration below 50 g/L was underpredicted which could not be compensated by k_0, c_w nor by the virial coefficients B_2, B_3. Thus, the model showed a clear limitation caused by J_{lim}, which is not infinite even for very low concentration where no concentration polarization occurs. However, R^* was used to compensate for this limitation at low protein concentration. The result of the parameter estimation is shown in Figure 24 with an R^* of 0.70 and k_0 of 4.04e-5 ms^{-1}. In general, a smaller protein results in a higher k_0 due to increase of the diffusion coefficient. Under this assumption the estimated k_0 is comprehensible compared to 1.6e-5 ms^{-1} of a mAb [55]. The remaining model to measurement deviations observed in Figure 24 could not be further improved by solving the model along the membrane as suggested in recent Single Pass Tangential Flow Filtration (SPTFF) studies [101,108]. On the contrary, the model solution became significantly slower, so this approach was not pursued further.

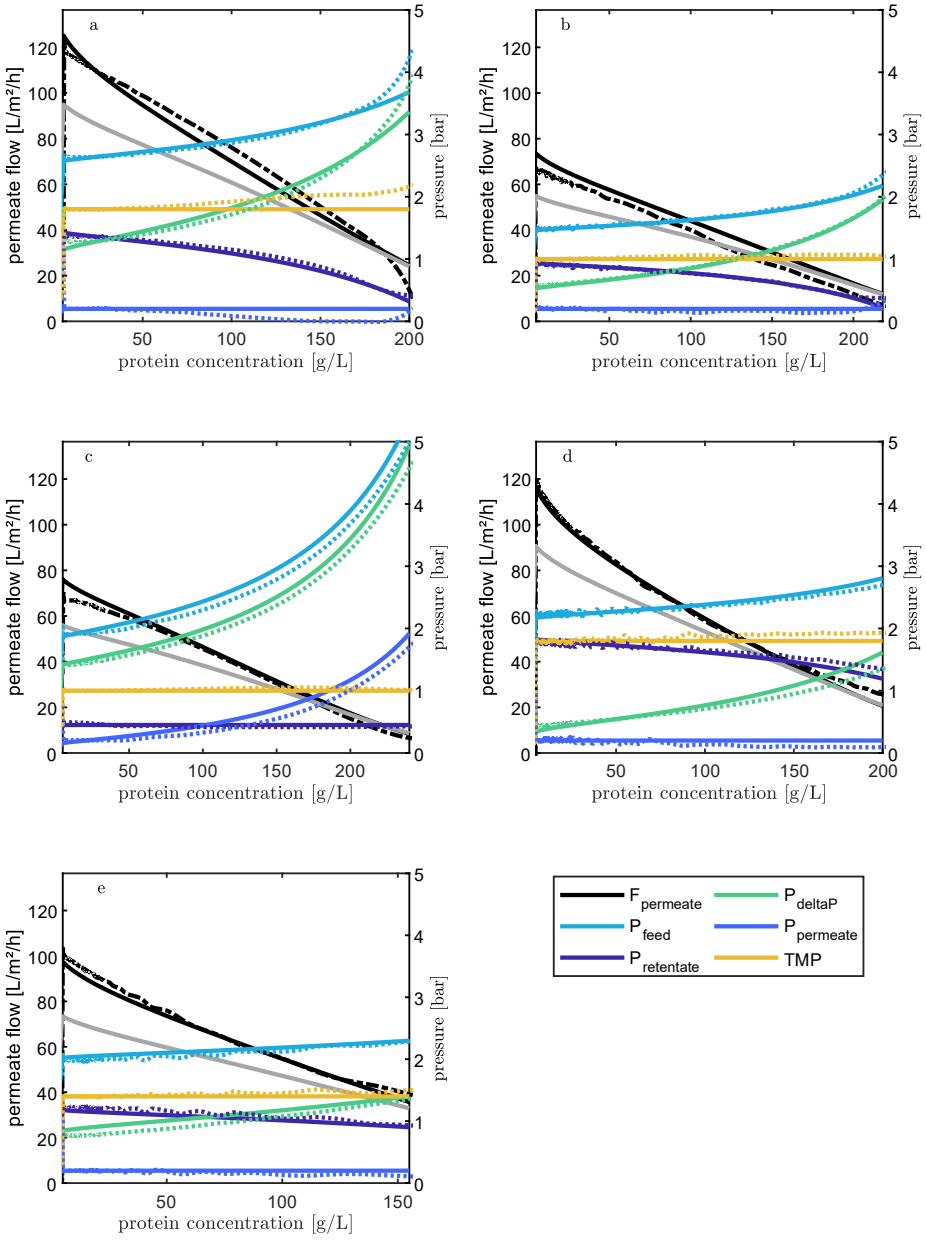

Figure 24: Model calibration (d) and validation (a,b,c,e) experiments. The measurement online data is represented in dashed lines and the model simulation in solid lines. Calibration experiment (d) was used to estimate k_0, R^* and b^*. The grey lines represent the result with R^* equal to one.

4.4.4.2 Pressure drop model

It is common knowledge, that the UF pressure drop increases with increasing solution viscosity which is dominated by the TFF membrane. For the pressure drop in this study, the Mooney equation model resulted in an overprediction of pressure for concentration above approximately 100 g/L (not shown). This is

caused by the feed channel characteristics reducing the effect of viscosity on pressure drop at high protein concentration which is a phenomenon known and published by the manufacturer [116]. A reduction of the b parameter to b^* based on experimental data (d), showed very good agreement of the pressure drop model for all experiments as shown in Figure 24. All determined model parameters are listed in Table 11. The table incorporates the confidence interval for parameter estimates. Wide confidence intervals were observed for the Mooney equation and the pressure drop function. This includes the parameters $b, c_{\max}$, k_P, and k_l. Based on the Fisher Information Matrix, parameter correlation could be identified as the root cause for the wide intervals. Consequently, the physical interpretation of these parameters should be approached with caution. Nevertheless, the model accurately described the viscosity and pressure drop data as presented in Figure 22, Figure 23, and Figure 24. The model prediction on the validation experiments (a,b,c,e) for the filtrate flow in Figure 24 showed acceptable results. Experiment (b) and (c) were in very good agreement with the model. However, the condition of high TMP and crossflow (a) slightly underpredicted the permeate flow.

Table 11: List of model parameters. In the context of the permeate flow model, the parameters k_0 and R^* were derived through estimation using UF permeate flow data. The parameter b^*, required for calibrating the pressure model, relies on UF data as well. However, certain parameters such as b and c_{max} for the permeate flow model, as well as the parameter a_p based on NWP data, can be determined beforehand without relying on protein UF data.

Parameter	Value	95 % confidence interval	Estimated on
k_0 [ms^{-1}]	4.04e-5	[4.00e-5, 4.09e-5]	Permeate flow curve of UF (d)
R^* [-]	0.70	[0.696, 0.704]	Permeate flow curve of UF (d)
k_p [m²]	3.66e-10	[-2.08e-9, 2.82e-9]	Initial pressure of UF (a,b)
k_l [m]	2.40e-4	[-10.33e-4, 15.13e-4]	Initial pressure of UF (a,b)
b [-]	4.70e-3 (UF1) 3.69e-3 (UF2)	[3.32e-3, 6.10e-3] [3.09e-3, 4.28e-3]	Rheometer data
b^* [-]	1.00e-3 (UF1) 2.19e-3 (UF2)	[0.99e-3, 1.01e-3] [2.18e-3, 2.20e-3]	Pressure curve of UF (d) Pressure curve of UF (e)
$c_\mathrm{w} = c_\mathrm{max}$ [g/L]	504 (UF1) 427 (UF2)	[98.82, 909.60] [319.20, 534.81]	Rheometer data
a_p [-]	1.33	[1.12, 1.54]	NWP
A_cs [m²]	5.28e-6	-	(Binabaji et al., 2016)
ρ [kgm^{-3}]	$1017.3 + 0.163c_\mathrm{p}$	-	Determined based on density measurements
r_p [m]	2.35e-9	-	-
R [Jmol^{-1}K^{-1}]	8.314	-	-
T [K]	298.15	-	-
M_p [gmol^{-1}]	~ 50,000	-	-
A_m [m²]	88e-4	-	-

The condition of experiment (c) was challenging due to the high-pressure crossflow and low TMP. To ensure TMP control, the ÄKTAcrossflow controlled the TMP with a permeate pressure reaching levels above the retentate pressure. For this event, the retentate pressure is controlled at 0.45 bar and the permeate pressure is then given by Eq. (114).

$$P_\mathrm{Permate} = P_\mathrm{Retentate} + \frac{\Delta P}{2} - TMP \tag{114}$$

The point L^* [m] within the membrane length, where the feed side pressure theoretically equals the permeate pressure was derived by Eq. (107):

$$P_{\text{Permate}} = P_{\text{Feed}} - \frac{\Delta P}{L} L^* \tag{115}$$

and results in

$$L^* = \frac{(P_{\text{Feed}} - P_{\text{Permeate}})}{\frac{\Delta P}{L}} \tag{116}$$

Hence, in case of $L^* < L$ the integration upper limit L in Eq. (104) is replaced by L^*. With the presented equations, the model was able to predict the filtration for the condition of experiment (c) as shown in Figure 24. With this adjustment the model is capable to describe the filtration and pressure behavior under complex process control conditions. In conclusion, the presented model was capable to predict, outside the calibration set, the permeate flow and the pressure drop of UF2 and UF1 of the validation experiments.

To describe the entire UF/DF process, a simple transition between the UF models for the pressure drop and permeate flow was applied as presented by Eq. (117) - (119) for an unretained salt component $i = \text{DF}$. The exchange of the component x_{DF} [-] is 0 at the end of UF1 and approaches 1 towards UF2. Thus, during DF both UF models were solved and were offset against each other to obtain combined pressure drop and permeate flow.

$$\frac{dx_{\text{DF}}}{dt} = \frac{F_{\text{buffer}}\left(c_{s,\text{DF},buffer} - c_{s,\text{DF}}\right)}{V} \tag{117}$$

$$F_{\text{permeate,DF}} = (1 - x_{\text{DF}}) F_{\text{permeate,UF1}} + x_{\text{DF}} F_{\text{permeate,UF2}} \tag{118}$$

$$\Delta P_{\text{DF}} = (1 - x_{\text{DF}}) \Delta P_{\text{UF1}} + x_{\text{DF}} \Delta P_{\text{UF2}} \tag{119}$$

Although a simple transition between the UF models is a simplified estimation for the DF process, the model results are in good agreement with the data as shown in Figure 25. The UF/DF conditions are extrapolated conditions regarding TMP and crossflow and thus were not included in the model calibration.

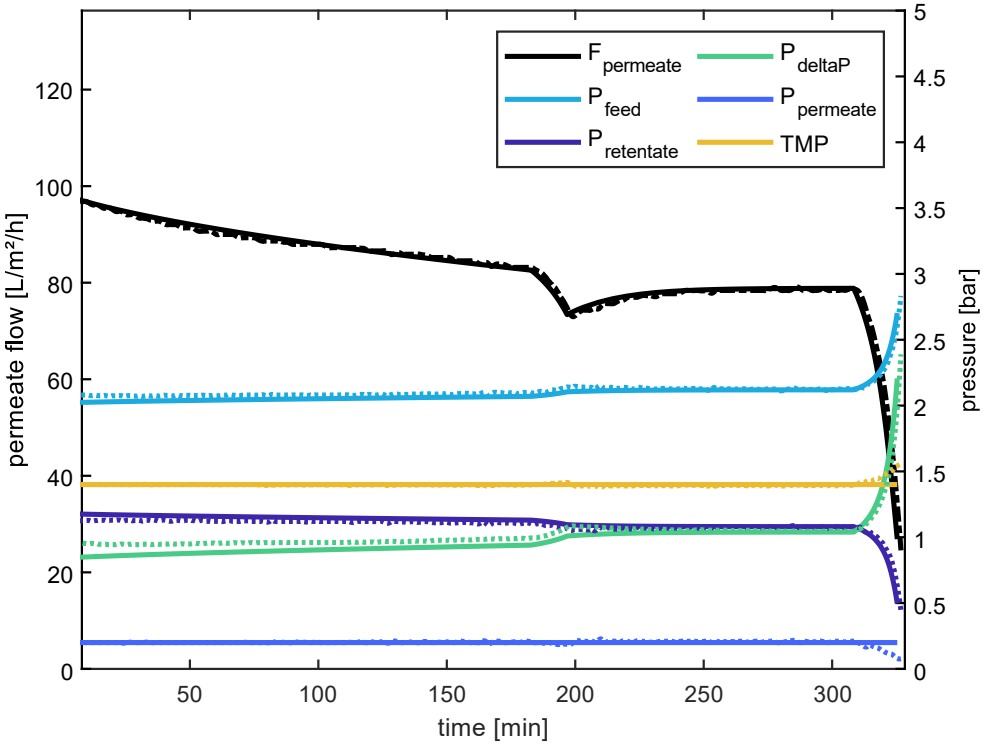

Figure 25: UF/DF model prediction. At 200 min the UF1 ends and at 310 min the UF2 starts. The presented conditions of TMP 1.4 and CF of 395 Lm^{-2}h^{-1} were not used for model calibration.

4.4.5 Scale-up

The presented UF/DF model calibrated at small-scale was used to extrapolate to manufacturing scale. The total membrane area at manufacturing scale was above 25 m². The estimated $L_P\eta_0^{-1}$ of 1.17e-10 [ms^{-1}Pa] of the membrane system was determined by equilibration data. A control difference to the small-scale experiments was the constant pressure drop control during UF1 and DF instead of a constant crossflow. The relation of pressure drop and crossflow is given by Eq. (110). Therefore, the model could be solved to compensate the calculated pressure drop by change in crossflow. For the final UF2 a constant crossflow was set. The model prediction of the manufacturing run is presented in Figure 26. At the end of the UF1 phase, which ends at 67 minutes, a flush is performed before the end of the phase. This leads to abrupt flow and pressure changes in the measured data. The description of the manufacturing data required adjustments of two parameters. First, the pressure drop was underpredicted and thus k_P adjusted to 2.1e-10 [m] to meet the measurement data. Next, the $L_P\eta_0^{-1}$ was reduced to 1.04e-10 [ms^{-1}Pa] to accurately meet the initial permeate flow at the start of the UF1. Including the mentioned adjustments, an acceptable description of the manufacturing process could be achieved. The required parameter adjustments are indicators for possible scale

effects. The increased pressure drop compared to small scale might be caused by stronger installation torque resulting in reduced distance of the membrane sheets and thus a pressure drop increase. The difference in membrane permeability can vary due to potential membrane fouling and differences in flow characteristic and thus required minor adjustments. Despite the minor adjustments, the extrapolation ability of the model as well as the switch from crossflow control in lab scale to pressure drop control in manufacturing scale underlines the physical relevance of the derived model and estimated parameters. One possible application of the presented model is to improve the understanding of the mentioned scale effects and thus provide guidance up to process transfer.

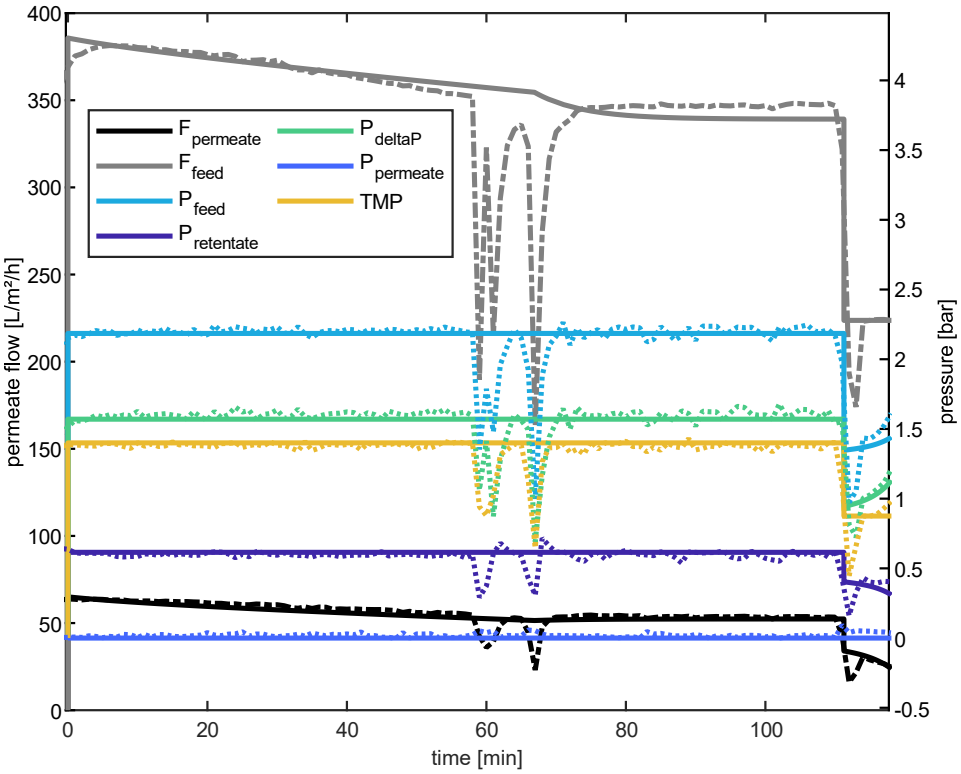

Figure 26: Scale-up prediction of manufacturing run. The UF 1 ends at 67 min and the UF 2 starts at 90 min. The data includes a flush before the end of UF1 resulting in abrupt flow and pressure changes which are not included in the model.

4.5 Conclusion

For industrial UF/DF process development a fast and reliable model solution is required to investigate the process robustness from early development phases on. The presented UF/DF model had only three parameters (k_0, R^*, b^*) that can be estimated on a single UF experiment. All other parameters could be determined by permeability tests and offline viscosity measurements. From

there the model was able to extrapolate to changes in crossflow and TMP combinations for a wide concentration range of 5 to 200 g/L. This was a particular challenge due to the transition from membrane-limited to polarization-limited permeate flow phases. Furthermore, the DF phase was successfully approximated based on the two UF models. The pressure control characteristics of the ÄKTAcrossflow, such as a permeate pressure increase, were successfully covered by the model. However, the manufacturing data showed an increased pressure drop and decreased membrane permeability compared to small-scale data. This could be successfully compensated by adjusting one pressure model parameter and the membrane permeability. In conclusion, the study demonstrated the potential of accompany process development with a mechanistic UF/DF model approach. The presented model required minimal calibration effort to successfully describe lab scale and manufacturing scale filtration data.

4.6 Acknowledgements

The authors would like to acknowledge Elaheh Binabaji for scientific discussion.

5 Connected mechanistic process modeling to predict a commercial biopharmaceutical downstream process

Federico Rischawy[a,b], Till Briskot[a], Nathalie Hopf[a], David Saleh[a], Gang Wang[a], Simon Kluters[a], Joey Studts[a], Jürgen Hubbuch[b]

[a] DSP Development, Boehringer Ingelheim Pharma GmbH & Co. KG, Biberach, Germany

[b] Karlsruhe Institute of Technology (KIT), Institute of Engineering in Life Sciences, Section IV: Biomolecular Separation Engineering, Karlsruhe, Germany

Corresponding author: Jürgen Hubbuch, Tel.: +49 721 608 47526, **juergen.hubbuch@kit.edu**

Abstract

Mechanistic modeling has shown to contribute greatly to the process understanding of chromatography and filtration processes. However, these are mostly considered individually and not connected for an entire downstream process. In this study, mechanistic models were connected to describe an entire downstream process of a Fab fragment. For the capture step, a transport-dispersion model (TDM) combined with an extended Langmuir isotherm was applied. Depth filtration was modeled with a combined pore blocking model. The polishing ion-exchange chromatography steps were described by a TDM combined with the colloidal particle adsorption model. The tangential flow filtration model accounts for both the Donnan effects and flow limitations. The presented downstream process model could predict online and offline data recorded at 12,000 L manufacturing scale. Process variations of 23 manufacturing batches were adequately reproduced by the model based on the consideration of input process parameter variations.

5.1 Introduction

Antibody-based therapy for cancer has become one of the most successful and important strategies for treatment of various tumors [7,8]. However, the biopharmaceutical industry is experiencing an increasingly competitive environment and thus a requirement for cost savings and efficiency. In addition, the trend towards non-standard formats such as bispecific antibody formats [19], antibody-drug conjugates [20], antibody fragments [21], and others [22] poses major challenges for a wet-lab process development. The divergent process behavior of biopharmaceutical drug candidates requires flexibility and generally does not allow generalization of process conditions and control strategies. This results in increased resource and time requirements when relying on a purely experimental approach. Therefore, to save time and experiments, prior process knowledge in form of mechanistic models can be used to explore the process behavior *in silico*. Since mechanistic models heavily rely on process knowledge and physical laws, they are particularly relevant when limited data is available. In other industries, e.g. chemical engineering, Process System Engineering (PSE) models, which are primarily based on mechanistic models, have proven their value for decades by increasing the industry efficiency from a process design and operations perspective [61]. Likewise in pharmaceutical industry, PSE already contributes by generating process knowledge and evaluating different operational scenarios [117]. Although biopharmaceutical industry is slightly behind using PSE, the trend towards taking advantage of these technologies to meet future challenges is clear [44,66,71,73,81,118–122]. The delay comes from the fact that the biopharmaceutical unit operations are biologically complex and mechanistically difficult to describe [65]. Moreover, biopharmaceutical unit operations are currently considered individually in both modeling and experimental approaches.

However, the connection of mechanistic models to a connected mechanistic process model (CMPM) would allow *in silico* investigations of multidimensional combination and interaction of input variables and process parameters across unit operations. Consequently, a cross-process understanding emerges that would meet demands by the regulatory authorities (ICH Q8 (R2)) [24]. In addition, a CMPM potentially would loosen up the robustness investigations regarding potential upstream (USP) variability, which can be considered one of the main sources of variability propagated through the entire downstream process. Especially, the effect of possible feed composition variability is difficult to be captured experimentally due to limited feedstocks in development stages and long processing time. Prior to benefit from models' application, utmost attention needs to be paid to ensure the representativeness of the models for

their real counterparts to avoid misleading results. This can include the validation of scale independence and extrapolation capability. In this context, a former work demonstrated that the connection of mechanistic models is capable to describe a biopharmaceutical polishing sequence from lab to manufacturing scale and predict manufacturing variability based on input variability [119]. Other studies also proposed the advantages of connected chromatography simulations [69–72]. To our best knowledge, a mechanistic model for the entire downstream process, including pH adjustment and filtrations steps, has not yet been published.

In this study, a complete biopharmaceutical downstream process from capture to UF/DF was described by connected mechanistic models. The initial model discrimination aimed at minimizing model complexity and the number of parameters, but still achieving extrapolation capabilities. The final calibrated models were connected to a CMPM and tested for its scale-independence at 12,000 L fermenter scale. Furthermore, the CMPM was tested to react accordingly to real input parameter variability in manufacturing scale regarding protein concentration, volume, size variant composition, ion concentration, and pH. This study shows a downstream process can be represented by an CMPM, which opens unexplored possibilities to accelerate the process development whilst saving resources.

5.2 Theory

5.2.1 Manufacturing process

The downstream process in this study is presented schematically in Figure 27. The sequence of ten consecutive chromatography, adjustments, and filtration steps is typical for the purification of therapeutic proteins [14,16]. The process starts with a capture chromatography step (Unit I), where the protein is bound under neutral pH condition, followed by three wash steps, and eluted via low pH. The capture step is performed in multiple cycles depending on the titer in the harvested cell culture fluid (HCCF) and subsequently pooled. The resulting pool is hold at low pH to inactivate potential viruses and subsequently adjusted to neutral pH with 1 M Tris (Unit II: Virus inactivation). Resulting turbidities are clarified via depth filtration (Unit III). The clarified pool is adjusted to pH 8 with 1 M Tris (Unit IV: Adjustment 1) and loaded on the anion-exchange chromatography (AEX) column (Unit V), as the first polishing chromatography step, operated in flow-through mode. Afterwards the pool is adjusted to pH 4.9 with 1 M acetic acid (AcOH) in Unit VI (Adjustment 2) and loaded on the second polishing cation-exchange chromatography (CEX) column (Unit VII). The CEX is performed in bind-and-elute mode, where the elution is accomplished via salt

step elution. Unit V – VII can be performed in either one or two trains, depending on the loading condition. In case of two trains, the CEX elution are pooled before being adjusted to pH 5.5 with 0.1 M NaOH in Unit VIII (Adjustment 3). Unit IX is an orthogonal virus filtration step to Unit II and removes potential viruses by size. The last Unit X is the ultrafiltration/diafiltration (UF/DF) used for final buffer exchange and pool concentration. In this study, a model for every process unit is built and connected in sequence including pH, ions, protein concentration, size variants and volume. In the following, the models used to describe the downstream process are presented.

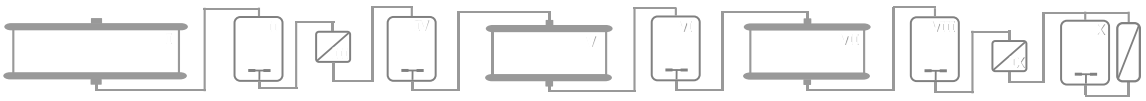

Figure 27: Scheme of manufacturing process: I - capture, II - pH virus inactivation, III - depth filtration, IV - adjustment 1, V – anion-exchange chromatography, VI - adjustment 2, VII – cation-exchange chromatography, VIII - adjustment 3, IX - virus filtration, X - UF/DF

5.2.2 Chromatography models

All models of chromatography units were simulated using the transport-dispersion model (TDM) [Eq. (65)] in combination with a binding model describing the interaction between protein and resin. The dimensions of the chromatography column are defined by the diameter d_C [m] and the length L_C [m] which is the upper bound of the axial position $x \in [0, L_\mathrm{C}]$. Equation (65) describes the change in the bulk concentration of solute j $c_{\mathrm{b},j}$ [molm^{-3}] over time and over column length. The solute bulk concentration in the particle of radius r_p [m] is represented by c_P [molm^{-3}].

$$\begin{aligned}\frac{\partial c_{\mathrm{b},j}}{\partial t}(x,t) = \; & -u_\mathrm{int}(t)\frac{\partial c_{\mathrm{b},j}}{\partial x}(x,t) + D_\mathrm{ax}\frac{\partial^2 c_{\mathrm{b},j}}{\partial x^2}(x,t) \\ & -\frac{1-\varepsilon_\mathrm{v}}{\varepsilon_\mathrm{v}}\frac{3}{r_\mathrm{p}}k_{\mathrm{eff},j}\left(c_{\mathrm{b},j}(x,t) - c_{\mathrm{p},j}(x,t)\right)\end{aligned} \tag{120}$$

Additional parameters are the flowrate, given as the interstitial velocity of the mobile phase u_int [ms^{-1}], the axial dispersion coefficient D_ax [m^{2}s^{-1}], the void fraction ε_v [-], and the effective mass transfer coefficient k_eff [ms^{-1}] [27]. The TDM is completed with Danckwerts' boundary conditions at the column inlet and outlet [36]:

$$\frac{\partial c_{\mathrm{b},j}}{\partial t}(x=0,t)=\frac{u_{\mathrm{int}}(t)}{D_{\mathrm{ax}}}(c_{\mathrm{b},j}(x=0,t)-c_{\mathrm{inlet},j}(t)) \tag{121}$$

$$\frac{\partial c_{\mathrm{b},j}}{\partial t}(x=L_{\mathrm{C}},t)=0 \tag{122}$$

where $c_{\mathrm{inlet},j}$ [molm^{-3}] represents the column inlet concentration. The lumped rate model (LRM) assumes a constant c_{P} inside the particle:

$$\frac{\partial c_{\mathrm{p},j}}{\partial t}(x,t)=\frac{3}{r_{\mathrm{p}}}\frac{k_{\mathrm{eff},j}}{F_{\mathrm{acc},j}\varepsilon_{\mathrm{P}}}\left(c_{\mathrm{b},j}(x,t)-c_{\mathrm{p},j}(x,t)\right)-\frac{1-\varepsilon_{\mathrm{P}}}{F_{\mathrm{acc},j}\varepsilon_{\mathrm{P}}}\frac{\partial q_{\mathrm{v},j}}{\partial t}(x,t) \tag{123}$$

where ε_{P} [-] is defined as the particle porosity and the solute adsorbed on the particles stationary phase as q_{v} [molm^{-3}]. The pore accessibility factor:

$$F_{\mathrm{acc},j}=\frac{\varepsilon_{\mathrm{P},j}}{\varepsilon_{\mathrm{P}}} \tag{124}$$

ranges from (0,1] and accounts for size exclusion effects due to lower protein porosity $\varepsilon_{\mathrm{P},j}$ compared to that of salt under non-binding conditions. However, $F_{\mathrm{acc},j}$ [-] was fixed for all protein species j to avoid inconsistencies when using binding models.

5.2.2.1 Capture chromatography

For the capture chromatography model, the elution behavior under varying pH [-] can be described by a Langmuir based binding model. The binding model in Eq. (125) was originally developed by Lane and Przybycien for Protein A affinity chromatography [123,124]:

$$\frac{\partial q_{\mathrm{v},i}}{\partial t}=k_{\mathrm{kin},i}\left(q_{\max}\frac{k_{\mathrm{eq},i}c_{\mathrm{p},i}}{\left(1+10^{\mathrm{p}K_{\mathrm{a}}'-pH}\right)\left(1+10^{\mathrm{p}K_{\mathrm{a}}''-pH}\right)}\left(1-\sum_{i=1}^{n}\frac{q_{\mathrm{v},i}}{q_{\max}}\right)-q_{\mathrm{v},i}\right) \tag{125}$$

where the protein bound to the resin skeleton volume $q_{\mathrm{v},i}$ [molm^{-3}] depends on the solutions pH. The effective pH where the interaction complex of the ligand protein ($\mathrm{p}K_{\mathrm{a}}'$) and target protein ($\mathrm{p}K_{\mathrm{a}}''$) changes is represented by effective $\mathrm{p}K_a$ [-] parameters. The maximum achievable binding capacity is given by $q_{\max}$ [molm^{-3}], the equilibrium coefficient by $k_{\mathrm{eq},i}$ [m^{3}mol^{-1}], and the kinetic parameter by $k_{\mathrm{kin},i}$ [s]. For model calibration, the parameters $q_{\max}$, $k_{\mathrm{eq},i}$, $\mathrm{p}K_{\mathrm{a}}'$ and $\mathrm{p}K_{\mathrm{a}}''$s were estimated on experimental data.

5.2.2.2 Ion-exchange chromatography

To describe the binding behavior of a protein on an ion-exchange adsorber surface the colloidal particle adsorption (CPA) model was applied [45]. This

model assumes the protein to be a perfect sphere with radius a_j [m] which binds to the resin skeleton volume by:

$$\frac{\partial q_{\mathrm{v},i}}{\partial t} = k_{\mathrm{kin},i}\left(K_{\mathrm{v},i}c_{\mathrm{p},i} - q_{\mathrm{v},i}\right) \tag{126}$$

with the kinetic parameter:

$$k_{\mathrm{kin},i} = k^{*}_{\mathrm{kin},i}\frac{1}{2}\left(\frac{u_{\mathrm{A},i}\left(\delta_{\mathrm{m},i}\right)}{k_{\mathrm{b}}T}\right)^{2}\frac{1}{\cosh\left(\frac{u_{\mathrm{A},i}\left(\delta_{\mathrm{m},i}\right)}{k_{\mathrm{b}}T}\right) - 1} \tag{127}$$

which contains the Boltzmann constant k_{b} [JK^{-1}], the temperature T [K], and the fitting parameter $k^{*}_{\mathrm{kin},i}$ [s^{-1}]. The function $u_{\mathrm{A},i}\left(\delta_{\mathrm{m},i}\right)$ [J] in Eq. (70) represents the minimum of the interaction energy between the colloid and the adsorber surface given at the distance $\delta_{\mathrm{m},i}$ [m]. This interaction energy depends on the fitting parameter protein charge Z_i, the ionic strength I and pH. The equilibrium coefficient $K_{\mathrm{v},i}$ [-] in Eq. (69) is given by:

$$K_{\mathrm{v},i} = \Delta_i B_i(\Theta)\frac{k_{\mathrm{b}}T}{u_{\mathrm{A},i}\left(\delta_{\mathrm{m},i}\right)}\exp\left(-\frac{u_{\mathrm{lat},i}}{k_{\mathrm{b}}T}\right)\left(1 - \exp\left(-\frac{u_{\mathrm{A},i}\left(\delta_{\mathrm{m},i}\right)}{k_{\mathrm{b}}T}\right)\right) \tag{128}$$

The fitting parameter Δ_i[-] represents the boundary layer thickness in which electrostatic interaction is enabled. The lateral interaction energy is represented by $u_{\mathrm{lat},i}$ [J] and depends on the fitting parameter lateral charge $Z_{\mathrm{lat},i}$ [-]. The equilibrium coefficient further includes the available surface function $B_i(\Theta)$ [-]:

$$B_i(\Theta) = (1-\Theta)\exp\left(-\frac{\pi a_i^2\sum_j q_j N_{\mathrm{A}} + 2\pi a_i\sum_j a_j q_j N_{\mathrm{A}}}{(1-\Theta)} - \frac{\pi a_i^2\left(\sum_j a_j q_j N_{\mathrm{A}}\right)^2}{(1-\Theta)^2}\right) \tag{129}$$

which accounts for steric hindrance at high protein concentration. The term N_{A} represents the Avogadro number and q_j [molm^{-2}] is the protein bound to the adsorber surface. The surface coverage Θ [-] in Eq. (129) is given by:

$$\Theta = \pi N_{\mathrm{A}}\sum a_i^2\frac{q_{\mathrm{v},i}}{A_{\mathrm{s},i}} \tag{130}$$

which depends on the specific adsorber surface $A_{\mathrm{s},i}$ [m^{-1}] and is estimated on experimental data. The derivation of the model and a more detailed description can be found in previous publications [42,44,45].

5.2.3 Pool adjustment model

The adjustment model considers a system of mixed ion solution and a sphere protein of outer radius a [m] in electroneutral equilibrium. To determine the pH of the solution with changing ion composition, the influence of ionic strength, buffer components, protein concentration, and protein charge, which is itself a function of pH, need to be described. Therefore, a Wigner-Seitz cell (WS) model was used [58,125].

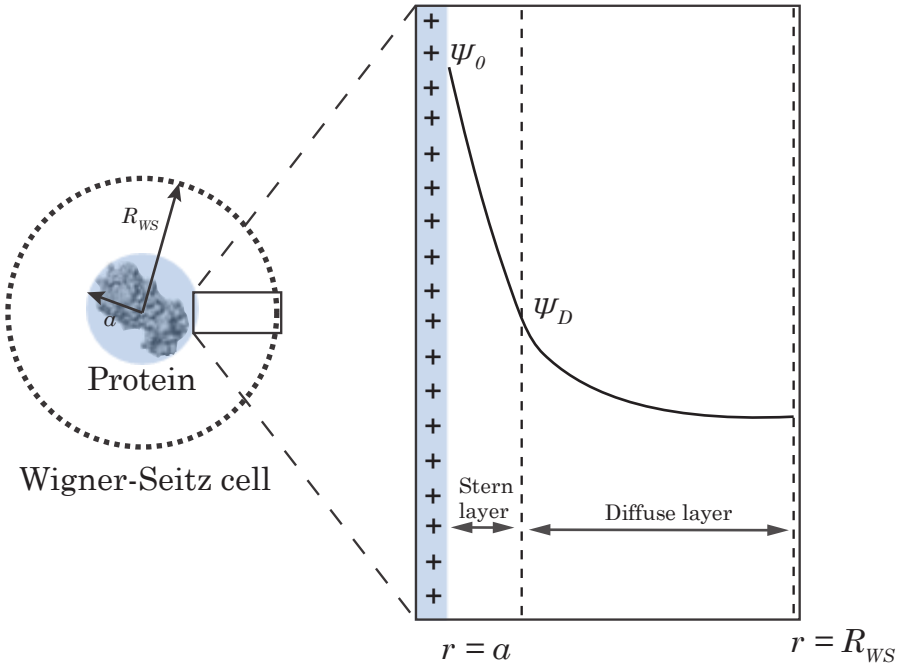

Figure 28: Schematic illustration of the Wigner Seitz Cell which is divided into a Stern layer and a diffuse layer.

This model allows to reduce the problem to a single cell as illustrated in Figure 28. The radius R_{WS} [m] of the WS cell can be directly related to the molar protein concentration in the bulk by:

$$R_{\mathrm{WS}} = \left(\frac{3}{4\pi N_{\mathrm{A}} c_{\mathrm{b}}}\right)^{\frac{1}{3}} \tag{131}$$

The double layer between the protein surface and the WS cell is divided into a Stern and a diffuse layer as presented in Figure 28. The basic Stern model [77] discussed in previous work [58,119] is used to describe the electric potential within the charge-free Stern layer by a linear relation given by the Stern capacitance:

$$C_{\mathrm{S}} = \frac{\sigma}{\psi_0 - \psi_{\mathrm{D}}} \tag{132}$$

where σ [Cm^{-2}] represents the charge density at the protein surface, ψ_0 [V] represents the potential at the protein surface, and ψ_{D} [V] is the potential at the origin of the diffuse layer. Inside the diffuse layer the potential is described by the following Poisson Boltzmann (PB) equation:

$$\begin{aligned} &\frac{\partial^2\psi}{\partial r^2}(r) + \frac{2}{r}\frac{\partial\psi}{\partial r}(r) \\ &= -\frac{eN_{\mathrm{A}}}{\varepsilon\varepsilon_0}\sum_i\sum_j z_{i,j}\bar{c}_{i,j}(\overline{\mathrm{pH}})\exp\left(-z_{i,j}\frac{e}{k_{\mathrm{b}}T}\left(\psi(r) - \overline{\psi}\right)\right) \end{aligned} \tag{133}$$

with the first boundary condition ensuring a vanishing electric potential for the closed stirred tank system:

$$\psi(r = R_{\mathrm{WS}}) = 0 \tag{134}$$

and the second boundary condition ensuring electroneutrality within the WS:

$$\frac{\partial\psi}{\partial r}(r = a) = -\frac{\sigma}{\varepsilon\varepsilon_0}. \tag{135}$$

For the second boundary condition ε_0 [CV^{-1}m^{-1}] denotes for the vacuum permittivity and ε [-] represents the relative permittivity for water of 78.3. The index i represents a solute component and j the ionization states of the solute. The average ion component concentration $\bar{c}_{i,j}$ [molm^{-3}] in the diffuse layer for a certain $\overline{\mathrm{pH}}$ can be calculated by their pK_{a} values according to Ladwig et al. [59,119]. The average electric potential $\overline{\psi}$ [V] inside the WS cell as required for the PB equation is given by:

$$\overline{\psi} = -\frac{k_{\mathrm{b}}T}{ez_{i,j}}\ln\left(\frac{3}{(R_{\mathrm{WS}}^3 - a^3)}\int_a^{R_{\mathrm{WS}}}\exp\left(-z_{i,j}\frac{\psi(r)}{k_{\mathrm{b}}T}r^2dr\right)\right) \tag{136}$$

and the protein surface charge by:

$$\sigma = \frac{e}{4\pi a^2}\sum_k N_k\Big((\zeta_k - 1)[1 + 10^{\mathrm{p}K_k - \mathrm{pH}_0}]^{-1} + \zeta_k[1 + 10^{\mathrm{pH}_0 - \mathrm{p}K_k}]^{-1}\Big) \tag{137}$$

which is required for the second boundary. The protein surface charge depends on the number of charged amino acids N_k [-] in the primary sequence, ζ [-] the charge of the protonated side chain k, and the pK_k [-] of the side chain. The pH at the protein surface in Eq. (76) relates to the average pH by:

$$\mathrm{pH}_0 = \overline{\mathrm{pH}} + \frac{1}{\ln(10)} \frac{\mathrm{e}}{k_\mathrm{b} T} \left(\psi_0 - \overline{\psi}\right) \tag{138}$$

Finally, the presented equation system Eq. (131) – Eq. (138) needs to be solved iteratively to obtain a pH that meets the electroneutrality condition given by:

$$0 = \sum_i \sum_j z_{i,j} \bar{c}_{i,j}(\overline{pH}) \, exp\left(z_{i,j} \frac{e\bar{\psi}}{k_\mathrm{b} T}\right) \tag{139}$$

A more detailed description of the approach can be found in previously published work [58,119].

5.2.4 Filtration models

The downstream process described in Sec. 5.2.1 consists of multiple filtration steps including sterile filtration, depth filtration (Unit III), virus filtration (Unit IX), and tangential flow filtration (Unit X). Sterile filtration can normally be considered non-critical in process development and is not addressed in this study.

5.2.4.1 Depth filtration

Depth filtration is used for clarification and impurity removal subsequent to virus inactivation. The material is composed of cellulose or polypropylene fibers and a filter aid (e.g. diatomaceous earth). In contrast to other filtration technologies, retention occurs through the entire depth of the filter pore volume due to size and surface interactions [31,32]. However, it was assumed that blocking can be approximated by simple blocking mechanisms.

For filter blocking mechanism, previous work has shown that there can be a transition in fouling behavior during filtration [30,126–128]. In this study, the depth filtration was simulated using a combined-pore blockage model introduced by Ho et al. [48]. The model provides a smooth transition from pore blockage to cake filtration. Under the assumption of a uniform resistance of the protein layer over the fouled surface of the membrane, the filtrate flow Q [$m^3 s^{-1}$] is given by:

$$\begin{aligned} Q &= Q_\mathrm{open} + Q_\mathrm{blocked} \\ &= Q_0 \left(\exp\left(-\frac{\alpha \Delta P C_\mathrm{b}}{\mu_\mathrm{b} R_\mathrm{m}} t\right) \right. \\ &\quad \left. + \frac{R_\mathrm{m}}{R_\mathrm{m} + R_\mathrm{p}} \left(1 - \exp\left(-\frac{\alpha \Delta P C_\mathrm{b}}{\mu_\mathrm{b} R_\mathrm{m}} t\right)\right)\right) \end{aligned} \tag{140}$$

where Q_open [$m^3 s^{-1}$] is the flow through open pores and Q_blocked [$m^3 s^{-1}$] the flow through blocked pores which relates to cake filtration. The initial volumetric

flowrate is represented by Q_0 [m³s⁻¹], the transmembrane pressure by ΔP [Pa], the solution viscosity by μ_b [Pas], and the bulk protein concentration by C_b [gL⁻¹]. The pore blockage parameter α [m²kg⁻¹] is equal to the membrane area blocked per unit mass of protein and needs to be determined by fitting the model to experimental data. The resistance of the clean membrane can be determined during equilibration and is represented by R_m [m⁻¹], whereas the resistance of a growing deposit is given by:

$$R_p = (R_m + R_p) = \sqrt{1 + \frac{2f'R'\Delta P C_b}{\mu_b (R_m + R_{p0})^2} t} - R_m \tag{141}$$

In Eq. (141) the fraction of protein that contributes to deposit growth f' [-] and the specific protein layer resistance R' [mkg⁻¹] are combined to the fitting parameter $f'R'$ [mkg⁻¹]. The third and last parameter that needs to be determined is the resistance of a single protein aggregate R_{p0} [m⁻¹].

5.2.4.2 Virus filtration

Virus filters are used for size-based viral clearance and can be performed in constant flow or constant pressure mode [30,129]. Flux decline has been analyzed in various studies [129–131]. However, in this study due to negligible fouling effects, the following Darcy relation:

$$Q = L_p A_m \frac{\Delta P}{\mu_b} \tag{142}$$

was sufficient to describe the filtrate flow. The membrane hydraulic permeability is given by L_p [m] and the membrane area by A_m [m²]. The virus clearance is ensured in separate virus clearance studies and not in the scope of this study.

5.2.4.3 Tangential flow filtration

5.2.4.3.1 System description

The UF/DF system can be considered a perfectly mixed stirred tank reactor of volume V [L] which includes the reservoir and dead volume. A system of ordinary differential equations (ODE) was used to describe the concentration and volume within the system. The volume is described by:

$$\frac{dV(t)}{dt} = F_{in} + F_{buffer} - F_{permeate} \tag{143}$$

where F_{in} [Ls⁻¹] represents the protein solution inflow, F_{buffer} [Ls⁻¹] the buffer inflow, and $F_{permeate}$ [Ls⁻¹] the permeate flow. For the protein concentration given by:

$$\frac{dc_{\mathrm{b}}(t)}{dt} = \frac{(F_{\mathrm{in}}c_{\mathrm{b,in}} - \frac{dV(t)}{dt}c_{\mathrm{b}}(t))}{V} \tag{144}$$

a fully retentive membrane is assumed. For the concentration of a salt ion component i the concentration in the system is given by:

$$\frac{dc_{\mathrm{s},i}(t)}{dt} = \frac{(F_{\mathrm{in}}c_{\mathrm{s},i,\mathrm{in}} + F_{\mathrm{buffer}}c_{\mathrm{s},i,\mathrm{buffer}} - F_{\mathrm{permeate}}c_{\mathrm{s},i,\mathrm{permeate}} - \frac{dV(t)}{dt}c_{\mathrm{s},i}(t))}{V} \tag{145}$$

where $c_{\mathrm{s},i,\mathrm{buffer}}$ [molm^{-3}] represents the diafiltration buffer and $c_{\mathrm{s},i,\mathrm{permeate}}$ [molm^{-3}] the ion concentration in the permeate.

5.2.4.3.2 Donnan model

Due to a charged protein retained by a semipermeable membrane used in UF/DF processes, an electrical potential difference between retentate and permeate may occur, especially at high protein concentrations. This difference can lead to undesirable variations in the ion composition and pH of the final pool, known as the Donnan effect. It was assumed, that the electrostatic equilibrium is reached immediately. Therefore, the Donnan effect was included by the permeate concentration by:

$$c_{\mathrm{s},i,\mathrm{permeate}} = \frac{c_{\mathrm{s},i}}{(1-\Theta)\exp\left(-z_{i,j}\frac{e\bar{\psi}}{k_{\mathrm{b}}T}\right)} \tag{146}$$

where the denominator denotes for the Gibbs-Donnan coefficient [58]. The same WS cell approach as described in Section 5.2.3 was used to solve for the electric potential. In contrast to the adjustment model in Section 5.2.3, the first boundary condition is replaced by:

$$\frac{\partial\psi}{\partial r}(r = R_{\mathrm{WS}}) = 0 \tag{147}$$

in accordance with Gauss' law. The volume exclusion effect due to the spherical protein in Eq. (96) is considered by the cell volume given by:

$$\Theta = \frac{4}{3}\pi a^3 c_{\mathrm{b}} N_{\mathrm{A}} \tag{148}$$

5.2.4.3.3 Permeate flow model

The concentration during ultrafiltration can lead to a strong decline of F_{permeate}. This flux decline can be described by a resistance in series model. The

resistance in series model applied in this study for a membrane of area A_m [m²], length L [m], and $x \in$ [0,L] is given by:

$$F_\mathrm{permeate} = M_\mathrm{n} A_\mathrm{m} 10^{-3} \left(\frac{J_\mathrm{lim} x}{L} + \frac{J_\mathrm{lim}^2 R^*}{\frac{L_\mathrm{p}}{\eta_0} \Delta P(x)} \log\left(\frac{J_\mathrm{lim} R^* + J_0 - \frac{L_\mathrm{p}}{\eta_0} \Delta P(x)}{J_\mathrm{lim} R^* + J_0} \right) \right) \tag{149}$$

where M_n [-] represents the number of membrane modules, η_0 the dynamic viscosity of water [Pas], and R^* [-] represents a resistance fitting parameter. Eq. (104) takes into account the flow limitation due to concentration polarization and membrane resistance. The flow limitation due to concentration polarization is given by:

$$J_\mathrm{lim} = k_0 \left(\frac{\eta_\mathrm{b}}{\eta_0} \right)^{\frac{1}{3}} \int_{C_\mathrm{b}}^{C_\mathrm{w}} \left(\frac{M_\mathrm{p}}{RT} \right) \left(\frac{\eta_0}{\eta} \right) \left(\frac{d\Pi}{dC} \right) \frac{dC}{C} \tag{150}$$

where C_w [gL^{-1}] is the concentration at the membrane wall, C_b [gL^{-1}] the protein concentration in the bulk, M_p [gmol^{-1}] is the proteins' molar concentration, Π [Pas] is the osmotic pressure, and the fitting parameter k_0 [ms^{-1}] represents the mass transfer coefficient.

The filtrate flow at the entrance of the membrane is given by:

$$J_0 = \frac{L_\mathrm{p}}{\eta_0} \left(P_\mathrm{feed} - P_\mathrm{permeate} - \Delta\Pi \right) \tag{151}$$

where P_feed [Pa] is the feed pressure and P_permeate [Pa] the permeate pressure.

The pressure drop in the feed channel required for Eq. (104) can be described by a Darcy Forchheimer approach:

$$\Delta P(x) = \frac{x}{10^3 A_\mathrm{cs}} \left(\frac{\eta_\mathrm{b}}{k_\mathrm{p}} \left(F_\mathrm{feed} - a_\mathrm{p} F_\mathrm{permeate} \right) + \frac{\rho}{10^3 k_\mathrm{l} A_\mathrm{cs}} \left(F_\mathrm{feed} - a_\mathrm{p} F_\mathrm{permeate} \right)^2 \right) \tag{152}$$

where ρ [kgm^{-3}] represents the solution density, k_p [m²] the Forchheimer permeability coefficient, A_cs [m²] the cross-sectional area, and k_l [m] the additional loss coefficient. The fitting parameter a_p [-] accounts for the membrane specific influence of the permeate flow on the pressure drop.

The viscosity was included by a Mooney equation Eq. (106) which was first introduced by Ross and Minton [107]:

$$\frac{\eta}{\eta_0} = \exp\left(\frac{bC_\mathrm{b}}{1-\left(\frac{C_\mathrm{b}}{C_\mathrm{max}}\right)}\right) \tag{153}$$

where the b [-] and C_max [gL^{-1}] are fitting parameter. The osmotic pressure was included as commonly applied with three virial coefficients:

$$\Pi = RT(B_1C_\mathrm{b} + B_2C_\mathrm{b}^2 + B_3C_\mathrm{b}^3) \tag{154}$$

5.2.4.4 Diafiltration model

The diafiltration phase was approximated by averaging the model outputs of the UF1 and UF2 model based on the mixture of the buffer condition x_DF [-]. For the permeate flow this leads to:

$$F_\mathrm{permeate,DF} = (1-x_\mathrm{DF})F_\mathrm{permeate,UF1} + x_\mathrm{DF}F_\mathrm{permeate,UF2} \tag{155}$$

and similarly for the pressure drop to:

$$\Delta P_\mathrm{DF} = (1-x_\mathrm{DF})\Delta P_\mathrm{UF1} + x_\mathrm{DF}\Delta P_\mathrm{UF2} \tag{156}$$

A more detailed description of the UF/DF model can be found in previous publications [132].

5.3 Materials and methods

5.3.1 Protein and buffers

The biopharmaceutical protein (Boehringer Ingelheim Pharma GmbH &Co. KG, Biberach an der Riß, Germany) used in this study is a Fab fragment and has a molecular weight of approximately 50 kDa. All chemicals in this study were from Merck Millipore (Burlington, USA).

5.3.2 Resins, filters, and systems

The capture chromatography step was performed with the KappaSelect (Cytivia, Uppsala, Sweden) resin. The resin used for AEX was Q Sepharose FF (Cytiva) and for CEX Poros 50 HS (Thermo Fisher Scientific, Waltham, Massachusetts, USA). Depth filtration was performed using a Zeta Plus™ 60ZB05 (3M, Saint Paul, Minnesota, USA) combined with a Zeta Plus™ 30ZB05 (3M) as prefilter. The virus filter used was a Planova 20N (Asahi Kasai, Tokyo, Japan) and the UF/DF membrane an Ultracel Pellicon® 3 C-Screen cassette (Merck Millipore, Burlington, USA). The lab-scale chromatography and depth filtration experiments were conducted on an Äkta™ avant 25 system (Cytiva). Lab-scale virus filtration was performed on an inhouse controlled filtration system and UF/DF experiments on the ÄKTAcrossflow (Cytiva).

5.3.3 Column experiments

The capture column used for calibration and validation experiments listed in Table 10 was of 15 cm length and 1 cm diameter. A linear pH gradient elution was achieved with a citrate buffer mixture. The load material for experiment Capture_C5 was buffer exchanged in the first wash buffer to enable a UV signal during the breakthrough curve (BTC). Prior to isotherm parameter estimation, a system characterization was performed. Therefore, column and particle porosities, axial dispersion and effective mass transfer coefficients were estimated via non-binding protein pulses, salt and dextran pulses at varying flowrates (86-300 cm/h). The linear velocity u [mms^{-1}] dependency of the axial dispersion is described by the following quadratic approximation:

$$D_{\mathrm{AX}}(u) = D_{\mathrm{AX},0} + D_{\mathrm{AX},1}u + D_{\mathrm{AX},2}u^2 \tag{157}$$

The isotherm parameters were estimated based on the experiments Capture_C1-5. The experiments used for AEX and CEX chromatography modeling can be found in Rischawy et al. [119]. The model parameters can be found in the Appendix.

Table 12: Overview of calibration and validation experiments for the capture chromatography model.

Experiment	Elution buffer	Elution pH	Loading density [g/L]	Flow [cm/h]
Capture_C1	25 mM citrate	Gradient pH 6.0 – 2.35 in 10 CV	10	196
Capture_C2-4	25 mM citrate	Gradient pH 6.0 – 2.35 (5, 10, 20 CV)	1	196
Capture_C5	50 mM elution buffer component	2.5	BTC	196
Capture_V1	50 mM elution buffer component	2.5	13.5	196

5.3.4 Filtration experiments

Depth filtration experiment conditions are listed in Table 13. The control mode was either the transmembrane pressure or the filtrate flow. The filter area for all lab-scale experiments was 3.8 cm². Due to the strong pH dependency of the neutralization turbidity, a pH extension to the model was introduced by fitting a second order polynomial to parameter estimates of $f'R'$ at three pH values. For pressure-controlled experiments, the pressure drop measurement was taken as model input. For the DF_V5* constant flow experiment, the pressure increase was simulated by iteratively determining the pressure to keep the filtrate flow constant over time.

Table 13: Model calibration and validation experiment conditions for depth filtration. The listed experiments were pressure controlled, except for DF_V5 which was controlled by flow.*

Experiment	Protein concentration [g/L]	pH [-]	Controlled ΔP [bar] or flow* [L/min/m²]	Load [L/m²]
DF_C1	8.7	6.0	1.5	275
DF_C2	6.5	7.0	1.5	275
DF_C3	8.7	8.0	1.5	275
DF_V1	6.5	6.0	1.0	550
DF_V2	6.5	8.0	2.0	550
DF_V3	6.5	6.0	1.0	550
DF_V4	6.5	8.0	2.0	550
DF_V5*	6.5	7.0	46*	550

The virus filtration experiment was performed with a filter area of 0.12 m². For a summary of all UF/DF experiments, we refer to a previous publication [132]. In addition, the Donnan effect model was embedded in the pressure-flow

UF/DF model as described in Section 5.2.4.3. The parameters required for the electrostatic interaction used in the Donnan and adjustment model are listed in Table 2 and Table 15. The ion analytics during UF/DF was performed by an inhouse routine. The chloride ion concentration was analyzed by a LCK311 photometric assay (Hach Company, Loveland, CO, USA) according to the manufacturer's instructions. Acetate concentration in the supernatant of precipitated protein solution was analyzed by a reverse phase 5 µm 4 × 250 mm Acclaim OA column (Thermo Fisher Scientific) with 100 mM Na_2SO_4 pH 2.7 as mobile phase and a flowrate of 0.6 mL/min at 30°C.

Table 14: pH adjustment model parameters.

Parameter	Value
Stern capacitance C_S [Fm^{-2}] [58]	0.2
Protein radius a [nm]	2.35
Relative permittivity of water ε [-]	78.3
Molecular weight M_P [kDa]	~ 50
Temperature T [K]	298.15

Table 15: Average residual pK values of side chains [80].

Residual	pK_k	ζ_k
N-terminal	7.5	1
Glutamic acid	4.4	0
Aspartic acid	4.0	0
Tyrosine	9.6	0
Lysine	10.4	1
Arginine	12.0	1
Histidine	6.3	1

5.3.5 Software

All chromatography models were solved using the Chromatography Analysis and Design Toolkit (CADET) (Research Center Jülich, Germany)[133]. The default solver parameters provided by Cadet were used. In addition, the column discretization was set to at least 60 finite elements, the relative tolerance and absolute tolerance was set to 1e-6, with an initial integrator step size of 0.01 seconds. The mechanistic process model as well as filtration and adjustment models were all solved and plotted in the MATLAB 2019b (The Mathworks Inc., Natick, MA, USA) environment. The applied solvers are listed in the supplementary Table 16. For parameter estimations, a least square minimization problem with the MATLAB nonlinear programming solver fmincon was solved. The solver converged with default solver parameters.

Table 16 Overview of CMPM models, parameters, solver, and software. The process output parameters of one unit operation are the inputs of the following unit operation.

Unit	Model	Software/Solver: Model	Para-meters estimated on process data	Pre-determined parameters	Input process parameter	Output process parameter
I	Capture	• Cadet: Langmuir based model • Matlab: Cadet interface, result evaluation	k_{kin} q_{max} k_{eq} $\mathrm{p}K_{\mathrm{a}}'$ $\mathrm{p}K_{\mathrm{a}}''$	D_{ax} k_{eff} ε_{v} ε_{P}	$c_{\mathrm{s},i}$ $c_{\mathrm{b},i}$ V pH	$c_{\mathrm{s},i}$ $c_{\mathrm{b},i}$ V pH
II, IV, VI, VIII	Adjust-ment	• Matlab bvp5c: Poisson Boltzmann • Matlab Bisection method: Electroneutrality condition	–	a		
III	Depth filtratio n	• Matlab: Combined pore blockage model	$f'R'(pH)$ R_{p0} A L_{p}	–		
V, VII	AEX, CEX	• Cadet: CPA	k_{kin}^{*} Δ	a $A_{S,0}$		

		• Matlab: Cadet interface, result evaluation	A_s Z_{lat} $Z(pH_{ref})$	Λ_{IEX} D_{ax} k_{eff} ε_v ε_P		
IX	Virus filtration	• Matlab: Darcy relation model	–	L_p		
X	UF/DF	• Matlab ODE15s: UF/DF tank model	–	–	$c_{s,i}$ $c_{b,i}$ V $F_{permeate}$ $c_{s,i,permeate}$	$c_{s,i}$ $c_{b,i}$ V pH
		• Matlab: Permeate flow, Pressure drop	k_0 a_p k_p k_l	L_p η Π	$c_{b,i}$	$F_{permeate}$
		• Matlab bvp5c & bisection method: Donnan model	–	–	pH $c_{s,i}$ $c_{b,i}$	$c_{s,i,permeate}$

5.4 Results and discussion

5.4.1 Capture chromatography model

The capture chromatography step was calibrated based on pH gradients and a breakthrough curve under the conditions listed in Table 10. The non-binding protein pulses performed under low pH condition revealed a size exclusion effect, which was approximated by a reduced particle porosity for the protein compared to salt [45]. The kinetic parameter was fixed to a high value of 1e6 s, which assumes an immediate equilibrium state. Furthermore, although the pK_a'' for the ligand and target protein (pK_a') have physical relevance, they are structurally indistinguishable. Thus, a single effective pK_a^* was assumed without observing drawbacks in model performance. As shown in Figure 3, the

elution behavior of the size variants proved to be indifferent, so that a common set of parameters was found to be sufficient to describe the elution profile. In Figure 29 the overlay of model to measurement data of all experiments listed in Table 10 is shown. The binding model was able to describe the elution chromatogram of varying loading and pH conditions and predicted a step elution. In the following the estimated parameters listed in Table 17 are discussed.

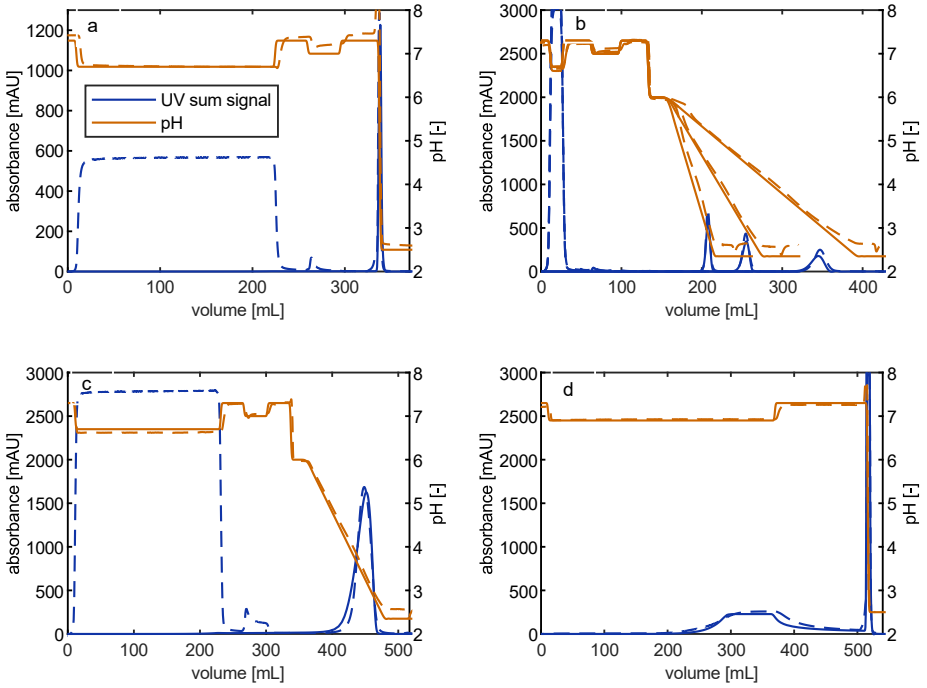

Figure 29: Capture model experiments. The measurement data is presented in dashed lines and the simulation in solid lines. The conditions of experiments are listed in Table 10: Capture_V1 (a), Capture_C2-4 (b), Capture_C1 (c), Capture_C5 (d). Calibration experiments have the suffix "_C" and the validation experiment "_V". The UV measurement signal of the loading phase is caused by cell media additives which was not included in the model.

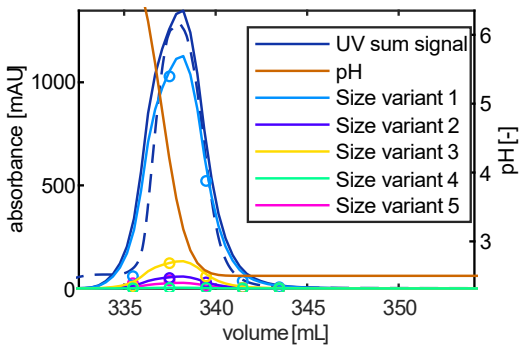

Figure 30: Zoom to Capture_V1 (Figure 29 (a)) pH step elution used for model validation. The measurement data of size variants is represented by scatter points and reveal co-elution behavior of variants.

In the following the estimated model parameters are discussed. The resin manufacturer provides a ligand density estimate of the KappaSelect resin slurry of approximately 5 mg/mL and a molecular weight of the ligand of approximately 13 kDa [134]. This can be calculated to a ligand density of 0.385 mol/m³ resin or a theoretical q_{max} based on the estimated resin backbone volume of 7.54 mol/m³. The estimated q_{max} of 6.94 mol/m³ was approximately in the same order of magnitude which shows that the value is realistic, assuming that the ligand number is limiting for protein binding. However, due to the high influence of minor changes in the parameter an inverse parameter was inevitable. Furthermore, the amino acids involved in the ligand to Fab interaction of KappaSelect are not completely understood based on literature. For affinity chromatography with Protein A the ligand interaction is known to depend on histidine residue interaction [135]. However, the pK_a of histidine can be a function of the local environment leading to pK_a shifts [136]. Due to pK_a shifts and the general lack of understanding on a molecular level of the binding interaction with the KappaSelect ligand, the pK_a'' of the ligand interacting amino acids and the pK_a' of the protein interacting amino acids were lumped to an effective pK_a^*. In addition, the two parameters are structurally indistinguishable. The single effective pK_a^* could be assumed without observing drawbacks in model performance. The final model was tested on the step elution experiment Capture_V1 in Figure 29 and showed a good agreement with the measurement data.

Table 17: Chromatography column parameters for Capture, AEX, and CEX [13].

Parameter	Capture	AEX [119]	CEX [119]
Column volume V_C [mL]	11.78	12.10	10.00
Column length L_C [cm]	15.00	15.40	10.00
Void fraction ε_v [-]	0.35	0.34	0.40
Particle porosity ε_p [-]	0.91	0.78	0.54
Bead radius r_p [µm]	37.5	45	25
Protein particle porosity $\varepsilon_{p,j}$ [-]	0.50	0.78	0.41
Axial dispersion coefficient $D_{AX,0}$ [mm²s^{-1}]	-0.13	-0.14	0
Axial dispersion coefficient $D_{AX,1}$ [mm]	0.35	0.25	0.20
Axial dispersion coefficient $D_{AX,2}$ [s]	0	0	0.45
Effective mass transfer coefficient $k_{eff,non-protein}$ [mms^{-1}]	1.25e-2	1.50e-2	0.83e-2
Effective mass transfer coefficient $k_{eff,protein}$ [mms^{-1}]	0.90e-3	0.52e-2	0.83e-2
Maximum binding capacity q_{max} [molm^{-3}]	6.94	-	-
Ionic capacity Λ_{IEX} [M]	-	1.50	0.31
Total available adsorber surface $A_{S,0}$ [m²m^{-3}]	-	4.80e8	1.40e8
Specific adsorber surface A_S [m^{-1}]	-	3.60e8	6.25e7
Ligand density $\Gamma_L = \Lambda_{IEX} A_{S,0}^{-1}$ [molm^{-2}]	-	3.12e-6	2.19e-6
Equilibrium coefficient $k_{eq,i}$ [m^{3}mol^{-1}]	3.13e3	-	-
Effective acidic dissociation constant pK_a^* [-]	4.50	-	-
Kinetic $k_{kin,i}$ [s]	1e6	-	-

5.4.2 Virus inactivation

Virus clearance is ensured in separate virus clearance studies and not in the scope of this study. However, neutralization after virus inactivation can lead to increasing turbidity of the protein solution [16] which can affect the depth filtration performance regarding the flux decline as discussed in Sec. 5.4.3.1. Figure 31 shows the pH course when titrating 6.71 g/L protein solution with 1 M Tris. The turbidity peaked at pH 5.5 - 7.0 (data not shown) which could be

related to aggregation and precipitation of HCPs close to their typical pI range of 4.5 - 7.5 [137]. Above the typical pI, HCPs start being polar and solubilized again resulting in reduced turbidity measures. The observed turbidity course was in very good agreement with data presented by Chollangi et al. [137]. The load pool ion analytic resulted in an ion concentration of 31 mM sodium ions, 42 mM chloride ions, 37.8 mM elution buffer component and 2 mM phosphate carryover ions. The resulting titration curve was predicted by the adjustment model based on ions, protein structural information, and protein concentration.

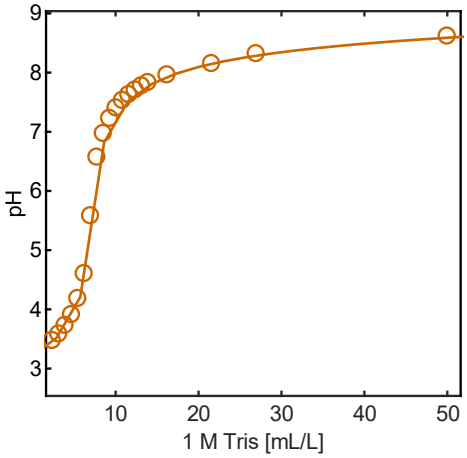

Figure 31: Neutralization of virus inactivation pool by titration with 1 M Tris solution. Measurements are presented as scatter points and the adjustment model prediction by a solid line.

5.4.3 Filtration

5.4.3.1 Depth filtration

As discussed in section 5.4.2, the turbidity highly depends on the pH and thus potentially affect filtration behavior during depth filtration. The depth filter model was calibrated using experiments DF_C1-3 (Figure 32 a-c) at three different pH values (pH 6.0, pH 7.0, and pH 8.0) and a transmembrane pressure of 1.5 bar. The model parameters $f'R'$, R_{P0}, and α were estimated based on the single experiment DF_C2. In order to add a pH dependency, the $f'R'$ parameter was estimated on DF_C1 and DF_C3. This is consistent with the expected pH dependency of protein layer resistance R' caused by changes in intermolecular interactions [48]. Parameter estimates are listed in Table 18. The membrane resistance of 1.15e11 m varied by $\pm$ 10 % with changing membranes between runs and was therefore determined based on equilibration data for each individual run.

Table 18: Model parameter estimates for depth filtration. The $f'R'$ estimates were connected by a second order polynomial to approximate the pH dependency.

Parameter	Depth filtration model estimates
Protein resistance growth parameter $f'R'$ [mkg^{-1}]	$f'R' = (53.52 - 9.48\text{pH} + 0.36\text{pH}^2)1e10$
Resistance of a single protein aggregate R_{p0} [m^{-1}]	4.0e10
Pore blockage parameter α [m²kg^{-1}]	2.0

The predictive power of the model was tested under varying input variations regarding transmembrane pressure, protein loading, and pH as presented in Figure 32 (d-h). The simulation in Figure 32 (h) demonstrates the capability of the model to predict the pressure in a flow control experiment. In summary, the depth filtration model was shown to have extrapolation capabilities of changing pressures, protein loading, pH, and control mode. The size variances were not changed by the filtration step, except for variant 1, which was constantly reduced to approximately 11.2 % of the load proportion in lab-scale experiments.

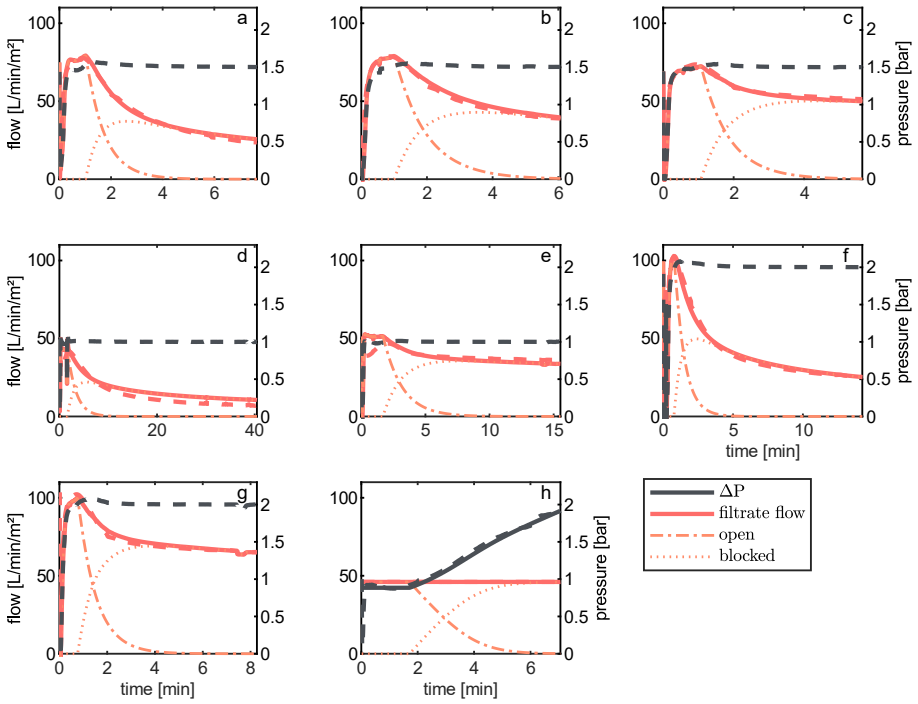

Figure 32: Depth filtration experiments used for model calibration and validation. Measurement data is presented by thick dashed lines and simulation data as solid lines. The conditions of experiments are listed in Table 13. Experiments (a-c) were used for model calibration and experiments (d-h) for model validation. Experiment (h) was performed in flow control while all other experiments are performed in pressure control mode. Thus ΔP is not an input but a simulation output, represented by a solid line. The open and blocked filtrate contributions were included as thin dashed lines for demonstration purposes.

5.4.3.2 Virus filtration

The virus filtration in this study was performed as dead-end filtration and showed no time dependent filtrate flow decline caused by a blocking mechanism. Therefore, the model presented in section 5.2.4.2 was found to be sufficient to describe the experimental data by estimating the membrane hydraulic permeability of 1.987e-13 m as presented in Figure 33. However, for other proteins and membranes this simplification might not hold due to possible membrane blocking [129–131].

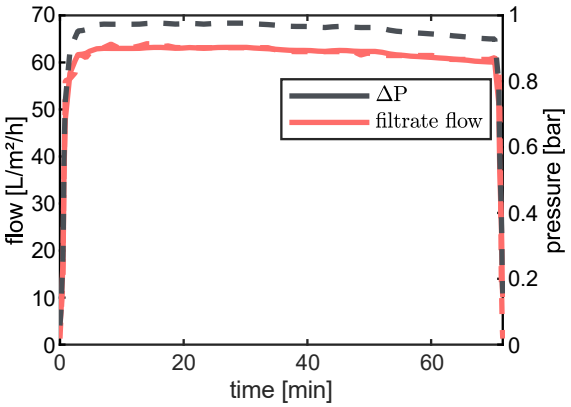

Figure 33: Experiment used for estimation of the virus permeability. Measurement data is represented in dashed lines and the simulation in solid lines. The filtration was found to be purely dominated by filter permeability and revealed no blocking mechanism.

5.4.3.3 Ultrafiltration/Diafiltration

The UF/DF model used in this study is presented in detail in previous work [132]. In the present study, model complexity was further increased by adding the Donnan effect [58]. The model prediction is presented in Figure 34. The model for the permeate flow and Donnan model throughout all UF/DF phases was in good alignment with the measurement data. The model was calibrated on UF experiments and viscosity data. Combining the results of the UF1 and UF2 models based on buffer exchange allowed an approximation of the flow and pressure behavior during DF phase. Moreover, the Donnan model predicts the pH shift at UF2 and acetate buffer concentration of acetate without the need to estimate any model parameters.

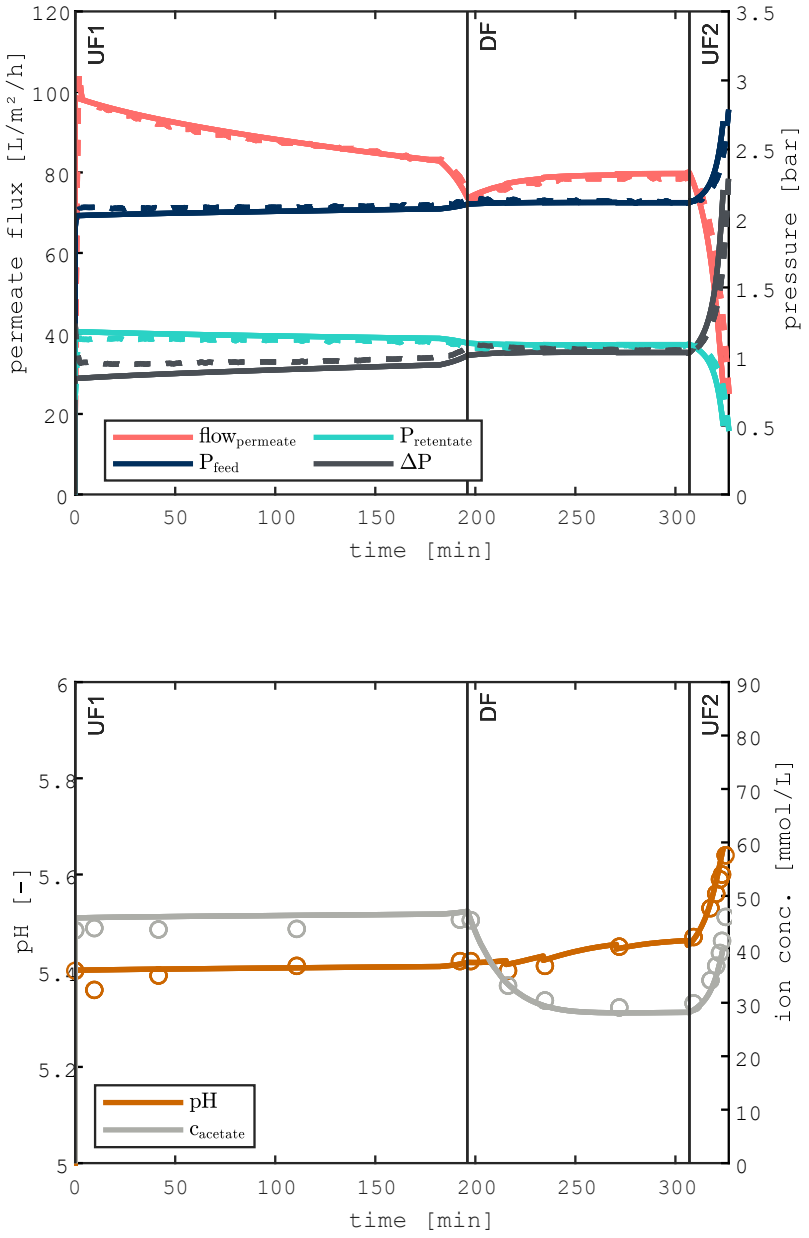

Figure 34: Model prediction of UF/DF process in lab scale. The upper figure shows the model result for filtrate and pressure. The bottom figure shows the prediction of the Donnan model for ion concentration and pH.

5.4.4 Mechanistic process model

The presented models were connected to the CMPM and applied to manufacturing conditions. A connected mechanistic process model uses the output of one unit as input for the following unit. In this study, process parameters transferred between models were protein concentration, volume, size variant composition, ion concentration, and pH. To accomplish this, assumptions had to be made to define the downstream starting conditions,

which is discussed below. First, for the capture step the ion concentration data of the manufacturing runs were not available and were therefore approximated to be the same as the elution buffer concentration for elution buffer component. The concentrations of additional sodium, chloride, and phosphate were adopted from the small-scale experiment measurements. The pH measurements of the capture pool were used to approximate the ion composition for the input of the virus inactivation (Unit II) model. Dilution and changes in ion concentration caused by rinse volumes, e.g., during filtration washes, were included by mass balancing. In addition, the first data for size variants were available for the capture pool. Therefore, the starting material was assumed to match the given composition of the capture elution pool measurements. Except for the chromatography column dimension, all column parameters of each chromatography step were considered constant during scale-up.

With the assumptions made, the models work together as a mechanistic process model and were tested using online and offline manufacturing data. The prediction of the mechanistic model is presented in Figure 35 and demonstrates the predictivity of the model for runs of strongly deviating titers. The scale-up prediction of the model underlines the scale independence of the CMPM and estimated parameters. However, minor assumptions were included for modeling the large-scale system. First, the ΔP during depth filtration was reduced by a pressure loss caused by the filter module design itself which is a well-known effect in manufacturing. This pressure drop was estimated based on filter equilibration data. The filtration was therefore not limited by the pressure alone as in the lab-scale experiment, but by the pressure loss of the filter module. In this context, scale-effects could arise with change in the number of capsules [138] which was not the case in this study. In addition, the R_M membrane resistance parameter was increased by 20 % to meet the filtration start. With the assumptions made, the model described the filtrate flow trend of the manufacturing depth filtration. For the virus filtration a constant pressure loss was included based on equilibration data. For AEX a preceding stirred tank reactor (STR) was included to simulate back-mixing in the bubble trap. The UF/DF model membrane permeability estimated on equilibration data was reduced to meet the permeate flow at the start of UF1. Furthermore, the pressure drop parameter k_P was decreased to account for the underprediction of the pressure drop along the membrane. This is discussed in more detail in a previous publication [132]. In conclusion, the discussed assumptions demonstrate that starting conditions of filtration units were difficult to predict and filtration could not be linearly scaled. However, the pressure losses of the filters might be systematic and therefore transferable to processes of other biologics. This needs to be investigated in future studies. The

chromatography and adjustment step model prediction were in good agreement with the manufacturing scale online data.

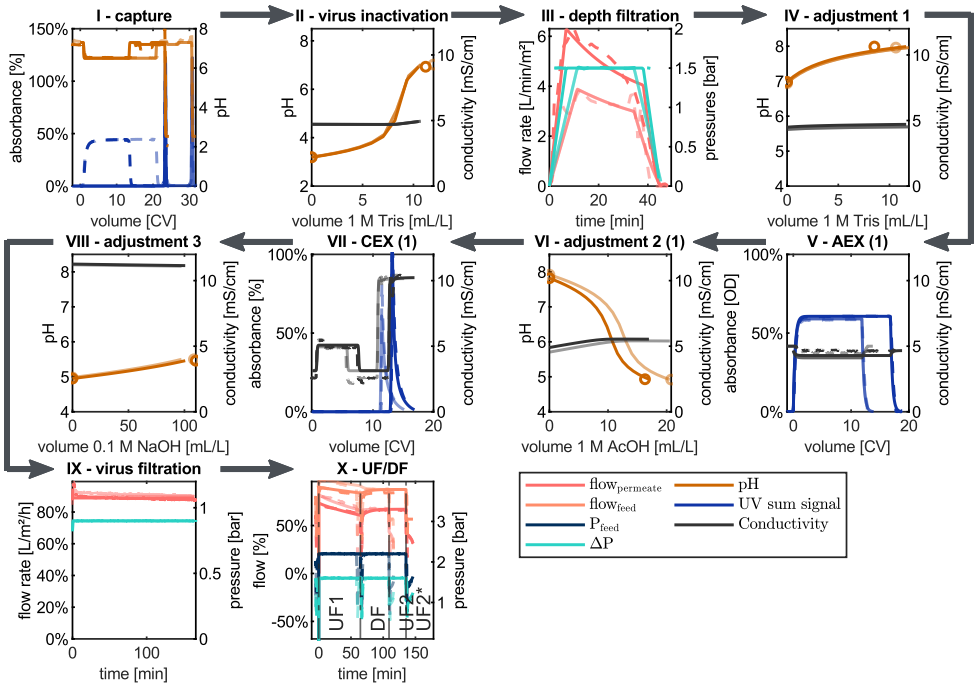

Figure 35: Mechanistic process model online data prediction of two manufacturing downstream processes. The model simulation is represented by solid lines and the online measurement data by dashed lines. The offline data for pH is represented by scatter points. For illustration purposes, the y axes are chosen based on the main control and output parameter of the unit. Hence, for filtration pressure and flow, for adjustments pH and conductivity, for IEX conductivity and UV absorbance, and for capture chromatography pH and UV absorbance. The run of high titer is represented in solid colors and the low titer run is represented in transparent colors. Due to confidentiality, the y axes were scaled.

Regarding the model depth chosen in this study. Each model presented is at the forefront of mechanistic modeling in the biopharmaceutical downstream process. The laboratory and scale up to manufacturing scale data for model discrimination were intentionally challenging. Reducing the model depth is expected to cause the model to not respond like the real counterpart when process inputs change. If the model is not able to describe, for example, a chromatography breakthrough curve, the question arises whether and when the extrapolation results are trustworthy. On the other hand, due to the timeliness of the selected models, an increase in model depth is not readily possible, but is part of further studies. Model extensions, as applied to hybrid modeling, can be a helpful option to bridge model limitations. However, the focus of this study was not on comparing models but can be an interesting topic for future studies.

5.4.5 Manufacturing variability

The model presented in the previous section demonstrated the prediction of data for an entire downstream process sequence at manufacturing scale. An application of such model could be a cross-unit *in silico* study at manufacturing scale to investigate the robustness of the target condition and control strategy. This can be particularly valuable when robustness despite upstream variability needs to be ensured which is usually difficult to be addressed experimentally with a limited number of cell culture batches. For such *in silico* studies the initial starting conditions and process parameter variabilities need to be known or approximated based on historical data. To demonstrate that the CMPM responds like the real manufacturing process and can be applied to investigate process robustness, the model was tested on the real initial measured manufacturing variability of 23 manufacturing runs. The output variability of the model is compared to measured output variability distribution in form of boxplots presented in Figure 36.

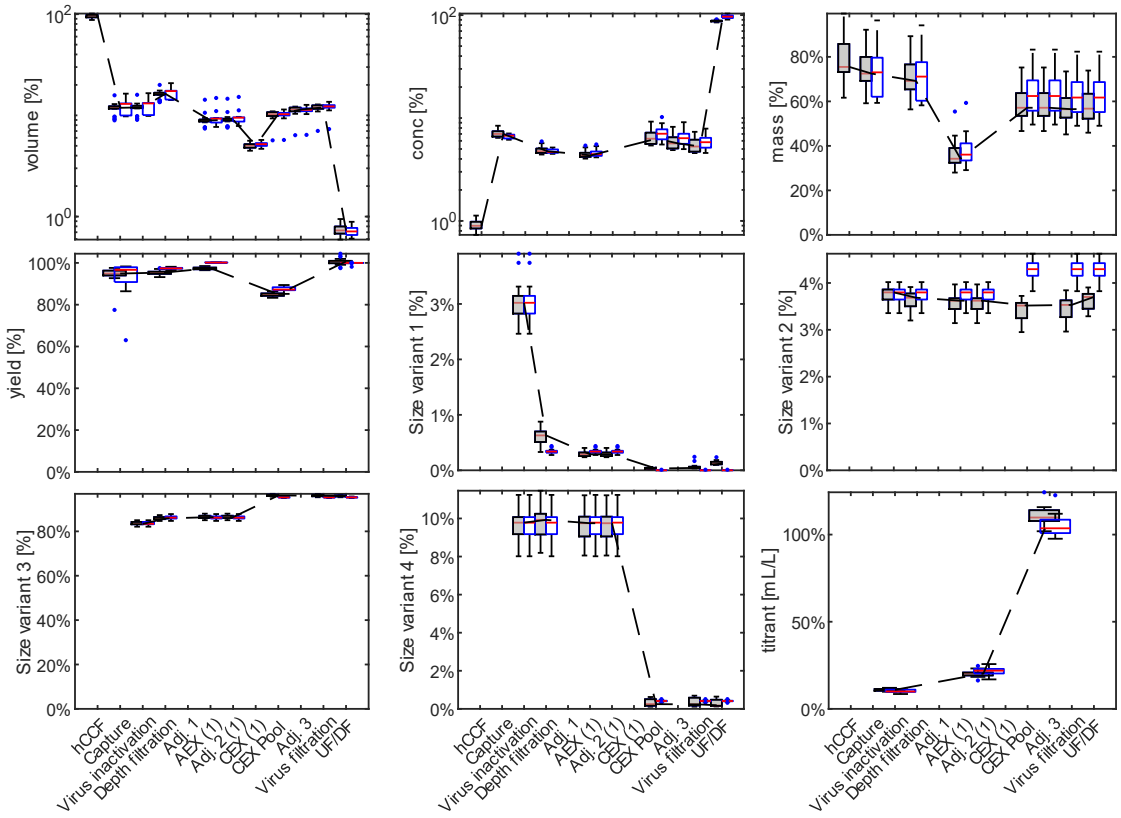

Figure 36: Comparison of model vs. manufacturing variability: Grey boxplots represent the measurement variability of 23 manufacturing runs and white boxplots represent the model output. The medians are connected by a dashed line. In this figure only first cycles of chromatography units were included for the sake of clarity. Measured buffer variability regarding pH and ion composition was included. Due to confidentiality, the y axes were scaled to the maximum value.

The results demonstrate that the lab-scale calibrated model can predict the range and median of volume, concentration, yield, titrant volume, and size variants across unit operations solely based on the initial input variability. Minor deviations of model to measurement can be caused by unknown sampling volumes between units, measurement errors, and model assumptions. Such systematic errors could have been easily adjusted based on an initial manufacturing run. However, this was not performed on purpose in this study to demonstrate the model capability prior to deviation correction. Buffer pH and concentration variability were included based on measurement data. When the CMPM is applied to novel processes, the historical pH variability range or normal operating ranges might be used to approximate the potential process response throughout the downstream sequence. As shown in Figure 36, the model prediction of the titrant volume variability was in good agreement with the measurement data. The primary influence of this variability was found to be the input pH variability. A minor offset in titrant volume was observed which could be the result of model limitations and requires further investigation. In summary, the model was found to react to input variability similarly to the real manufacturing process behavior. The lab-scale CMPM could be used to scale-up and act as a foundation for further model improvements and scale investigations. Furthermore, the CMPM could lead to a paradigm shift from a unit operation-based process development towards a holistic process understanding considering the propagation of process variability through the entire biopharmaceutical downstream process.

5.5 Conclusion

In this study mechanistic models for every process unit of a downstream sequence were connected referred to as CMPM. The existing models have demonstrated their extrapolation capability in laboratory-scale validation experiments and their scalability when applied at production scale. All model equations and parameter estimations converged without issues. The presented CMPM allows for a high degree of flexibility, which is required during process development of new drug candidates. For example, when changing the CEX operation mode from step to gradient elution the holistic cause and effect of process changes can be investigated and compared. It has been further demonstrated that a major part of the manufacturing process variability can be described by the model based on the measured input variability. Therefore, a good theoretical estimate on process performance might be made based on historical normal operating ranges for concentration, pH, flow rates, and material attributes. Application of the model to production data shows the potential for better understanding scale related topics through mechanistic

modeling and the use in process transfer issues. In general, development experiments will remain indispensable. In the future, however, they may only serve to confirm the optimal and robust process conditions and not to find them in first place. Of course, the presented CMPM has its limitations - here the authors appeal strongly to the community to consider the model as a starting point for further developments.

6 Discussion and conclusion

The biopharmaceutical industry aims to reduce the time to market which requires a lean process development. However, the drug safety is of highest priority and must be ensured. Due to limited fundamental process knowledge, extensive experimentation is required for each new drug candidate's process to eliminate any risk of quality deviations. The development and implementation of new technologies could lower the experimentation effort required without the need to accept any additional risks.

This dissertation presents a mechanistic model, referred to as CMPM, that connects mechanistic models for every process unit of a downstream sequence. The results contribute to the applicability of mechanistic models in biopharmaceutical process development. For the very first time, it has been shown that mechanistic models can reliably describe the downstream unit operations operated at real-world conditions and, when combined, can describe an entire downstream process. A major challenge was to find models reliably reacting to input parameters like the real system, also referred to as model discrimination. Here, the strategy was to start with the simplest model and increase complexity if required. This resulted in a final set of models that are at the forefront of mechanistic process modeling. This set of models described all chromatography, filtration, and adjustment steps in the process. However, the models cannot describe every aspect of a downstream process. The advantages and limitations of mechanistic models are discussed below.

6.1 Advantages and limitations of mechanistic models

Although the model describes the main effects such as pressure/flow dependence during filtration or pH/salt dependence during chromatography, other parts remained untouched and are not easily described by mechanistic models. This includes e.g. stabilities with respect to freeze-thaw or pH instabilities, which are complex to be predicted mechanistically and are probably easier to be determined experimentally and preferably in miniaturized form. Still, homology modeling can be applied to derive general trends for the aggregation propensity of a protein based on aggregation-prone regions, which is of particular interest in early phase development to design

stable antibodies [139]. However, mechanistic process modeling is perceived as a balanced approach for downstream development, considering its complexity and applicability. When compared with more complex molecular dynamic simulations, the computational effort required is significantly high, leading to impracticality in terms of time and complexity. Pure statistical modeling, on the other hand, requires extensive experimental investigation of all interrelationships, which is both cost and time-intensive, and is not feasible for all process parameters.

Mechanistic models offer the advantage of having prior knowledge embedded in the equations, requiring limited or even no specific data to describe the process. As demonstrated in this dissertation, these models provide simulated online measurement outputs, such as chromatograms or pressure/flow diagrams, enabling direct comparison with process data. Statistical models, as the commonly used method in biopharmaceutical process development, do not offer this advantage. Nevertheless, statistical approaches have their own merits. The application of regression models to describe experimental outputs can be fitted virtually to any outcome, thereby invariably providing a result. This, however, can also be a disadvantage as it could potentially obscure theoretical or experimental errors, which may be incorporated into the evaluation unknowingly. This feature, however, can also pose a disadvantage, as potential theoretical or experimental inaccuracies may go unnoticed and inadvertently be incorporated into the assessment. To illustrate, consider a scenario where a malfunctioning blue filter in the UV cell leads to a reduction in the UV signal. The resultant effect would affect the cutting criteria and decrease the overall yield. In the absence of a theoretical chromatogram provided by a mechanistic model for comparison, such a systematic error is likely to be overlooked. Consequently, the integration of models, as outlined in the previous chapters, can be an essential as a precautionary step to identify anomalous process behavior.

However, this requires the model to be accurate and the process to be well comprehended. In this context, the pH-dependent behavior of processes in chromatography and filtration exhibits a complex nature, which this study has largely addressed via empirical correlations within an appropriate pH range. For instance, this was necessary for determining the $f'R'$ parameter in depth filtration or the pH dependency of the CPA model via a pH correlation of the protein charge. The latter was accomplished by means of low-loading linear gradient experiments at different pH values [81]. Describing the correlation by means of the sequence has been extensively studied and was found to correctly reproduce the trend [44,140]. However, the accuracy and reliability are currently not considered sufficient. Nevertheless, a combination of mechanistic

approaches and regression models for not completely understood phenomena is a common approach in industrial applications.

In terms of model errors, the total error can be described as the sum of model error, measurement error, and model parameter error. In previous studies the model parameter uncertainty was of interest [88,143]. In this study, the strategy involved challenging the models with experimental conditions and scales. The primary challenge was to describe the experiments using a model in the first place. It was often not possible to describe the process behavior for any combination of parameters. For example, the standard polarization model could not describe the TFF experiments under varying conditions and was replaced by a more complex modified polarization model (Chapter 4). Similarly, the SMA isotherm was not capable to describe the CEX experiments for any parameter combination (Chapter 3). In conclusion, the focus was set to minimize the model error. However, parameter uncertainty is of interest in future studies to further refine the estimation strategy.

Another aspect that needs to be considered is error propagation. In a concatenation of models, it could be assumed that error propagation is a problem. However, it was observed in Section 5.4.5 that the errors do not extensively propagate through the process. First, the model error compared to the measurement was not large, and second, unit operations and process control can work against the error propagation. For example, an increased volume for the same amount of protein has an identical elution peak in the CEX. Thus, a volume error would be compensated during the process sequence. A similar case, for such non-passing variability, was observed for the size variants. Size variant impurities were found to be partially strongly bound to the resin. The CEX process was robust against impurity level changes on the input, which greatly reduced the variability of the CEX. In addition, pH deviations in manufacturing were always captured in the adjustment steps by the operator. Although the error propagation was not predominant in this study, a less robust process might significantly add to the error across units.

In general, this study has initiated the journey towards a comprehensive downstream process description using mechanistic models. The effort to understand and describe the process in depth has led to a significant increase in knowledge and confidence. As different groups work on models, they improve over time, and process development that uses mechanistic models will stay current. Even if real process data could be described with mechanistic models, this in itself is valuable information. It reveals a knowledge gap or even a material or operator error. In addition, this approach encourages developers to not only focus on discrete measurements like yield and purity but also to become more sensitive to interpreting deviations in the chromatogram or the

pressure/flow curve during filtration. Having the theory ready, troubleshooting ideas can be derived in a systematic manner at both lab scale and commercial scale.

It should be emphasized that describing every aspect of downstream process of biopharmaceuticals mechanistically is a highly ambitious goal. The physical phenomena involved in filtration and chromatography are often complex and not entirely comprehensible. Nevertheless, in this work, the knowledge about the downstream process could be applied collectively and main effects in a single downstream process could be described. Since the physical process does not change fundamentally, one could assume that other downstream processes could now be described in the same way. However, this is hardly the case. The complexity can increase drastically as the process conditions change. Take the example of having a mixed mode resin in process sequence. Multiple interaction principle would require a unified description of not only ionic exchange, but also hydrophobic interaction. To date, there is no mathematical model available, which would come with the same level of precision covering the simulation of broad experimental conditions. Also, frontal chromatography might be challenging for chromatography modeling due to complex displacement effects in highly nonlinear region [141]. The complexity in terms of modeling can also depend on the process condition itself. A fully loaded column can be expected to be more difficult to describe than a low loaded column. Likewise, a process with a small operating window as it is the case in weak partitioning will make modeling more difficult due to an increased sensitivity to input changes. However, in the course of this work, another factor has been identified to be challenging. In biopharmaceutical development several analytical methods are used to ensure product quality. To be able to replace real experiments, the model must provide information about all CQAs. As shown in Figure 37, the protein solution typically is divided into different proportions depending on the analytics. In this study, the analytical methods included capillary gel electrophoresis (cGE), high-performance size exclusion chromatography (HP-SEC), and high-performance weak-cation-exchange chromatography (HP-WCX). The method to first take the HP-SEC data and from there divide the “Main” species into charge variants, as applied in previous studies, was not possible [81,88]. This was mainly because the size variant 5 with 14.8% in the cGE analysis and 9.6% in the HP-SEC analysis, accounts for a significant proportion of the CQAs. In addition, the two methods (cGE, HP-SEC) were used to analyze size variants. However, HP-SEC analyses the size variants in its native state, whereas cGE separates the protein under denaturing conditions by using sodium dodecyl sulfate (SDS). This can lead to an increased percentage of light chain and decreased aggerate levels for the

cGE analysis, as presented in Figure 37. Since the mass balance could not be reconciled, a model for each analytical method would have been necessary.

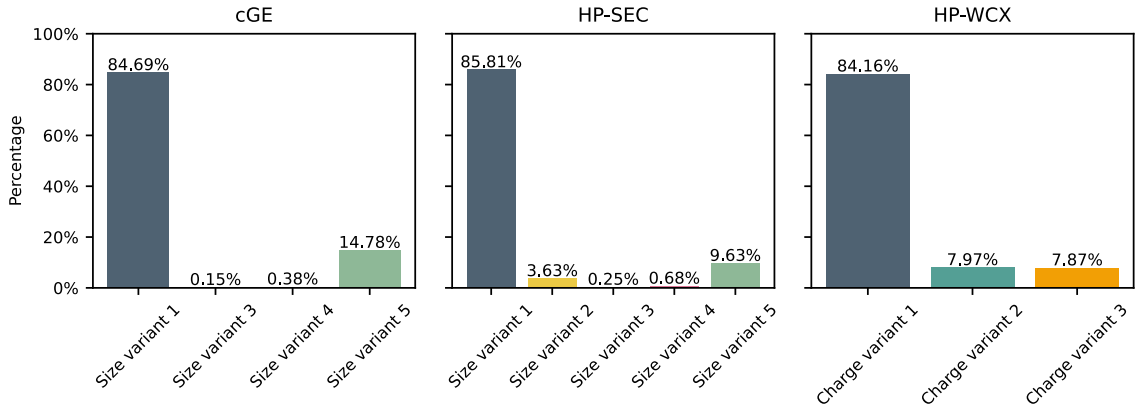

Figure 37: The composition of the CEX loading material measured by analytical capillary gel electrophoresis (cGE), high-performance size exclusion chromatography (HP-SEC), and high-performance weak-cation-exchange chromatography (HP-WCX). The different analytical methods divide the same protein mixture into different parts.

Regarding HCPs as impurities, a similar issue was observed. The loaded HCPs level could not be balanced in the wash, elution, and regeneration fractions. This was attributed to the analytical method. The HCP immunoassays are known to have high standard deviations and to be sensitive to the composition of the HCPs. This is especially pronounced in low HCP concentration levels where specific HCPs are enriched or depleted. Moreover, the HCPs are a heterogenous protein group. The chromatography models are designed to describe the interaction with the resin for a pure protein solution. It was attempted to divide the HCPs into a strong and weak binding group which, however, was unsuccessful. In depth filtration, the HCPs break throughs were investigated (data not shown). However, difficulties in mass balancing and assay changes to the manufacturing data did not allow to reliably model HCPs as impurity. For the mentioned reasons, the analytic included in this study focused on the HP-SEC size variants. An additional issue was observed for the CEX model regarding the ionic capacity. The model was tested on different columns with minor changes in ionic capacity measures. However, if the ionic capacity change was included in the model, the sensitivity of the model was stronger than experimentally observed. In fact, leaving the ionic capacity and chromatography column parameters constant, resulted in optimal results. Thus, despite the promising results of the presented CEX model, the theory seems to be uncompleted with the current CPA model. Motivated by the finding, an extensive study with varying ionic capacities would be beneficial for future model development.

The next aspect relates to the ion composition in the process. In this study, the titration curves of various adjustment steps were predicted. However, the ion composition of the capture elution pool did not match the elution buffer composition. Instead, unexpected sodium ions were measured, which seemingly co-elute from the affinity chromatography resin. In theory, sodium ions can bind to negatively charges under neutral pH. The ions can be repelled by the protonation of the negative charges under low pH, as applied during elution conditions. Although the theory is common knowledge a reliable mechanistic description of this effect is not available yet.

With regards to TFF, the membrane permeability is an important model parameter. Despite the theoretical relevance, the model was found to be more sensitive to varying permeability measures compared to the real filtration process. A possible explanation might be, that the increased permeability immediately leads to a blocking. This results in a permeate flow compared to membranes of lower permeabilities. In contrast, when adjusted to match the initial flow the course of filtration was well predicted. Hence, a more reliable parameter might be required. Another aspect concerns the scalability of filtration processes. The filtrate flow per membrane area was found to be significantly lower than in lab-scale experiments at similar pressure settings. In general, this was observed due to pressure losses in manufacturing scale. The pressure losses could be added to the model, however, the cause for the loss requires further investigations. In summary, the following challenges were observed during the studies:

- Mass balance issues arise from the use of multiple analytical methods
- During elution in capture chromatography, certain ions were observed to either bind or co-elute.
- The TFF membrane permeability exhibited stronger sensitivity in the model than during filtration experiments.
- The ionic capacity sensitivity in CEX modeling was observed to be stronger in the model than during experimentation.
- The use of e.g. mixed-mode resins and challenging process conditions may increase complexity for process modeling.
- The mass balance for host cell proteins (HCPs) proved to be particularly challenging.

6.2 Outlook

The work presented represents the initial step, or perhaps only the first attempt, in a significant journey that lies ahead. Knowledge about the process in form of mechanistic equations combined with protein properties, such as the charge, viscosity, and amino acid sequence led to the description of an entire downstream sequence by the introduced CMPM. In general, using mechanistic models to describe a process gives the development team the confidence to fundamentally understand and predict downstream process behavior. This is expected to reduce the number of experiments typically conducted to cover process eventualities. For filtration e.g., a single experiment can be sufficient to identify the blocking mechanism. Whereas the adjustment model does not have any unknown parameters to estimate. Once a model was demonstrated to give reliable results there is no good reason to not include the model during development phases. Thus, the use of reliable models presented here is expected to sustainably accelerate development and troubleshooting activities.

Despite the advantages of the presented CMPM, the limitations suggest further model development. Suggestions and potential for improvement were already listed in the previous section. It was mentioned that some aspects are not suited to be tackled by mechanistic models. Therefore, a combined approach of high-throughput screenings (HTS) and mechanistic modeling might be reasonable. This is demonstrated below as an example for CEX. The model calibration of a CEX model requires specifically designed wet-lab experiments including low and high load linear gradients. In addition, the pH dependency of the binding isotherm is an approximation and only valid for a narrow range. Thus, it would be time consuming to build a model for each resin candidate rather than using a resin screening in advance, such as a Kp-Screening [142]. The screening would help determine the optimal resin and pH conditions. From there, it would be difficult to derive the finer details such as robust cutting criteria and a control strategy based on the screening data alone. Conversely, a model can be used to find an optimal and robust process point for a selected optimal resin and pH set point. Once this is achieved, confirmation experiments are required to rule out model error. This could be embedded in a DoE for process characterization. This example demonstrates that combining technologies such as HTS, mechanistic models, and wet lab experiments can be beneficial. Clearly, direct calibration of the model using plate screening data or even amino acid sequence of proteins is of interest. However, this is still an area of research.

Another long-term goal should be to reduce the number of assisting model parameters and replace them by physical meaning. This is especially

demanded for pH relations in chromatography as discussed earlier. Similarly, the current TFF model showed promising results, however, the assisting parameter b^* should be aimed to be replaced in the future. This requires extensive experimentation with changing proteins and conditions to reveal and derive novel theories. In addition, the CMPM workflow needs to be tested on additional processes. It is expected that this will allow to better understand filtration scale effects and help to identify general trends. In addition, process variability originating from upstream could be addressed in this study with real measured data. However, these data are usually not available during the process development phases. For future projects, it would be favorable to expand the CMPM with upstream models to estimate the expected input variability for downstream.

Overall, the CMPM serves as a promising tool for describing the biopharmaceutical downstream process. It provides a valuable foundation for future studies to build upon and refine our understanding of the process. Although the model is an approximation of reality, the model sets a benchmark for the current state of knowledge in biopharmaceutical downstream process modeling. However, it is important to acknowledge that this knowledge is not yet complete and will continue to evolve through ongoing research in this area.

Bibliography

[1] B.K. Behera, Biopharmaceuticals, Challenges and Opportunities, (2020). https://doi.org/10.1201/9781351013154.

[2] M.S. Kinch, An overview of FDA-approved biologics medicines, Drug Discov Today. 20 (2015) 393–398. https://doi.org/10.1016/j.drudis.2014.09.003.

[3] D. Yi, Genentech: The Beginnings of Biotech, Ann Sci. 71 (2014) 432–434. https://doi.org/10.1080/00033790.2012.675444.

[4] N. Chaudhary, D. Weissman, K.A. Whitehead, mRNA vaccines for infectious diseases: principles, delivery and clinical translation, Nat Rev Drug Discov. 20 (2021) 817–838. https://doi.org/10.1038/s41573-021-00283-5.

[5] G. Walsh, E. Walsh, Biopharmaceutical benchmarks 2022, Nat Biotechnol. (2022) 1–39. https://doi.org/10.1038/s41587-022-01582-x.

[6] H. Kaplon, A. Chenoweth, S. Crescioli, J.M. Reichert, Antibodies to watch in 2022, Mabs. 14 (2022) 2014296. https://doi.org/10.1080/19420862.2021.2014296.

[7] U. Hafeez, H.K. Gan, A.M. Scott, Monoclonal antibodies as immunomodulatory therapy against cancer and autoimmune diseases, Curr Opin Pharmacol. 41 (2018) 114–121. https://doi.org/10.1016/j.coph.2018.05.010.

[8] A.M. Scott, J.D. Wolchok, L.J. Old, Antibody therapy of cancer, Nat Rev Cancer. 12 (2012) 278–287. https://doi.org/10.1038/nrc3236.

[9] M. Kesik-Brodacka, Progress in biopharmaceutical development, Biotechnol Appl Bioc. 65 (2018) 306–322. https://doi.org/10.1002/bab.1617.

[10] L.M. Weiner, R. Surana, S. Wang, Monoclonal antibodies: versatile platforms for cancer immunotherapy, Nat Rev Immunol. 10 (2010) 317–327. https://doi.org/10.1038/nri2744.

[11] Aspirin | C9H8O4 - PubChem, (n.d.). https://pubchem.ncbi.nlm.nih.gov/compound/Aspirin (accessed December 11, 2022).

[12] D.J. Crommelin, R.D. Sindelar, B. Meibohm, Pharmaceutical biotechnology: fundamentals and applications, Springer Science & Business Media, n.d.

[13] R.A. Rader, (Re)defining biopharmaceutical, Nat Biotechnol. 26 (2008) 743–751. https://doi.org/10.1038/nbt0708-743.

[14] P.A.J. Rosa, I.F. Ferreira, A.M. Azevedo, M.R. Aires-Barros, Aqueous two-phase systems: A viable platform in the manufacturing of biopharmaceuticals, J Chromatogr A. 1217 (2010) 2296–2305. https://doi.org/10.1016/j.chroma.2009.11.034.

[15] H.F. Liu, J. Ma, C. Winter, R. Bayer, Recovery and purification process development for monoclonal antibody production, Mabs. 2 (2010) 480–499. https://doi.org/10.4161/mabs.2.5.12645.

[16] A.A. Shukla, B. Hubbard, T. Tressel, S. Guhan, D. Low, Downstream processing of monoclonal antibodies—Application of platform approaches, J Chromatogr B. 848 (2007) 28–39. https://doi.org/10.1016/j.jchromb.2006.09.026.

[17] A.A. Shukla, J. Thömmes, Recent advances in large-scale production of monoclonal antibodies and related proteins, Trends Biotechnol. 28 (2010) 253–261. https://doi.org/10.1016/j.tibtech.2010.02.001.

[18] R.L. Fahrner, H.L. Knudsen, C.D. Basey, W. Galan, D. Feuerhelm, M. Vanderlaan, G.S. Blank, Industrial Purification of Pharmaceutical Antibodies: Development, Operation, and Validation of Chromatography Processes, Biotechnology Genetic Eng Rev. 18 (2001) 301–327. https://doi.org/10.1080/02648725.2001.10648017.

[19] M. Godar, H. de Haard, C. Blanchetot, J. Rasser, Therapeutic bispecific antibody formats: a patent applications review (1994-2017), Expert Opin Ther Pat. 28 (2018) 251–276. https://doi.org/10.1080/13543776.2018.1428307.

[20] H.K. Gan, M. van den Bent, A.B. Lassman, D.A. Reardon, A.M. Scott, Antibody–drug conjugates in glioblastoma therapy: the right drugs to the right cells, Nat Rev Clin Oncol. 14 (2017) 695–707. https://doi.org/10.1038/nrclinonc.2017.95.

[21] R.V. Kholodenko, D.V. Kalinovsky, I.I. Doronin, E.D. Ponomarev, I.V. Kholodenko, Antibody Fragments as Potential Biopharmaceuticals for Cancer Therapy: Success and Limitations, Curr Med Chem. 26 (2019) 396–426. https://doi.org/10.2174/0929867324666170817152554.

[22] C. Spiess, Q. Zhai, P.J. Carter, Alternative molecular formats and therapeutic applications for bispecific antibodies, Mol Immunol. 67 (2015) 95–106. https://doi.org/10.1016/j.molimm.2015.01.003.

[23] B. Kelley, Developing therapeutic monoclonal antibodies at pandemic pace, Nat Biotechnol. 38 (2020) 540–545. https://doi.org/10.1038/s41587-020-0512-5.

[24] I.H.T. Guideline, others, Pharmaceutical development, Q8 (2R). As Revised in August. (2009).

[25] B.K. Nfor, P.D.E.M. Verhaert, L.A.M. van der Wielen, J. Hubbuch, M. Ottens, Rational and systematic protein purification process development: the next generation, Trends Biotechnol. 27 (2009) 673–679. https://doi.org/10.1016/j.tibtech.2009.09.002.

[26] A. Rasmuson, B. Andersson, L. Olsson, R. Andersson, Mathematical Modeling in Chemical Engineering, (2014) 20–39. https://doi.org/10.1017/cbo9781107279124.004.

[27] H. Schmidt-Traub, A. Susanto, Preparative Chromatography, (2020) 525–600. https://doi.org/10.1002/9783527816347.ch10.

[28] H. Sankey, R. Nola, Theories of Scientific Method, (2006). https://doi.org/10.4324/9781315711959.

[29] A.L. Zydney, Membrane technology for purification of therapeutic proteins, Biotechnol. Bioeng. 103 (2009) 227–230. https://doi.org/10.1002/bit.22308.

[30] R. van Reis, A. Zydney, Bioprocess membrane technology, J Membrane Sci. 297 (2007) 16–50. https://doi.org/10.1016/j.memsci.2007.02.045.

[31] A.L. Zydney, New developments in membranes for bioprocessing – A review, J Membrane Sci. 620 (2020) 118804. https://doi.org/10.1016/j.memsci.2020.118804.

[32] Y. Yigzaw, R. Piper, M. Tran, A.A. Shukla, Exploitation of the Adsorptive Properties of Depth Filters for Host Cell Protein Removal during Monoclonal Antibody Purification, Biotechnol Progr. 22 (2006) 288–296. https://doi.org/10.1021/bp050274w.

[33] N. Singh, K. Pizzelli, J.K. Romero, J. Chrostowski, G. Evangelist, J. Hamzik, N. Soice, K.S. Cheng, Clarification of recombinant proteins from high cell density mammalian cell culture systems using new improved depth filters, Biotechnol. Bioeng. 110 (2013) 1964–1972. https://doi.org/10.1002/bit.24848.

[34] S.A. Johnson, S. Chen, G. Bolton, Q. Chen, S. Lute, J. Fisher, K. Brorson, Virus filtration: A review of current and future practices in bioprocessing, Biotechnol. Bioeng. 119 (2022) 743–761. https://doi.org/10.1002/bit.28017.

[35] J.Y. Kim, Y.-G. Kim, G.M. Lee, CHO cells in biotechnology for production of recombinant proteins: current state and further potential, Appl Microbiol Biotechnol. 93 (2012) 917–930. https://doi.org/10.1007/s00253-011-3758-5.

[36] P.V. Danckwerts, Continuous flow systems Distribution of residence times, Chem Eng Sci. 2 (1953) 1–13. https://doi.org/10.1016/0009-2509(53)80001-1.

[37] C.A. Brooks, S.M. Cramer, Steric mass-action ion exchange: Displacement profiles and induced salt gradients, Aiche J. 38 (1992) 1969–1978. https://doi.org/10.1002/aic.690381212.

[38] J. Diedrich, W. Heymann, S. Leweke, S. Hunt, R. Todd, C. Kunert, W. Johnson, E. von Lieres, Multi-state steric mass action model and case study on complex high loading behavior of mAb on ion exchange tentacle resin, J Chromatogr A. 1525 (2017) 60–70. https://doi.org/10.1016/j.chroma.2017.09.039.

[39] T.C. Huuk, T. Hahn, K. Doninger, J. Griesbach, S. Hepbildikler, J. Hubbuch, Modeling of complex antibody elution behavior under high protein load densities in ion exchange chromatography using an asymmetric activity coefficient, Biotechnol J. 12 (2017) 1600336. https://doi.org/10.1002/biot.201600336.

[40] X. Xu, A.M. Lenhoff, Binary adsorption of globular proteins on ion-exchange media, J Chromatogr A. 1216 (2009) 6177–6195. https://doi.org/10.1016/j.chroma.2009.06.082.

[41] B. Guélat, R. Khalaf, M. Lattuada, M. Costioli, M. Morbidelli, Protein adsorption on ion exchange resins and monoclonal antibody charge variant modulation, J Chromatogr A. 1447 (2016) 82–91. https://doi.org/10.1016/j.chroma.2016.04.018.

[42] T. Briskot, T. Hahn, T. Huuk, J. Hubbuch, Protein adsorption on ion exchange adsorbers: A comparison of a stoichiometric and non-stoichiometric modeling approach, J Chromatogr A. 1653 (2021) 462397. https://doi.org/10.1016/j.chroma.2021.462397.

[43] E.J.W. Verwey, J.Th.G. Overbeek, Long distance forces acting between colloidal particles, Trans Faraday Soc. 42 (1946) B117–B123. https://doi.org/10.1039/tf946420b117.

[44] T. Briskot, T. Hahn, T. Huuk, J. Hubbuch, Adsorption of colloidal proteins in ion-exchange chromatography under consideration of charge regulation, J Chromatogr A. 1611 (2020) 460608. https://doi.org/10.1016/j.chroma.2019.460608.

[45] T. Briskot, T. Hahn, T. Huuk, G. Wang, S. Kluters, J. Studts, F. Wittkopp, J. Winderl, P. Schwan, I. Hagemann, K. Kaiser, A. Trapp, S.M. Stamm, J. Koehn, G. Malmquist, J. Hubbuch, Analysis of complex protein elution behavior in preparative ion exchange processes using a colloidal particle adsorption model, J Chromatogr A. 1654 (2021) 462439. https://doi.org/10.1016/j.chroma.2021.462439.

[46] J.L. Lebowitz, E. Helfand, E. Praestgaard, Scaled Particle Theory of Fluid Mixtures, J Chem Phys. 43 (1965) 774–779. https://doi.org/10.1063/1.1696842.

[47] R.G. Holdich, A. Rushton, A.S. Ward, Solid-Liquid Filtration and Separation Technology : An Introduction, John Wiley & Sons, Incorporated, Hoboken, GERMANY, 1996. http://ebookcentral.proquest.com/lib/boehringeringelheim/detail.action?docID=481346.

[48] C.-C. Ho, A.L. Zydney, A Combined Pore Blockage and Cake Filtration Model for Protein Fouling during Microfiltration, J Colloid Interf Sci. 232 (2000) 389–399. https://doi.org/10.1006/jcis.2000.7231.

[49] E. Iritani, N. Katagiri, Developments of Blocking Filtration Model in Membrane Filtration, Kona Powder Part J. 33 (2016) 179–202. https://doi.org/10.14356/kona.2016024.

[50] G.B. van den Berg, C.A. Smolders, Flux decline in ultrafiltration processes, Desalination. 77 (1990) 101–133. https://doi.org/10.1016/0011-9164(90)85023-4.

[51] O. Kedem, A. Katchalsky, Thermodynamic analysis of the permeability of biological membranes to non-electrolytes, Biochim Biophys Acta. 27 (1958) 229–246. https://doi.org/10.1016/0006-3002(58)90330-5.

[52] E. Binabaji, J. Ma, S. Rao, A.L. Zydney, Theoretical analysis of the ultrafiltration behavior of highly concentrated protein solutions, J Membrane Sci. 494 (2015) 216–223. https://doi.org/10.1016/j.memsci.2015.07.068.

[53] A.L. Zydney, Stagnant film model for concentration polarization in membrane systems, J Membrane Sci. 130 (1997) 275–281. https://doi.org/10.1016/s0376-7388(97)00006-9.

[54] A.L. Zydney, Concentration effects on membrane sieving: development of a stagnant filmmodel incorporating the effects of solute-solute interactions, J Membrane Sci. 68 (1992) 183–190. https://doi.org/10.1016/0376-7388(92)80160-l.

[55] E. Binabaji, J. Ma, S. Rao, A.L. Zydney, Ultrafiltration of highly concentrated antibody solutions: Experiments and modeling for the effects of module and buffer conditions, Biotechnol Progr. 32 (2016) 692–701. https://doi.org/10.1002/btpr.2252.

[56] H. Butt, K. Graf, M. Kappl, Physics and Chemistry of Interfaces, (2010) 80–117. https://doi.org/10.1002/3527602313.ch6.

[57] G. Trefalt, S.H. Behrens, M. Borkovec, Charge Regulation in the Electrical Double Layer: Ion Adsorption and Surface Interactions, Langmuir. 32 (2016) 380–400. https://doi.org/10.1021/acs.langmuir.5b03611.

[58] T. Briskot, N. Hillebrandt, S. Kluters, G. Wang, J. Studts, T. Hahn, T. Huuk, J. Hubbuch, Modeling the Gibbs-Donnan effect during ultrafiltration and diafiltration processes using the Poisson–Boltzmann theory in combination with a basic Stern model, J Membrane Sci. 648 (2022) 120333. https://doi.org/10.1016/j.memsci.2022.120333.

[59] J.E. Ladwig, X. Zhu, P. Rolandi, R. Hart, J. Robinson, A. Rydholm, Mechanistic model of pH and excipient concentration during ultrafiltration and diafiltration processes of therapeutic antibodies, Biotechnol Progr. 36 (2020) e2993. https://doi.org/10.1002/btpr.2993.

[60] A.J. Rogers, C. Inamdar, M.G. Ierapetritou, An Integrated Approach to Simulation of Pharmaceutical Processes for Solid Drug Manufacture, Ind Eng Chem Res. 53 (2014) 5128–5147. https://doi.org/10.1021/ie401344a.

[61] E.N. Pistikopoulos, A. Barbosa-Povoa, J.H. Lee, R. Misener, A. Mitsos, G.V. Reklaitis, V. Venkatasubramanian, F. You, R. Gani, Process Systems Engineering – The Generation Next?, Comput Chem Eng. 147 (2021) 107252. https://doi.org/10.1016/j.compchemeng.2021.107252.

[62] A. Giordano, A.A. Barresi, D. Fissore, On the use of mathematical models to build the design space for the primary drying phase of a pharmaceutical lyophilization process, J Pharm Sci. 100 (2011) 311–324. https://doi.org/10.1002/jps.22264.

[63] S. Badr, H. Sugiyama, A PSE perspective for the efficient production of monoclonal antibodies: integration of process, cell, and product design aspects, Curr Opin Chem Eng. 27 (2020) 121–128. https://doi.org/10.1016/j.coche.2020.01.003.

[64] A. Rogers, M. Ierapetritou, Challenges and opportunities in modeling pharmaceutical manufacturing processes, Comput Chem Eng. 81 (2015) 32–39. https://doi.org/10.1016/j.compchemeng.2015.03.018.

[65] R. Bhambure, A.S. Rathore, Chromatography process development in the quality by design paradigm I: Establishing a high-throughput process development platform as a tool for estimating "characterization space" for an ion exchange chromatography step, Biotechnol Progr. 29 (2013) 403–414. https://doi.org/10.1002/btpr.1705.

[66] T. Zahel, S. Hauer, E.M. Mueller, P. Murphy, S. Abad, E. Vasilieva, D. Maurer, C. Brocard, D. Reinisch, P. Sagmeister, C. Herwig, Integrated Process Modeling—A Process Validation Life Cycle Companion, Bioeng. 4 (2017) 86. https://doi.org/10.3390/bioengineering4040086.

[67] G.M. Kontogeorgis, R. Dohrn, I.G. Economou, J.-C. de Hemptinne, A. ten Kate, S. Kuitunen, M. Mooijer, L.F. Žilnik, V. Vesovic, Industrial Requirements for Thermodynamic and Transport Properties: 2020, Ind Eng Chem Res. 60 (2021) 4987–5013. https://doi.org/10.1021/acs.iecr.0c05356.

[68] G. Franceschini, S. Macchietto, Model-based design of experiments for parameter precision: State of the art, Chem Eng Sci. 63 (2008) 4846–4872. https://doi.org/10.1016/j.ces.2007.11.034.

[69] B.K. Nfor, T. Ahamed, G.W.K. van Dedem, P.D.E.M. Verhaert, L.A.M. van der Wielen, M.H.M. Eppink, E.J.A.X. van de Sandt, M. Ottens, Model-based rational methodology for protein purification process synthesis, Chem Eng Sci. 89 (2013) 185–195. https://doi.org/10.1016/j.ces.2012.11.034.

[70] C. Helling, C. Borrmann, J. Strube, Optimal Integration of Directly Combined Hydrophobic Interaction and Ion Exchange Chromatography Purification Processes, Chem Eng Technol. 35 (2012) 1786–1796. https://doi.org/10.1002/ceat.201200043.

[71] T.C. Huuk, T. Hahn, A. Osberghaus, J. Hubbuch, Model-based integrated optimization and evaluation of a multi-step ion exchange chromatography, Sep Purif Technol. 136 (2014) 207–222. https://doi.org/10.1016/j.seppur.2014.09.012.

[72] S.M. Pirrung, L.A.M. van der Wielen, R.F.W.C. van Beckhoven, E.J.A.X. van de Sandt, M.H.M. Eppink, M. Ottens, Optimization of biopharmaceutical downstream processes supported by mechanistic models and artificial neural networks, Biotechnol Progr. 33 (2017) 696–707. https://doi.org/10.1002/btpr.2435.

[73] D. Saleh, G. Wang, F. Rischawy, S. Kluters, J. Studts, J. Hubbuch, In silico process characterization for biopharmaceutical development following the quality by design concept, Biotechnol Progr. 37 (2021) e3196. https://doi.org/10.1002/btpr.3196.

[74] C.E. Herman, X. Xu, S.J. Traylor, S. Ghose, Z.J. Li, A.M. Lenhoff, Behavior of weakly adsorbing protein impurities in flow-through ion-exchange chromatography, J Chromatogr A. 1664 (2022) 462788. https://doi.org/10.1016/j.chroma.2021.462788.

[75] R. Kender, F. Kaufmann, F. Rößler, B. Wunderlich, D. Golubev, I. Thomas, A.-M. Ecker, S. Rehfeldt, H. Klein, Development of a digital twin for a flexible air separation unit using a pressure-driven simulation approach, Comput Chem Eng. 151 (2021) 107349. https://doi.org/10.1016/j.compchemeng.2021.107349.

[76] R. Ambrožič, D. Arzenšek, A. Podgornik, Designing scalable ultrafiltration/diafiltration process of monoclonal antibodies via mathematical modeling by coupling mass balances and Poisson–Boltzmann equation, Biotechnol Bioeng. 118 (2021) 633–646. https://doi.org/10.1002/bit.27598.

[77] J. Westall, H. Hohl, A comparison of electrostatic models for the oxide/solution interface, Adv Colloid Interfac. 12 (1980) 265–294. https://doi.org/10.1016/0001-8686(80)80012-1.

[78] C.W. Davies, The extent of dissociation of salts in water. Part VIII. An equation for the mean ionic activity coefficient of an electrolyte in water, and a revision of the dissociation constants of some sulphates., Journal of the Chemical Society (Resumed). (1938) 2093–2098.

[79] D.-M. Smilgies, E. Folta-Stogniew, Molecular weight–gyration radius relation of globular proteins: a comparison of light scattering, small-angle X-ray scattering and structure-based data, J Appl Crystallogr. 48 (2015) 1604–1606. https://doi.org/10.1107/s1600576715015551.

[80] J. Antosiewicz, J.A. McCammon, M.K. Gilson, The Determinants of pK as in Proteins †, Biochemistry-Us. 35 (1996) 7819–7833. https://doi.org/10.1021/bi9601565.

[81] D. Saleh, G. Wang, B. Müller, F. Rischawy, S. Kluters, J. Studts, J. Hubbuch, Straightforward method for calibration of mechanistic cation exchange chromatography models for industrial applications, Biotechnol Progr. 36 (2020) e2984. https://doi.org/10.1002/btpr.2984.

[82] G. Guiochon, D.G. Shirazi, A. Felinger, A.M. Katti, Fundamentals of Preparative and Nonlinear Chromatography, (2006) 471–529. https://doi.org/10.1016/b978-012370537-2/50034-5.

[83] J.S. Mackie, P. Meares, The diffusion of electrolytes in a cation-exchange resin membrane I. Theoretical, Proc Royal Soc Lond Ser Math Phys Sci. 232 (1955) 498–509. https://doi.org/10.1098/rspa.1955.0234.

[84] T.C. Huuk, T. Briskot, T. Hahn, J. Hubbuch, A versatile noninvasive method for adsorber quantification in batch and column chromatography based on the ionic capacity, Biotechnol Progr. 32 (2016) 666–677. https://doi.org/10.1002/btpr.2228.

[85] K.-C. Loh, D.I.C. Wang, Characterization of pore size distribution of packing materials used in perfusion chromatography using a network model, J Chromatogr A. 718 (1995) 239–255. https://doi.org/10.1016/0021-9673(95)00706-7.

[86] A. Geng, K.-C. Loh, Contribution of axial dispersion to band spreading in perfusion chromatography, J Chromatogr A. 918 (2001) 37–46. https://doi.org/10.1016/s0021-9673(01)00725-7.

[87] W. Heymann, J. Glaser, F. Schlegel, W. Johnson, P. Rolandi, E. von Lieres, Advanced score system and automated search strategies for parameter estimation in mechanistic chromatography modeling, J Chromatogr A. 1661 (2022) 462693. https://doi.org/10.1016/j.chroma.2021.462693.

[88] F. Rischawy, D. Saleh, T. Hahn, S. Oelmeier, J. Spitz, S. Kluters, Good modeling practice for industrial chromatography: Mechanistic modeling of ion exchange chromatography of a bispecific antibody, Comput Chem Eng. 130 (2019) 106532. https://doi.org/10.1016/j.compchemeng.2019.106532.

[89] C. Hoffmann, J. Weigert, E. Esche, J.-U. Repke, Parameter Estimation for Thermodynamic Models Using an Identifiability Analysis and Subset Selection, Comput-Aided Chem En. 46 (2019) 583–588. https://doi.org/10.1016/b978-0-12-818634-3.50098-9.

[90] K.A.P. McLean, K.B. McAuley, Mathematical modelling of chemical processes—obtaining the best model predictions and parameter estimates using identifiability and estimability procedures, Can J Chem Eng. 90 (2012) 351–366. https://doi.org/10.1002/cjce.20660.

[91] C. Huang, Y. Wang, X. Xu, J. Mills, W. Jin, S. Ghose, Z.J. Li, Hydrophobic property of cation-exchange resins affects monoclonal antibody aggregation, J Chromatogr A. 1631 (2020) 461573. https://doi.org/10.1016/j.chroma.2020.461573.

[92] N.E. Levy, K.N. Valente, K.H. Lee, A.M. Lenhoff, Host cell protein impurities in chromatographic polishing steps for monoclonal antibody purification, Biotechnol Bioeng. 113 (2016) 1260–1272. https://doi.org/10.1002/bit.25882.

[93] R.B. McCleskey, D.K. Nordstrom, J.N. Ryan, Comparison of electrical conductivity calculation methods for natural waters, Limnology Oceanogr Methods. 10 (2012) 952–967. https://doi.org/10.4319/lom.2012.10.952.

[94] R. Mathaes, A. Koulov, S. Joerg, H.-C. Mahler, Subcutaneous Injection Volume of Biopharmaceuticals—Pushing the Boundaries, J Pharm Sci. 105 (2016) 2255–2259. https://doi.org/10.1016/j.xphs.2016.05.029.

[95] E. Rosenberg, S. Hepbildikler, W. Kuhne, G. Winter, Ultrafiltration concentration of monoclonal antibody solutions: Development of an optimized method minimizing aggregation, J Membrane Sci. 342 (2009) 50–59. https://doi.org/10.1016/j.memsci.2009.06.028.

[96] G. Belfort, R.H. Davis, A.L. Zydney, The behavior of suspensions and macromolecular solutions in crossflow microfiltration, J Membrane Sci. 96 (1994) 1–58. https://doi.org/10.1016/0376-7388(94)00119-7.

[97] Y. Baek, N. Singh, A. Arunkumar, A. Zydney, Ultrafiltration behavior of an Fc-fusion protein: Filtrate flux data and modeling, J Membrane Sci. 528 (2017) 171–177. https://doi.org/10.1016/j.memsci.2017.01.029.

[98] Y. Baek, N. Singh, A. Arunkumar, M. Borys, Z.J. Li, A.L. Zydney, Ultrafiltration behavior of monoclonal antibodies and Fc-fusion proteins: Effects of physical properties, Biotechnol Bioeng. 114 (2017) 2057–2065. https://doi.org/10.1002/bit.26326.

[99] H.M. Yeh, T.W. Cheng, H.H. Wu, Membrane ultrafiltration in hollow-fiber module with the consideration of pressure declination along the fibers, Sep Purif Technol. 13 (1998) 171–180. https://doi.org/10.1016/s1383-5866(98)00041-0.

[100] A.R.D. Costa, A.G. Fane, D.E. Wiley, Spacer characterization and pressure drop modelling in spacer-filled channels for ultrafiltration, J Membrane Sci. 87 (1994) 79–98. https://doi.org/10.1016/0376-7388(93)e0076-p.

[101] M.G. Jabra, A.M. Lipinski, A.L. Zydney, Single Pass Tangential Flow Filtration (SPTFF) of monoclonal antibodies: Experimental studies and theoretical analysis, J Membrane Sci. 637 (2021) 119606. https://doi.org/10.1016/j.memsci.2021.119606.

[102] E. Binabaji, J. Ma, A.L. Zydney, Intermolecular Interactions and the Viscosity of Highly Concentrated Monoclonal Antibody Solutions, Pharmaceut Res. 32 (2015) 3102–3109. https://doi.org/10.1007/s11095-015-1690-6.

[103] E. Binabaji, S. Rao, A.L. Zydney, The osmotic pressure of highly concentrated monoclonal antibody solutions: Effect of solution conditions, Biotechnol Bioeng. 111 (2014) 529–536. https://doi.org/10.1002/bit.25104.

[104] V.L. Vilker, C.K. Colton, K.A. Smith, D.L. Green, The osmotic pressure of concentrated protein and lipoprotein solutions and its significance to ultrafiltration, J Membrane Sci. 20 (1984) 63–77. https://doi.org/10.1016/s0376-7388(00)80723-1.

[105] V.L. Vilker, C.K. Colton, K.A. Smith, The osmotic pressure of concentrated protein solutions: Effect of concentration and ph in saline solutions of bovine serum albumin, J Colloid Interf Sci. 79 (1981) 548–566. https://doi.org/10.1016/0021-9797(81)90106-5.

[106] W.G. McMillan, J.E. Mayer, The Statistical Thermodynamics of Multicomponent Systems, J Chem Phys. 13 (1945) 276–305. https://doi.org/10.1063/1.1724036.

[107] P.D. Ross, A.P. Minton, Hard quasispherical model for the viscosity of hemoglobin solutions, Biochem Bioph Res Co. 76 (1977) 971–976. https://doi.org/10.1016/0006-291x(77)90950-0.

[108] J. Kaiser, J. Krarup, E.B. Hansen, M. Pinelo, U. Krühne, Defining the optimal operating conditions and configuration of a single-pass tangential flow filtration (SPTFF) system via CFD modelling, Sep Purif Technol. 290 (2022) 120776. https://doi.org/10.1016/j.seppur.2022.120776.

[109] H. Darcy, Les fontaines publiques de la ville de Dijon, Paris: Dalmont, 1856.

[110] M.M. Castellanos, J.A. Pathak, R.H. Colby, Both protein adsorption and aggregation contribute to shear yielding and viscosity increase in protein solutions, Soft Matter. 10 (2013) 122–131. https://doi.org/10.1039/c3sm51994e.

[111] H. Lutz, J. Arias, Y. Zou, High concentration biotherapeutic formulation and ultrafiltration: Part 1 pressure limits, Biotechnol Progr. 33 (2017) 113–124. https://doi.org/10.1002/btpr.2334.

[112] J. Wu, J.M. Prausnitz, Osmotic pressures of aqueous bovine serum albumin solutions at high ionic strength, Fluid Phase Equilibr. 155 (1999) 139–154. https://doi.org/10.1016/s0378-3812(98)00435-x.

[113] R.G. Mortimer, Physical Chemistry, Elsevier Academic Press. (2008).

[114] B.D. Connolly, C. Petry, S. Yadav, B. Demeule, N. Ciaccio, J.M.R. Moore, S.J. Shire, Y.R. Gokarn, Weak Interactions Govern the Viscosity of Concentrated Antibody Solutions: High-Throughput Analysis Using the Diffusion Interaction Parameter, Biophys J. 103 (2012) 69–78. https://doi.org/10.1016/j.bpj.2012.04.047.

[115] S. Saito, J. Hasegawa, N. Kobayashi, N. Kishi, S. Uchiyama, K. Fukui, Behavior of Monoclonal Antibodies: Relation Between the Second Virial Coefficient (B2) at Low Concentrations and Aggregation Propensity and Viscosity at High Concentrations, Pharmaceut Res. 29 (2012) 397–410. https://doi.org/10.1007/s11095-011-0563-x.

[116] Ultrafiltration Diafiltration Process Development, (n.d.). https://www.slideshare.net/FrdricSengler/ultrafiltrationdiafiltration-process-development-of-high-concentrationviscosity-application (accessed November 23, 2022).

[117] E. Papadakis, J.M. Woodley, R. Gani, Chapter 24 Perspective on PSE in pharmaceutical process development and innovation, Comput-Aided Chem En. 41 (2018) 597–656. https://doi.org/10.1016/b978-0-444-63963-9.00024-5.

[118] D. Saleh, G. Wang, B. Mueller, F. Rischawy, S. Kluters, J. Studts, J. Hubbuch, Cross-scale quality assessment of a mechanistic cation exchange chromatography model, Biotechnol Progr. 37 (2021) e3081. https://doi.org/10.1002/btpr.3081.

[119] F. Rischawy, T. Briskot, A. Schimek, G. Wang, D. Saleh, S. Kluters, J. Studts, J. Hubbuch, Integrated process model for the prediction of biopharmaceutical manufacturing chromatography and adjustment steps, J Chromatogr A. (2022) 463421. https://doi.org/10.1016/j.chroma.2022.463421.

[120] K. Westerberg, E. Broberg-Hansen, L. Sejergaard, B. Nilsson, Model-based risk analysis of coupled process steps, Biotechnol Bioeng. 110 (2013) 2462–2470. https://doi.org/10.1002/bit.24909.

[121] S.W. Benner, J.P. Welsh, M.A. Rauscher, J.M. Pollard, Prediction of lab and manufacturing scale chromatography performance using mini-columns and mechanistic modeling, J Chromatogr A. 1593 (2019) 54–62. https://doi.org/10.1016/j.chroma.2019.01.063.

[122] R. Hess, D. Yun, D. Saleh, T. Briskot, J.-H. Grosch, G. Wang, T. Schwab, J. Hubbuch, Standardized method for mechanistic modeling of multimodal anion exchange chromatography in flow through operation, J Chromatogr A. (2023) 463789. https://doi.org/10.1016/j.chroma.2023.463789.

[123] L. VL, P. TM, Competitive adsorption of antibodies in Protein A chromatography, (2018).

[124] V. Lane, Computational Characterization of Protein A – Antibody Binding, Carnegie Mellon University, 2018.

[125] A.R. Denton, Poisson–Boltzmann theory of charged colloids: limits of the cell model for salty suspensions, J Phys Condens Matter. 22 (2010) 364108. https://doi.org/10.1088/0953-8984/22/36/364108.

[126] C. Duclos-Orsello, W. Li, C.-C. Ho, A three mechanism model to describe fouling of microfiltration membranes, J Membrane Sci. 280 (2006) 856–866. https://doi.org/10.1016/j.memsci.2006.03.005.

[127] I.M. Griffiths, A. Kumar, P.S. Stewart, A combined network model for membrane fouling, J Colloid Interf Sci. 432 (2014) 10–18. https://doi.org/10.1016/j.jcis.2014.06.021.

[128] G. Bolton, D. LaCasse, R. Kuriyel, Combined models of membrane fouling: Development and application to microfiltration and ultrafiltration of biological fluids, J Membrane Sci. 277 (2006) 75–84. https://doi.org/10.1016/j.memsci.2004.12.053.

[129] Z.H. Syedain, D.M. Bohonak, A.L. Zydney, Protein Fouling of Virus Filtration Membranes: Effects of Membrane Orientation and Operating Conditions, Biotechnol Progr. 22 (2006) 1163–1169. https://doi.org/10.1021/bp050350v.

[130] A.S. Rathore, V. Kumar, A. Arora, S. Lute, K. Brorson, A. Shukla, Mechanistic modeling of viral filtration, J Membrane Sci. 458 (2014) 96–103. https://doi.org/10.1016/j.memsci.2014.01.037.

[131] M. Bakhshayeshi, A.L. Zydney, Effect of solution pH on protein transmission and membrane capacity during virus filtration, Biotechnol Bioeng. 100 (2008) 108–117. https://doi.org/10.1002/bit.21735.

[132] F. Rischawy, T. Briskot, F. Nitsch, D. Saleh, G. Wang, S. Kluters, J. Studts, J. Hubbuchb, Modeling of biopharmaceutical UF/DF from laboratory to manufacturing scale, (Submitted and Provided in the Supplementary). (2022).

[133] S. Leweke, E. von Lieres, Chromatography Analysis and Design Toolkit (CADET), Comput Chem Eng. 113 (2018) 274–294. https://doi.org/10.1016/j.compchemeng.2018.02.025.

[134] KappaSelect LambdaFabSelect, (n.d.).

[135] J. Deisenhofer, Crystallographic refinement and atomic models of a human Fc fragment and its complex with fragment B of protein A from Staphylococcus aureus at

2.9- and 2.8-.ANG. resolution, Biochemistry-Us. 20 (1981) 2361–2370. https://doi.org/10.1021/bi00512a001.

[136] S. Chaudhury, D.R. Ripoll, A. Wallqvist, Structure-based pKa prediction provides a thermodynamic basis for the role of histidines in pH-induced conformational transitions in dengue virus, Biochem Biophysics Reports. 4 (2015) 375–385. https://doi.org/10.1016/j.bbrep.2015.10.014.

[137] S. Chollangi, R. Parker, N. Singh, Y. Li, M. Borys, Z. Li, Development of robust antibody purification by optimizing protein-A chromatography in combination with precipitation methodologies, Biotechnol Bioeng. 112 (2015) 2292–2304. https://doi.org/10.1002/bit.25639.

[138] A.U. Krupp, C.P. Please, A. Kumar, I.M. Griffiths, Scaling-up of multi-capsule depth filtration systems by modeling flow and pressure distribution, Sep Purif Technol. 172 (2017) 350–356. https://doi.org/10.1016/j.seppur.2016.07.028.

[139] R. van der Kant, A.R. Karow-Zwick, J.V. Durme, M. Blech, R. Gallardo, D. Seeliger, K. Aßfalg, P. Baatsen, G. Compernolle, A. Gils, J.M. Studts, P. Schulz, P. Garidel, J. Schymkowitz, F. Rousseau, Prediction and Reduction of the Aggregation of Monoclonal Antibodies, J Mol Biol. 429 (2017) 1244–1261. https://doi.org/10.1016/j.jmb.2017.03.014.

[140] S. Kluters, M. Hafner, T. von Hirschheydt, C. Frech, Solvent modulated linear pH gradient elution for the purification of conventional and bispecific antibodies: Modeling and application, J Chromatogr A. 1418 (2015) 119–129. https://doi.org/10.1016/j.chroma.2015.09.053.

[141] O. Khanal, V. Kumar, A.M. Lenhoff, Displacement to separate host-cell proteins and aggregates in cation-exchange chromatography of monoclonal antibodies, Biotechnol. Bioeng. 118 (2021) 164–174. https://doi.org/10.1002/bit.27559.

[142] P. McDonald, B. Tran, C.R. Williams, M. Wong, T. Zhao, B.D. Kelley, P. Lester, The rapid identification of elution conditions for therapeutic antibodies from cation-exchange chromatography resins using high-throughput screening, J Chromatogr A. 1433 (2016) 66–74. https://doi.org/10.1016/j.chroma.2015.12.071.

[143] T. Briskot, F. Stückler, F. Wittkopp, C. Williams, J. Yang, S. Konrad, K. Doninger, J. Griesbach, M. Bennecke, S. Hepbildikler, J. Hubbuch, Prediction uncertainty assessment of chromatography models using Bayesian inference, J Chromatogr A. 1587 (2019) 101–110. https://doi.org/10.1016/j.chroma.2018.11.076.

Abbreviations

AC	Affinity chromatography
AcOH	Acetic acid
AEX	Anion-exchange chromatography
CEX	Cation-exchange chromatography
cGE	Capillary gel electrophoresis
CHO	Chinese hamster ovary
CPA	Colloidal particle adsorption
CPA	Colloidal particle adsorption
CPP	Critical process parameter
CQA	Critical quality attribute
CV	Column volume
DNA	Deoxyribonucleic acid
DoE	Design of experiments
DV	Diafiltration volume
EDM	Equilibrium-dispersive model
EMA	European Medicines Agency
FDA	U.S. Food and Drug Administration
GRM	General rate model
HCCF	Harvest cell culture fluid
HCLF	High concentrated liquid formulation
HCP	Host cell protein
HIC	Hydrophobic interaction chromatography
HP-SEC	High performance size-exclusion chromatography (analytic)
HP-WCX	High performance weak-cation-exchange chromatography (analytic)
HTS	High-throughput screening
ICH	International conference on harmonization of technical requirements for registration of pharmaceuticals for human use
IEX	Ion-exchange chromatography
iSEC	Inverse size exclusion chromatography
LHS	Latin hypercube sampling
LRM	Lumped rate model
mAb	Monoclonal antibody
MMC	Mixed-mode chromatography
NWP	Normalized water permeability
ODE	Ordinary differential equation
PB	Poisson-Boltzmann
PDE	Partial differential equation
PES	Polyethersulfone
pI	Isoelectric point
PSE	Process system engineering
PVDF	Polyvinylidene fluoride

QbD	Quality by design
RT	Room temperature
SDS	Sodium dodecyl sulfate
SEC	Size exclusion chromatography
SMA	Steric mass action
SPT	Scaled particle theory
SPTFF	Single-pass tangential flow filtration
TDM	Transport-dispersive model
TFF	Tangential flow filtration
TMP	Transmembrane pressure
UF/DF	Ultrafiltration/Diafiltration
WS	Wigner-Seitz

Symbols

Symbol	Unit	Description
$\overline{J_v}$	ms^{-1}	Average permeate flux
$\dot{N}_{bound}$	$mols^{-1}$	Molar material flow leaving the liquid phase due to adsorption
$\dot{N}_{convection}$	$mols^{-1}$	Molar material transport by convection
$\dot{N}_{diffusion}$	$mols^{-1}$	Molar material transport by diffusion
$\dot{N}_{trans}$	$mols^{-1}$	Molar material transported through the particle film resistance layer
$\dot{N}_p$	$mols^{-1}$	Molar flow of protein
$\overline{pH}$	-	Average pH which can be measured
Λ_{IEX}	$molL^{-1}$	Ionic capacity per liter resin backbone
A_C	m^2	Column cross-section area
A_{cs}	m^2	Feed channel cross-sectional area
A_{int}	m^2	Interstitial cross-section area of the chromatography liquid phase
A_m	m^2	Membrane area
$A_{S,0}$	m^2m^{-3}	Total available surface area
A_s	m^{-1}	Specific adsorber surface per skeleton volume
$A_{P,cross}$	m^2	Resin particle cross-section area
A_P	m^2	Resin particle surface area
B_1	$kgmol^{-1}$	First virial coefficient
B_2	$molm^3kg^{-2}$	Second virial coefficient
B_3	$mol^2m^6kg^{-4}$	Third virial coefficient
C_b	gL^{-1}	Bulk protein concentration for filtration
C_S	Fm^{-2}	Stern capacitance
D_{AX}	m^2s^{-1}	Axial dispersion coefficient
D_m	cm^2s^{-1}	Molecular diffusion coefficient
D_{pore}	m^2s^{-1}	Pore diffusion coefficient
F_{acc}	-	Pore accessibility factor
F_{buffer}	Ls^{-1}	Inflow buffer
F_{in}	Ls^{-1}	Inflow feed
$F_{permeate}$	Ls^{-1}	Permeate flow
I_m	$molm^{-3}$	Ionic strength
J_{lim}	ms^{-1}	Limiting local permeate flux
J_{membr}	ms^{-1}	Membrane limited local permeate flux
J_v	ms^{-1}	Permeate flux
K_v	-	Equilibrium coefficient
K_a'	$molL^{-1}$	Protein acid dissociation constant
K_a''	$molL^{-1}$	Ligand acid dissociation constant
L_C	m	Column length
L_p	$ms^{-1}Pa^{-1}$	Membrane hydraulic permeability
M_n	-	Number of membranes
M_p	$gmol^{-1}$	Molar mass of protein
N_A	mol^{-1}	Avogadro's constant
P_{feed}	Pa	Feed side pressure in TFF processes
$P_{permeate}$	Pa	Permeate pressure in TFF processes
$P_{retentate}$	Pa	Retentate side pressure in TFF processes
Q_0	m^3s^{-1}	Initial volumetric flow
$Q_{blocked}$	m^3s^{-1}	Flow through blocked pores
Q_{open}	m^3s^{-1}	Flow through open pores

R^*	-	Resistance parameter
R_m	m^{-1}	Clean membrane resistance
R_p	m^{-1}	Resistance of a growing deposit
R_p0	m^{-1}	Resistance of a single protein aggregate
R_WS	M	Radius of the Wigner-Seitz cell
V_C	m^3	Column volume
$V_\mathrm{p,liquid}$	m^3	Resin particle liquid phase volume
$V_\mathrm{p,solid}$	m^3	Resin particle solid phase volume (resin backbone)
V_p	m^3	Resin particle volume
V_t	LL^{-1}	Titrant volume
Z_lat	-	Characteristic lateral charge
a_M	m	Protein outer radius
a_p	-	Membrane specific pressure drop parameter
$\overline{c}$	$molm^{-3}$	Ion concentration
c_0	$molm^{-3}$	Ion concentration of the fully protonated state
c_b	$molm^{-3}$	Bulk concentration in TFF cassette or chromatography column interstitial volume
c_in	$molm^{-3}$	Column inlet concentration
c_M	$molm^{-3}$	Protein concentration during adjustment steps
c_max	gL^{-1}	Mooney equation concentration at which viscosity becomes infinite
c_p	$molm^{-3}$	Molar concentration in the resin particles liquid phase
c_s	$molL^{-1}$	Salt concentration
c_t	$molm^{-3}$	Titrant concentration
c_total	$molm^{-3}$	Total ion concentration
c_w	$molm^{-3}$	Wall concentration of TFF membrane
d_p	m^3	Resin particle diameter
k_0	ms^{-1}	Mass transfer coefficient of the modified concentration polarization model
k_ads	s^{-1}	Adsorption rate constant
k_b	JK^{-1}	Boltzmann constant
k_b	s^{-1}	Pore blockage constant
k_c	sm^{-6}	Cake filtration constant
k_des	s^{-1}	Desorption rate constant
k_eff	ms^{-1}	effective mass transfer coefficient
k_film	ms^{-1}	Film transfer coefficient
k_i	m^{-3}	Intermediate blockage constant
k_kin	s^{-1}	Adsorption kinetic parameter
k_kin^*	s^{-1}	Kinetic constant (fitting parameter)
k_l	m	Forchheimer additional loss coefficient
k_m	-	TFF membrane pressure constant
k_P	m^{-3}	Pore constriction constant
k_p	m^2	Forchheimer permeability coefficient
k_pore	ms^{-1}	Pore transfer coefficient
q_{max}	$molm^{-3}$	Maximum achievable concentration on the resin backbone
r_C	m	Column radius
r_P	m	Resin particle radius
u_A	J	Interaction free energy
u_eff	ms^{-1}	Effective crossflow
u_int	ms^{-1}	Linear interstitial flow
u_lat	J	Lateral protein-protein interaction energy
u_lat	J	Lateral interaction energy
x_DF	-	Diafiltration-exchange parameter

z_c	-	Charge of adsorbed protein
Γ_L	$molm^{-2}$	Ligand density
δ^*	m	Thickness of the boundary layer
δ_m	m	Minimum interaction free energy
ε_0	$C^2N^{-1}m^{-1}$	Vacuum permittivity
ε_{int}	-	Chromatography interstitial volume fraction
ε_p	-	Particle porosity
ζ	-	Charge of protonated side chain
η_0	Pas	Buffer viscosity
η_p	Pas	Protein viscosity
μ_b	Pas	Bulk solution viscosity
ρ_e	Cm^{-3}	Charge density
σ_A	Cm^{-2}	Surface charge density
$\overline{\psi}$	V	Average electric potential
ψ_0	V	Electric potential at the proteins surface
Δ	-	Thickness of the interaction boundary layer
ΔP_{TMP}	Pa	Transmembrane pressure difference in TFF processes
ΔP	Pa	Pressure difference
pH_0	-	pH at the proteins surface
pH_{ref}	-	Reference pH
pK_a'	-	Protein acid dissociation constant in log10
pK_a''	-	Ligand acid dissociation constant in log10
q_c	$molm^{-2}$	Counter-ions per adsorber surface
Z	-	Protein charge
Δ	-	Interaction boundary layer thickness
Θ	-	Surface coverage
Π	Pa	Osmotic pressure
B	-	Available surface function
D	m^2s^{-1}	Diffusion coefficient
K	m	Partitioning coefficient
Q	m^3s^{-1}	Volumetric flow rate
R	$Jmol^{-1}K$	Ideal gas constant
V	m^3	Filtrate volume
a	m	Colloid radius
b	Lg^{-1}	Mooney equation coefficient
c	$molm^{-3}$	Molar concentration
e	C	Elementary charge
$f'R'$	mkg^{-1}	Deposit growth and the specific protein layer resistance
k	s^{-1}	General blocking constant
n	-	Filter blocking exponent
q	$molm^{-3}$	Concentration bound per resin backbone volume
u	ms^{-1}	Linear flow
z	-	Charge of ion
Ψ	V	Electric potential
α	m^2kg^{-1}	Pore blockage parameter
δ	m	Polarization boundary layer thickness
ε	-	Relative permittivity
η	Pas	Dynamic viscosity
μ	$Jmol^{-1}$	Chemical potential

Appendix A Supplementary material

The steric mass action isotherm

Ion-exchange chromatography binding behavior can be described by the steric mass action isotherm (SMA) introduced by Brooks and Cramer [37]. The theory is based on an equilibrium state given by:

$$c_{\mathrm{p},i}(x,t) + \nu_i \cdot \bar{q}_s(x,t) \underset{k_{\mathrm{des},i}}{\overset{k_{\mathrm{ads},i}}{\rightleftarrows}} q_i(x,t) + \nu_i \cdot c_{\mathrm{p,s}}(x,t) \qquad (158)$$

where an equilibrium is assumed between protein concentration in solution and counter-ions (named salt) bound to the resin $\bar{q}_{\mathrm{s}}$ [molm^{-3}], with protein bound to the resin and salt in the particles liquid phase $c_{\mathrm{p,s}}$ [molm^{-3}]. The characteristic charge ν_i [-] of the protein balances the protein charge which is assumed to be deviate from the salt charge of 1. The equilibrium rates are represented by the adsorption rate k_{ads} [m^{3}mol^{-1}s^{-1}] and desorption rate k_{des} [m^{3}mol^{-1}s^{-1}]. The change of bound protein can be described by the adsorption and desorption rate as:

$$\begin{aligned}\frac{dq_i(x,t)}{dt} &= \dot{r}_{\mathrm{ads}}(x,t) - \dot{r}_{\mathrm{des}}(x,t) \\ &= k_{\mathrm{ads},i}\bar{q}_s^{\nu_i}(x,t)c_{\mathrm{p},i}(x,t) - k_{\mathrm{des},i}q_i(x,t)c_{\mathrm{p,s}}^{\nu_i}(x,t).\end{aligned} \qquad (159)$$

Inserting the rearranged electroneutrality condition on the stationary phase defined as:

$$\bar{q}_s(x,t) = \Lambda - \sum_{i=1}^{n}(\nu_i + \sigma_i)q_i(x,t) \qquad (160)$$

in Eq. (160) leads to:

$$\frac{dq_i(x,t)}{dt} = k_{\mathrm{ads},i}\left(\Lambda - \sum_{i=1}^{n}(\nu_i + \sigma_i)q_i(x,t)\right)^{\nu_i} c_i - k_{\mathrm{des},i}\, q_i c_{\mathrm{p},s}^{\nu_i} \qquad (161)$$

where the available ionic capacity is represented by Λ [molm^{-3}] and charges sterically shielded (non-interacting) by the protein by parameter σ_i [-]. Eq. (161) can be transformed into a kinetic formulation by dividing $k_{\mathrm{des},i}$:

$$k_{\mathrm{kin}}\frac{dq_i(x,t)}{dt} = K_{\mathrm{eq},i}\left(\Lambda - \sum_{i=1}^{n}(\nu_i + \sigma_i)q_i(x,t)\right)^{\nu_i} c_i - q_i c_s^{\nu_i} \qquad (162)$$

where $k_{\mathrm{kin},i}$ [molm^{-3}] is defined as the inverse of $k_{\mathrm{des},i}$ and the equilibrium coefficient $K_{\mathrm{eq},i}$ [-] is defined as the ratio of $k_{\mathrm{ads},i}$ and $k_{\mathrm{des},i}$.